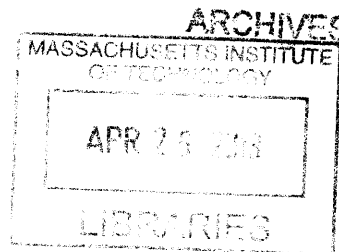


**Prediction of the Reactor Antineutrino Flux for
the Double Chooz Experiment**

by

Christopher LaDon Jones



Submitted to the Laboratory for Nuclear Science
in partial fulfillment of the requirements for the degree of

Department of Physics

at the

MASSACHUSETTS INSTITUTE OF TECHNOLOGY

September 2012

© Massachusetts Institute of Technology 2012. All rights reserved.

A
Author
Laboratory for Nuclear Science
July 9, 2012

/ / / / /
Certified by
Janet M. Conrad
Professor
Thesis Supervisor

Accepted by
John Belcher
Associate Department Head for Education

Prediction of the Reactor Antineutrino Flux for the Double Chooz Experiment

by

Christopher LaDon Jones

Submitted to the Laboratory for Nuclear Science
on July 9, 2012, in partial fulfillment of the
requirements for the degree of
Department of Physics

Abstract

This thesis benchmarks the deterministic lattice code, DRAGON, against data, and then applies this code to make a prediction for the antineutrino flux from the Chooz B1 and B2 reactors. Data from the destructive assay of rods from the Takahama-3 reactor and from the SONGS antineutrino detector are used for comparisons. The resulting prediction from the tuned DRAGON code is then compared to the first antineutrino event spectra from Double Chooz. Use of this simulation in nuclear nonproliferation studies is discussed.

Thesis Supervisor: Janet M. Conrad
Title: Professor

Acknowledgments

I thank my advisor, Professor Janet Conrad, for helping me to make some of my potential kinetic. I thank Dr. Lindley Winslow (now Professor!) for being a model of equanimity and tenacity as a scientist. And I thank Kazuhiro Terao for forgiving my awful Japanese. I thank Arthur Franke and Matt Touns for extensive help on using DCRxtrTools and DCDelayedCoinc, and just for being all-around great people. I thank Erica Caden, Brandon White, and Cara Maesano for the frequent smiley faces, in person and on Skype.

I thank Dr. Adam Bernstein and the Advanced Detectors Group at Lawrence Livermore National Laboratory for allowing me to participate in fascinating work and for the numerous Taco Tuesdays. I thank Professors Guy Marleau and Alain Hebert at Polytechnique Montreal for their patience and assistance with the DRAGON code and Dr. Anna Erickson for her impromptu primers in reactor physics.

I had extensive support from the MIT graduate student community, in particular from the Simmons Hall Houseteam. Thank you for being there for me during the best and worst times. In MIT LNS, I'll definitely miss commiserating about grad school with Asher Kaboth, Shawn Henderson, Ross Corliss, Will Leight, Christina Ignarra, and Jim Hays-Wehle. I thank Tai Sakuma for teaching me Python and R. I appreciate all of the hours that Michael Betancourt spent discussing Bayesian inference with me. I thank Clemmie Jones for her diligent editing of this thesis, and Josh Spitz, Lindley Winslow, and Anna Erickson for their patience and very helpful comments.

I thank my parents and brothers for not immediately disassembling my scale-model of the Solar System made of basketballs and baseballs when I was 7. My interest in science only deepened from there.

I thank Lauren Scharfenberg for reminding me of the importance of explaining physics to mere mortals and not just to other physicists.

On December 6, 2010, my wonderful daughter Elena Claire was born. She personally kept me on schedule in finishing this dissertation. Finally, I thank my wife, Rachel, for her love and enduring support, and for enduring me. I dedicate this work

to you both.

Contents

1	Introduction and Motivation	17
1.1	The Oscillating Leptons	18
1.2	Parameterizing the PMNS Matrix	19
1.3	The Search For θ_{13}	21
1.4	A Summary of Recent Reactor Antineutrino Experiments	22
1.4.1	Disappearance Experiments	22
1.4.2	The CHOOZ Experiment	24
1.4.3	The Palo Verde Experiment	27
1.4.4	Daya Bay & RENO	29
1.4.5	Appearance Experiments	31
1.5	The Reactor Antineutrino Anomaly	34
1.5.1	Very Short Baseline Reactor Experiments	35
1.5.2	Reanalysis of Reactor Flux Prediction	35
2	The Double Chooz Experiment	39
2.1	Location	39
2.2	The Chooz Reactor Cores	40
2.2.1	Reactor Plant Design	40
2.2.2	Reactor Core Layout	40
2.2.3	Generation of Antineutrinos in the Core	42
2.3	Detector Design	44
2.3.1	Detecting Antineutrinos With Inverse β Decay	47
2.3.2	The Target Volume	48

2.3.3	The Gamma Catcher	48
2.3.4	The Buffer Region	49
2.3.5	The Inner Veto	49
2.3.6	Outer Veto and Shielding	49
2.4	PMT Readout System	50
2.5	The Double Chooz Trigger	52
2.6	Calibration	52
2.7	The Double Chooz Software	52
3	Simulation of Nuclear Fission Reactors with DRAGON	55
3.1	The Neutron Transport Equation and its Deterministic Solution . . .	55
3.1.1	Derivation	56
3.1.2	The Source Density	58
3.1.3	Multigroup Discretization	59
3.1.4	Solution of the Transport Equation	60
3.2	The Lattice Code DRAGON	63
3.2.1	Motivating Lattice Calculations	63
3.2.2	Relevant Features of DRAGON for Reactor Antineutrino Ex- periments	64
4	Simulation of Reactors for Anti-neutrino Experiments Using DRAGON and MURE	67
5	The Double Chooz Antineutrino Flux Prediction and Uncertainty	77
5.1	From EDF Inputs to Antineutrino Flux	77
5.1.1	Producing Fission Rates with EDF Inputs	77
5.1.2	Connection to Experiment: DCRxtrTools	80
5.2	Reactor Simulation Cross-Checks with DRAGON	82
5.2.1	Thermal Power	82
5.2.2	Fission Rate Evolution	83
5.2.3	Assembly-level Systematic Uncertainties with DRAGON . . .	83

5.2.4	k_{eff} Cross-Check	84
5.2.5	Systematic Uncertainty for Fission Rates	84
5.2.6	Anchoring to the Bugey-4 Reactor Experiment	90
5.3	Summary of Reactor Flux Uncertainties	94
6	First Results from Double Chooz	95
6.1	Analysis Overview	95
6.1.1	Candidate Event Selection	95
6.1.2	Backgrounds	96
6.1.3	Selection Efficiencies	99
6.1.4	Detector Energy Scale	101
6.2	Oscillation Fit	102
7	Comparisons and Conclusions	107
7.1	Accelerator Appearance Experiments	107
7.1.1	Results from T2K	107
7.1.2	Results from MINOS	110
7.2	Reactor Disappearance Results	110
7.2.1	Results from the Daya Bay Experiment	110
7.2.2	Results from the RENO Experiment	113
8	Conclusions	117
A	DRAGON Tutorial and Modifications	119
A.1	Code Sample and Tutorial	119
A.2	Linked List Directives	119
A.3	Importing Modules	120
A.4	The LIB: module	120
A.5	Mixtures	121
A.6	Assembly Geometry	124
A.7	Tracking	127
A.8	Self-shielding, Collision Probabilities, and Flux	128

A.9	Fuel Depletion	128
A.10	Modifications for Fission Rates	129
B	Using Antineutrinos For Nuclear Nonproliferation	131
B.1	Neutrino Spectroscopy with Reactors	131
B.2	Close Range Core Monitoring With SONGS1	133
B.2.1	SONGS: Reactor and Detector	133
B.2.2	Data Analysis and Results	135
B.2.3	Fission Rate Prediction from DRAGON	137
B.3	Using the Double Chooz Far Detector for Nonproliferation	139
B.3.1	Illicit Production Scenarios	140
B.3.2	Double Chooz Detector Monte Carlo	141
B.3.3	Non-observation of the Burnup Effect	147
B.3.4	Inference of Diverted Plutonium	147
C	AFA3G Sensitivity Study With DRAGON	151

List of Figures

1-1	Percent deviation of two-neutrino model from three-neutrino model. Here, θ_{13} , θ_{12} , δm_{13}^2 , and δm_{12}^2 were taken from [1], and the baseline was $L = 1050$ m.	21
1-2	Normal and inverted neutrino mass hierachies.	23
1-3	Illustration of a reactor disappearance experiment.	23
1-4	A cutaway drawing of the detector, where the holes show where the PMTs would be mounted. Taken from [2].	24
1-5	Neutron <i>vs.</i> positron energies for neutrino candidates in CHOOZ, from [2].	26
1-6	Left: Positron yields in CHOOZ. Right: Ratio of positron yields from both reactors, compared to the no-oscillation scenario. Taken from [2].	27
1-7	The Palo Verde experiment. One of the neutrino modules is shown at the bottom. Taken from [3].	28
1-8	A neutrino candidate in the Palo Verde experiment from [3].	29
1-9	The Daya Bay experiment. Here, EH = Experimental Hall, AD = Antineutrino Detector, and NPP = Nuclear Power Plant. L1 through L4 represent the Ling Ao reactors, while D1 and D2 are the Daya Bay reactors. Taken from [4].	30
1-10	The RENO experiment.	30
1-11	The T2K ν_μ beam energy spectra. The $P(\nu_\mu \rightarrow \nu_e)$ probability is superimposed with arbitrary units. The ideal off-axis angle of 2.5° is shown, and is easily seen to be near the maximum of the appearance oscillation probability with a very narrow peak. Figure taken from [5].	32

1-12	The NO ν A ν_μ beam energy spectra. The $P(\nu_\mu \rightarrow \nu_e)$ probability is shown on top. The ideal off-axis angle of 0.8° (14 mrad) is shown in red, and is easily seen to be near the maximum of the appearance oscillation probability with a very narrow peak. Figure taken from [6].	33
1-13	The NO ν A detectors.	34
1-14	The antineutrino anomaly. The data points are the reanalyzed results from the very short baseline reactor flux experiments. Taken from [7].	38
2-1	Chooz power plant with Double Chooz detectors.	40
2-2	Illustration of principal components of a PWR.	41
2-3	Assembly example. This image was made with DRAGON. The color purple refers to fuel, faint green refers to cladding, and grey refers to water.	42
2-4	Fission cross sections of some radioactive isotopes. ^{235}U and ^{239}Pu have the largest thermal fission cross section of all elements. ^{238}U only fissions with “fast” neutrons, near 1 MeV.	43
2-5	Empirical energy spectrum of neutrons emitted in fission reactions, assuming that only ^{235}U fissions. The units are probability per unit energy.	43
2-6	Radionuclides involved in the uranium cycle.	45
2-7	Illustration of Double Chooz main detector components.	46
2-8	The buffer region with PMTs.	50
2-9	Schematic of Outer Veto.	51
2-10	Schematic of Double Chooz hardware systems from [8].	51
2-11	Double Chooz software components.	53
3-1	Illustration of self-shielding effects. Image from [9].	64
5-1	Radial contribution factors for each assembly as a function of time. The contributions have all been normalized to their initial value so that what is plotted is in fact the percent deviation.	81

5-2	Example fission rates during a typical fuel cycle.	83
5-3	B1 and B2 thermal power for Cycle 12.	84
5-4	Deviation of reconstructed power from DRAGON for core B2 during Cycle 12.	85
5-5	DRAGON deviation of APOLLO k_{eff} calculation for AFA 3G assem- bly, with and without Gd.	86
5-6	DRAGON deviation of APOLLO AFA 3G simulation without Gd. Units are in MW-day / ton.	87
5-7	DRAGON deviation of APOLLO AFA 3G simulation with Gd. Units are in MW-day / ton.	88
5-8	DRAGON vs. MURE for AFA 3G assembly without Gd: fuel inventory and fission rates.	89
5-9	DRAGON vs. MURE for AFA 3G assembly with Gd: fuel inventory and fission rates.	89
5-10	Fission rate systematic errors as a function of time. The DRAGON result is labeled "Code". From [10].	91
5-11	Fission rate systematic errors as a function of time. The DRAGON result is labeled "Code". From [11].	91
5-12	Fission rate systematic errors as a function of time. The DRAGON result is labeled "Code". From [11].	92
5-13	Fission rate systematic errors as a function of time. The DRAGON result is labeled "Code". From [11].	92
5-14	Fission rate systematic errors as a function of time. The DRAGON result is labeled "Code". From [11].	93
6-1	The MQTQ discriminant on prompt and delayed events. The black points are antineutrino candidates in the coincidence window $4 < \Delta t <$ $100\mu\text{s}$; the red points are a measurement of accidental background by looking at an off-time window of $1\text{ s} + 4\mu\text{s} < \Delta t < 1\text{ s} + 100\mu\text{s}$. From [12].	96

6-2	Scatter plot of prompt and delayed energy for IBD candidates. From [13].	97
6-3	A plot of interevent time between an observed coincidence and the previous muon. From [14].	98
6-4	Prompt energy spectrum of coincidences happening between $40\mu\text{s}$ and $150\mu\text{s}$ after a muon. The Gd and H peaks are visible. The abscissa units are in DUQ ($15020 \text{ DUQ} \approx 1 \text{ MeV}$). From [14].	98
6-5	The accidental spectrum. From [15].	99
6-6	Spill-in and spill-out events. From [16].	100
6-7	Combined fit neutron capture on Gd and H peaks. From [17].	101
6-8	The empirical MC correction function. The reduced $\chi^2 \approx 4$. From [18].	102
6-9	The empirical MC correction function. The reduced $\chi^2 \approx 3$ and 5 for ^{60}Co and ^{137}Cs respectively. From [18].	102
6-10	Data vs. MC rate comparison for the first publication data set, from [95].	104
6-11	Data and best-fit spectra. The measured prompt energy spectra are shown with statistical error bars. The blue dashed line shows the no-oscillation scenario, which is predicted from reactor simulations and detector Monte Carlo. The best-fit spectra is shown in red and is derived from a χ^2 minimization technique. The green band shows the background contributions and are seen in more detail in the inset. . .	105
7-1	Summary of recent measurements of θ_{13} . For each experiment, the value of θ_{13} and its 1σ error is plotted, assuming a gaussian shape. The combined best-fit is also shown. The experiments comprising this plot are [20, 21, 22, 96, 77].	108
7-2	Energy spectrum of reconstructed neutrinos at T2K far detector. The blue line shows the 1.25 GeV energy cut. Taken from [19].	109
7-3	Top: MC vs. data for the MINOS near detector, with systematic uncertainty shaded in red. Bottom: Background and signal as function of the LEM discriminant, assuming $\sin^2 2\theta_{13} = 0.1$. Taken from [20].	111

7-4	MINOS best-fit value at the far detector with multiple values of the LEM discriminant. Taken from [20].	112
7-5	Top: The measured positron spectrum from the far hall compared to the no-oscillation expectation from the near halls. Bottom: ratio of far hall prediction to the no-oscillation scenario. Taken from [21].	114
7-6	Top: distortion of the positron energy spectrum in RENO. Bottom: ratio of far detector prediction to no-oscillation scenario. Taken from [22].	115
B-1	Energy spectrum of detected reactor antineutrinos.	132
B-2	SONGS Unit 2 core map. Each square is a fuel assembly. The blue fuel is fresh, the yellow fuel has passed through one fuel cycle, and the red fuel has been through two fuel cycles. Taken from [23].	134
B-3	SONGS Unit 2 assembly. This is a CE design. Taken from [23].	134
B-4	The SONGS detector location in the core. The red circle locates the detector in the reactor tendon gallery. Taken from [23].	135
B-5	The SONGS1 antineutrino detector. Taken from [23].	136
B-6	A sample interevent spectrum from SONGS1. Taken from [24].	136
B-7	Observation of antineutrino changes due to fuel evolution and reloading. The top frame shows the Unit 2 thermal power; the middle frame shows a clear tracking of the antineutrino rate; the bottom frame shows a zoom-in to the middle frame to make the change more clearly visible. Taken from [24].	137
B-8	DRAGON prediction of SONGS thermal power.	138
B-9	DRAGON fission rate prediction for SONGS.	138
B-10	DRAGON rate prediction with SONGS1 data. The time axis shows the number of days into the current fuel cycle.	140
B-11	Neutron flux for the three scenarios.	142
B-12	Total fission rate for the three scenarios.	142
B-13	^{235}U fission rate for the three scenarios.	143

B-14	^{238}U fission rate for the three scenarios.	143
B-15	^{239}Pu fission rate for the three scenarios.	144
B-16	^{241}Pu fission rate for the three scenarios.	144
B-17	^{235}U inventory for the three scenarios.	145
B-18	^{238}U inventory for the three scenarios.	145
B-19	^{239}Pu inventory for the three scenarios.	146
B-20	^{241}Pu inventory for the three scenarios.	146
B-21	Comparison of two spectra separated by 1 month.	147
B-22	Scenario spectra.	148
B-23	Scenario spectra with 1% energy scale uncertainty band.	149
C-1	Assembly-level sensitivity study of AFA 3G APOLLO simulation with DRAGON.	152
C-2	Assembly-level sensitivity study of AFA 3G APOLLO simulation with DRAGON.	152
C-3	Assembly-level sensitivity study of AFA 3G APOLLO simulation with DRAGON.	154
C-4	Assembly-level sensitivity study of AFA 3G APOLLO simulation with DRAGON.	155

List of Tables

1.1	Neutrino oscillation experiment sensitivities to Δm^2 , taken from [1]. Note that solar neutrinos have significant matter effects. The abbreviations “SB” and “LB” refer to “short-baseline” and “long-baseline”, respectively.	19
1.2	Summary of solar and atmospheric neutrino experiments [1, 25]. This is a global fit assuming a 3ν model. The solar experiments include SNO-III[26], GALLEX[27], and Borexino[28].	20
1.3	Very short baseline reactor data. The old and new ratios are $N_{measured}/N_{predicted}$, where the predictions contain no oscillation effect [29, 7]	36
5.1	Fission rate variations, taken from [11].	90
5.2	Reactor antineutrino signal uncertainty, taken from [30].	94
6.1	Detector-related uncertainties, taken from [30].	103
6.2	Far detector backgrounds, taken from [30].	103
B.1	Energy released per fission used by the DRAGON code, from [31].	138
B.2	SONGS simulations for DRAGON.	139
B.3	Detector parameters for the SONGS antineutrino flux prediction. Taken from [32].	139
B.4	Fit parameters for the S_k , taken from [33].	140
B.5	Comparison of SONGS and Double Chooz Far Detector.	141
B.6	Fuel inventories at end of simulation for each scenario, in metric tons.	141
C.1	Parameter variations for fission rates.	151

C.2	AFA-3GL fission rate percent variations at day 362 of simulations (burnup = 14315 MWd/T)	153
C.3	Fresh fuel AFA-3GL errors: B1	153

Chapter 1

Introduction and Motivation

The neutrino is an exceedingly unusual particle. This is still an understatement, even in a world where we have cloistered quarks, virtual photons, and triply-strange baryons. Like shape-shifting ghosts, they permeate the universe and remain largely transparent to it. They are carriers of the weak force, without them there would be no thermonuclear fusion, no sun. They exhibit the *purest* interactions of all phenomena in Nature: they only interact via the weak force, and remain stable modulo oscillations into other neutrino flavors. This thesis discusses the effort undertaken by Double Chooz, a reactor antineutrino disappearance experiment, to determine θ_{13} , the final unknown parameter describing the phenomena of neutrino oscillations. As Double Chooz is a reactor experiment, it is a spiritual descendent of the original reactor experiments that discovered the neutrino. It is only fitting that Double Chooz also provide one of the first measurements of this mixing angle.

The layout of this work is as follows. In this chapter, we discuss a brief history of neutrino oscillations and the search for θ_{13} , including the results of previous reactor antineutrino experiments and their constraints on the mixing angle. In Chapter 2, the Double Chooz experiment is discussed, along with a brief survey of the similar Daya Bay and RENO experiments. In Chapter 3, the theory of reactor simulations relevant to antineutrino experiments, in particular the DRAGON simulation code, is discussed. In Chapter 4, we show the result of the Takahama-3 benchmark, which validates our use of DRAGON for simulating the Chooz reactors. In Chapter 5,

we discuss the calculation of the antineutrino flux using the DRAGON code, and in Chapter 6, we show the first determination of θ_{13} from the Double Chooz experiment, along with the calculation of the systematic uncertainty due to the reactor. The final chapter compares the Double Chooz result with those from other θ_{13} experiments, including MINOS, T2K, Daya Bay and RENO.

This work contains two appendices. In the first, we provide a sample input file for the DRAGON code along with extended annotation. In the second appendix, we outline a method using detected antineutrinos to perform a real-time assay of reactor fuel. The Double Chooz Monte Carlo coupled with DRAGON predictions is used to determine the feasibility of this method for nonproliferation efforts. This chapter begins with a review of neutrino oscillations and proceeds to a discussion of the current limits set on θ_{13} .

1.1 The Oscillating Leptons

In the past two decades, ample evidence for the neutrino oscillation hypothesis has been collected and confirmed by several key experiments [34, 35, 36]. The discussion of the phenomenon is due to Maki, Nakagawa, and Sakata [37] as well as Pontecorvo [38]. To motivate the predictions, let us assume, unlike in the Standard Model, that the neutrinos have a nonzero rest mass. It is then possible that the weak eigenstates and the mass eigenstates are not identical. The two sets of states could be connected by a unitary transformation, similar to the CKM matrix in the quark sector. We will see that observation of neutrino oscillations require at least one nonzero and non-degenerate mass eigenstate.

We will compute the amplitude and probability for oscillations by assuming 1D plane-wave states for simplicity; these results will hold even with a more sophisticated derivation using wave packets [39]. The following derivation follows [40] and only derives oscillations in vacuum. A more detailed discussion, including matter effects [41] can be found in [42, 43]. Let $|\nu_i\rangle$ be the mass eigenstates prepared at $x = 0$ and $|\nu_\alpha\rangle$ be the flavor eigenstates. These states are orthonormal, so we have $\langle\nu_i|\nu_j\rangle = \delta_{ij}$.

We can construct a unitary matrix U , the PMNS matrix, to connect the two sets of states:

$$|\nu_\alpha(x, t = 0)\rangle = \sum_i U_{\alpha i} |\nu_i(x, t = 0)\rangle \quad (1.1)$$

$$|\nu_i(x, t = 0)\rangle = \sum_\alpha U_{i\alpha}^* |\nu_\alpha(x, t = 0)\rangle. \quad (1.2)$$

The mass eigenstates by construction commute with the Hamiltonian, so we know their evolution for arbitrary time t , and since they are plane wave states, they are momentum eigenstates as well:

$$\begin{aligned} |\nu_i(x, t)\rangle &= e^{-iHt} |\nu_i(x, t = 0)\rangle = |\nu_i(x, t = 0)\rangle e^{-iE_i t} \\ &= |\nu_i\rangle e^{ip_i x - iE_i t}. \end{aligned} \quad (1.3)$$

Now we can write an arbitrary neutrino state at position x and time t in terms of flavor eigenstates:

$$\begin{aligned} |\nu(x, t)\rangle &= \sum_i U_{\alpha i} |\nu_i\rangle e^{ip_i x - iE_i t} \\ &= \sum_i U_{\alpha i} U_{\beta i}^* |\nu_\beta\rangle e^{ip_i x - iE_i t}. \end{aligned} \quad (1.4)$$

Since these neutrinos are ultra-relativistic, we have $E_i = \sqrt{p_i^2 + m_i^2} \approx p_i + \frac{m_i^2}{2p_i} \approx E + \frac{m_i^2}{2E}$. Here, we have assumed that the mass eigenstate energy E_i does not differ too much from that of the weak eigenstate, E . In units where $c = 1$, we have $x = ct = t$. We can then use the above expression to write the amplitude for transitions from flavor α to β at a distance L from the production point:

$$\begin{aligned} A_{\alpha \rightarrow \beta} &= \langle \nu_\beta | \nu(x, t) \rangle \\ &= \sum_i U_{\alpha i} U_{\beta i}^* e^{-i \frac{m_i^2}{2E_i} L} \end{aligned} \quad (1.5)$$

Source	Type	E (MeV)	L (km)	Δm^2 (eV ²)	Examples
Reactor (SB)	$\bar{\nu}_e$	~ 1	1	10^{-3}	CHOOZ
Reactor (LB)	$\bar{\nu}_e$	~ 1	100	10^{-5}	KamLAND
Accelerator (SB)	$\bar{\nu}_\mu, \nu_\mu$	$\sim 10^3$	1	1	MINOS
Accelerator (LB)	$\bar{\nu}_\mu, \nu_\mu$	$\sim 10^3$	10^3	10^{-3}	No ν A
Atmospheric	$\bar{\nu}_{e,\mu}, \nu_{e,\mu}$	$\sim 10^3$	10^4	10^{-4}	Super-K
Solar	ν_e	~ 1	1.5×10^8	$\sim 10^{11}$	SNO

Table 1.1: Neutrino oscillation experiment sensitivities to Δm^2 , taken from [1]. Note that solar neutrinos have significant matter effects. The abbreviations “SB” and “LB” refer to “short-baseline” and “long-baseline”, respectively.

We can find the squared modulus of this amplitude to get the probability of transition from $\alpha \rightarrow \beta$ [40]:

$$P_{\alpha \rightarrow \beta} = \sum_i |U_{\alpha i} U_{\beta i}^*|^2 + 2 \cdot \text{Re} \sum_{j>i} U_{\alpha i} U_{\alpha j}^* U_{\beta i}^* U_{\beta j} \exp\left(-i \frac{\Delta m_{ij}^2 L}{2E}\right). \quad (1.6)$$

where $\Delta m_{ij}^2 \equiv m_i^2 - m_j^2$ is the mass-squared difference. The oscillatory nature of the probability is evident.

From expression 1.6, we see that neutrino oscillations require at least one eigenstate possessing nonzero mass and non-diagonal terms in the PMNS matrix. It is the experimentalist’s goal to determine the entries of the PMNS matrix and the values of the m_i . We cannot learn the absolute values of the m_i with neutrino oscillations since we can only measure the differences Δm_{ij}^2 . It is also crucial to note the dependence of the oscillation probability on L/E ; this will drive the design of neutrino oscillation experiments. Neutrino oscillation effects are most noticeable when the phase of the transition probability is large; i.e., $\frac{\Delta m^2 L}{E} \approx \pi/2$, or $\Delta m^2 \sim E/L$. In Table 1.1, we show the values of Δm^2 that can be explored in a variety of experiments with neutrino sources of different energies.

1.2 Parameterizing the PMNS Matrix

With the three known neutrino flavors (e, μ , and τ), the PMNS matrix becomes a 3×3 unitary matrix which connects the flavor eigenstates with the three mass eigenstates: $|\nu_1\rangle, |\nu_2\rangle$, and $|\nu_3\rangle$. We can parameterize the matrix using three mixing angles θ_{12}, θ_{23} , and θ_{13} . The angle labels describe the transitions between mass eigenstates, so for example, θ_{13} parameterizes transitions between $|\nu_1\rangle$ and $|\nu_3\rangle$. In terms of these angles, the PMNS matrix can be written as $U = U_{23} \cdot U_{13} \cdot U_{12}$, or:

$$\begin{pmatrix} 1 & 0 & 0 \\ 0 & \cos \theta_{23} & \sin \theta_{23} \\ 0 & -\sin \theta_{23} & \cos \theta_{23} \end{pmatrix} \begin{pmatrix} \cos \theta_{13} & 0 & \sin \theta_{13} e^{-i\delta} \\ 0 & 1 & 0 \\ -\sin \theta_{13} e^{i\delta} & 0 & \cos \theta_{13} \end{pmatrix} \begin{pmatrix} \cos \theta_{12} & \sin \theta_{12} & 0 \\ -\sin \theta_{12} & \cos \theta_{12} & 0 \\ 0 & 0 & 1 \end{pmatrix} \quad (1.7)$$

Different oscillation experiments reveal different entries in this matrix. Experiments involving atmospheric neutrinos or accelerator neutrinos [34, 20, 19] measure Δm_{23}^2 and θ_{23} , and solar neutrino experiments and long baseline reactor experiments [36, 35] determine Δm_{12}^2 and θ_{12} . Thus, the matrices in the above expression are often labeled with the type of experiment that primarily probes for that mixing angle: $U_{12} \equiv U_{\text{solar}}$, $U_{23} \equiv U_{\text{atmospheric}}$, and $U_{13} \equiv U_{\text{reactor}}$. Strictly speaking, U_{13} is not solely determined from reactor experiments; as we will see later in this chapter, accelerator experiments can also probe for θ_{13} . In this parameterization, we have also included the CP -violating phase, δ . It is clear that if CP -violation is to be observed in the lepton sector, then $\sin \theta_{13}$ must be nonzero.

Despite the fact that there are three known flavors of neutrinos, a two-neutrino oscillation model is often used to simplify the interpretation of experiments. In this scenario, there is only one mixing angle θ . This simplifies the rotated states and probability of oscillation considerably:

$$\begin{pmatrix} \nu_\alpha \\ \nu_\beta \end{pmatrix} = \begin{pmatrix} \cos \theta & \sin \theta \\ -\sin \theta & \cos \theta \end{pmatrix} \begin{pmatrix} \nu_1 \\ \nu_2 \end{pmatrix} \quad (1.8)$$

θ	Best Fit $\sin^2 \theta$	Best Fit Δm^2 [eV ²]	Determined from
θ_{12}	$0.312^{+0.018}_{-0.015}$	$7.58^{+0.22}_{-0.26} \times 10^{-5}$	Super-K, SNO, KamLAND
θ_{23}	$0.42^{+0.08}_{-0.03}$	$2.35^{+0.12}_{-0.09} \times 10^{-3}$	Super-K, MINOS

Table 1.2: Summary of solar and atmospheric neutrino experiments [1, 25]. This is a global fit assuming a 3ν model. The solar experiments include SNO-III[26], GALLEX[27], and Borexino[28].

$$P_{\alpha \rightarrow \beta} = \sin^2 2\theta \sin^2 \left(1.27 \frac{\delta m^2 L}{E_\nu} \right) \quad (1.9)$$

Here, $\delta m^2 \equiv m_\beta^2 - m_\alpha^2$. From this model and from experiments listed in Table 1.1, two distinct mass scales have emerged: the solar mass scale and the atmospheric mass scale; see Table 1.2. The fact that the two-neutrino oscillations are adequate can be seen from the a more detailed three-neutrino calculation for reactor experiments at a baseline of $O(1)$ km, or short baseline (SB) [44]:

$$P_{SB} = \sin^2 2\theta_{13} \sin^2 \left(1.27 \frac{\delta m_{13}^2 L}{E_\nu} \right) + \chi^2 \left(1.27 \frac{\delta m_{13}^2 L}{E_\nu} \right)^2 \cos^4 \theta_{13} \sin^2 \theta_{12} \quad (1.10)$$

Here, $\chi \equiv \delta m_{21}^2 / \delta m_{23}^2 \approx 0.032$. In Figure 1-1, we show the percent deviation of the two-neutrino scenario from the three-neutrino scenario. Above threshold, this effect is less than 0.05%. Thus we see that the two-neutrino oscillation scenario is adequate for a reactor antineutrino experiment such as Double Chooz. With this model in mind, we now turn to the experimental determination of the final unmeasured mixing angle, θ_{13} .

1.3 The Search For θ_{13}

The previous generation of reactor antineutrino experiments, namely CHOOZ [2] and Palo Verde [3] were able to place upper limits on the value of θ_{13} . Aside from satisfying general scientific inquiry, determining this angle is important because its value is needed in any calculation involving electron-neutrinos, from the absolute mass scale to the effective Majorana mass of the ν_e . As was mentioned previously,

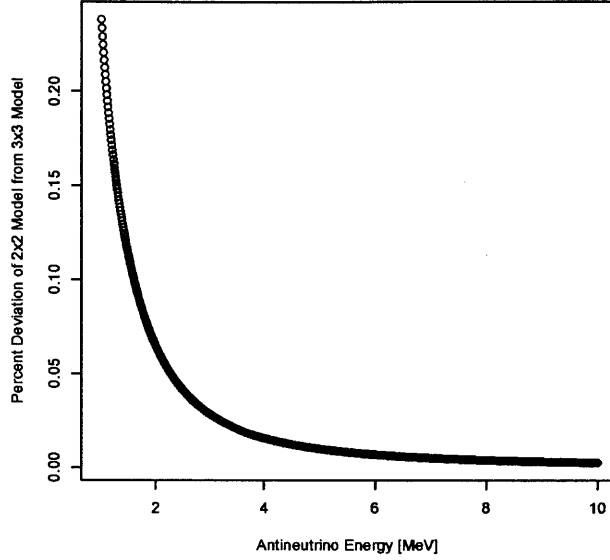


Figure 1-1: Percent deviation of two-neutrino model from three-neutrino model. Here, θ_{13} , θ_{12} , δm_{13}^2 , and δm_{12}^2 were taken from[1], and the baseline was $L = 1050$ m.

if θ_{13} is nonzero, this allows for the possibility of measuring the CP -violating phase δ_{CP} and thus observing CP violation in the lepton sector, an exciting possibility. Indeed, experiments are underway to measure this phase [45]. The observation of CP -violation in the lepton sector is particularly interesting and might shed some light on the origins of the matter-antimatter asymmetry in the universe. We can search for the phase δ_{CP} using a $O(100)$ km baseline experiment: [44, 45]

$$\begin{aligned}
 P_{long-baseline} &= \sin^2 2\theta_{13} \sin^2 \theta_{23} \sin^2 \Delta & (1.11) \\
 &\mp \chi \sin 2\theta_{13} \sin \delta_{CP} \cos \theta_{13} \sin 2\theta_{12} \sin 2\theta_{23} \sin^3 \Delta \\
 &+ \chi \sin 2\theta_{13} \cos \delta_{CP} \cos \theta_{13} \sin 2\theta_{12} \sin 2\theta_{23} \cos \Delta \sin^2 \Delta \\
 &+ \chi^2 \cos^2 \theta_{23} \sin^2 2\theta_{12} \sin^2 \Delta
 \end{aligned}$$

Here, $\Delta \equiv \Delta m_{31}^2 L/4E_\nu$ and χ is as defined in the previous section. In the expression above, the minus sign refers to neutrinos and the plus sign refers to antineutrinos.

Thus, one way to search for CP -violation is to run an experiment in both neutrino and antineutrino modes and look for differing appearance rates. Once again, this program depends on θ_{13} being not only nonzero, but sufficiently large in order to see these differing rates.

Even though two distinct mass scales have emerged from the results of previous experiments, neutrino oscillation experiments can only tell us of their relative scales; see Figure 1-2 for an illustration. The KATRIN experiment[46] is searching for absolute mass scale via a tritium endpoint measurement. However, long-baseline oscillation experiments can resolve whether the mass hierarchy is normal or inverted as shown in 1-2.

Reactor antineutrino experiments, such as Double Chooz[47], Daya Bay[48], and RENO[49] seek to measure θ_{13} by measuring antineutrino disappearance, as explained in Section 1.4.1. The accelerator experiments MINOS[20], T2K[19], and NO ν A[50] are sensitive to θ_{13} as well as to δ_{CP} and the mass hierarchy. Precise measurements of θ_{13} from the reactor experiments improve the ability of accelerator experiments to measure δ_{CP} or the mass hierarchy. We begin with a survey of the CHOOZ and Palo Verde experiments, and then discuss the current generation of experiments.

1.4 A Summary of Recent Reactor Antineutrino Experiments

1.4.1 Disappearance Experiments

Reactor antineutrino experiments all use very similar detection principles, and since Chapter 2 examines the Double Chooz detector in detail, we postpone a full discussion until that point. We illustrate a very basic disappearance experiment searching for θ_{13} in Figure 1-3. Antineutrinos from the reactor will, over a distance of approximately 1 km, oscillate into other flavors, and the $\bar{\nu}_e$ detector counts the depleted number of antineutrinos. For experiments like CHOOZ, Palo Verde, or the single-detector phase of Double Chooz, whose first results we will see in Chapter 6, there is only a

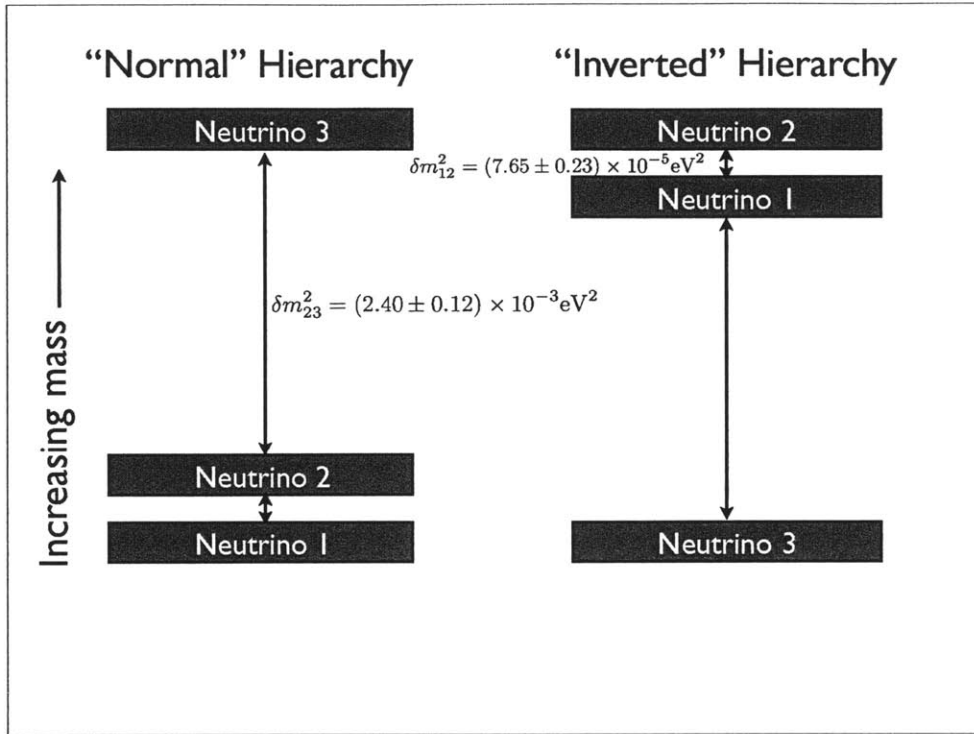


Figure 1-2: Normal and inverted neutrino mass hierachies.

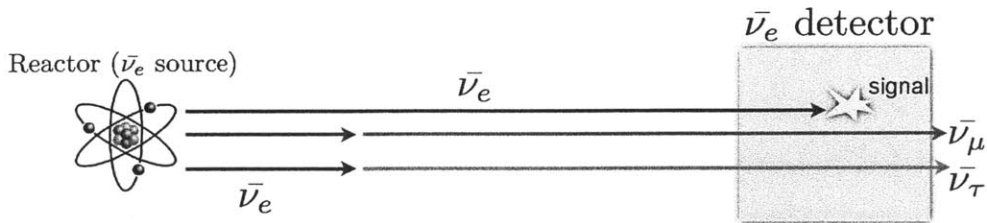


Figure 1-3: Illustration of a reactor disappearance experiment.

far detector located at the 1 km oscillation maximum; to obtain the number of antineutrinos that were emitted by the reactor (the so-called unoscillated flux), detailed reactor simulations must be performed. A major component of the work presented in this thesis is dedicated to predicting this unoscillated antineutrino flux.

For Daya Bay and RENO, data taking involves at least 2 detectors from the beginning. The near detector(s) normalize the flux, and then only small simulation-based corrections of the contribution of each reactor are needed. The detection mechanism used is inverse β decay in a Gd-doped liquid scintillator. This produces a coincidence signal of a prompt positron annihilation followed by the delayed neutron capture on Gd in $\sim 30\mu\text{s}$.

1.4.2 The CHOOZ Experiment

1.4.2.1 Detector Design

The CHOOZ experiment took place from April 1997 to July 1998 in the French village Chooz. CHOOZ searched for antineutrino disappearance. The single detector was located approximately 1 km from the Chooz B1 and B2 reactors, and 300 meters of water equivalence (m.w.e.) underground. The depth of the detector reduced critical backgrounds due to the muon flux by a factor of 300 [2]. Details of the B1 and B2 reactors will be discussed in Chapter 2. Figure 1-4 shows an image of the detector's internal regions. The design of the CHOOZ detector is typical of reactor antineutrino detectors.

- Region I, the innermost region, was the neutrino target. It contained 5 tons of gadolinium-doped (Gd-doped) liquid scintillator. The Gd is useful since it reduces the capture time of the neutron from $180\mu\text{s}$ to approximately $30\mu\text{s}$, which reduces the likelihood of backgrounds from false coincidences. In addition, the neutron capture on Gd produces an ≈ 8 MeV-gamma ray cascade with energies well above those of background events (< 4 MeV).
- Region II surrounded Region I and it contained 107 tons of undoped liquid scintillator. Region II's purpose was to capture escaping electromagnetic energy; it

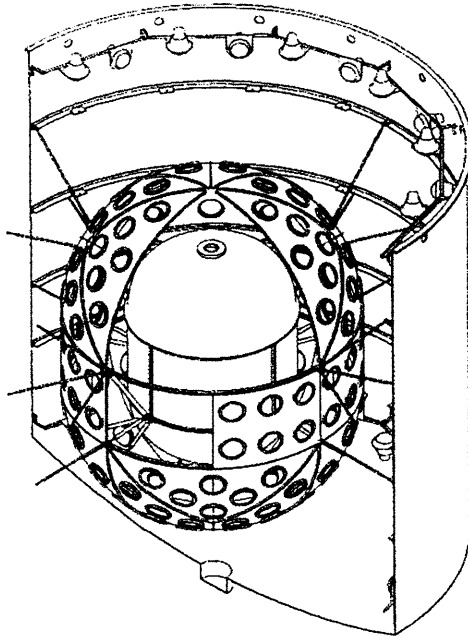


Figure 1-4: A cutaway drawing of the detector, where the holes show where the PMTs would be mounted. Taken from [2].

was 99% efficient in catching positrons from $\bar{\nu}$ reactions, and approximately 95% efficient in capturing gamma radiation for neutron capture on Gd [2]. Region II contained 192 center-facing PMTs to catch scintillator light.

- Region III was the veto region. Like Region II, it contained undoped scintillator; however, it only used 48 PMTs. Its purpose was to reject cosmic muons and to shield the target against the natural radioactivity from the surrounding rock.
- The detector was housed in a steel vessel with a diameter of 5.5 m, which, in turn, was surrounded by 75 cm of low-radioactivity sand and 14 cm of cast iron for shielding purposes.

The detector contained laser flashers and pipes for the introduction of radioactive sources for calibration. In fact, it was found that the attenuation length of the scintillator decreased as a function of time due to oxidation from nitrate ions, making periodic calibrations extremely important.

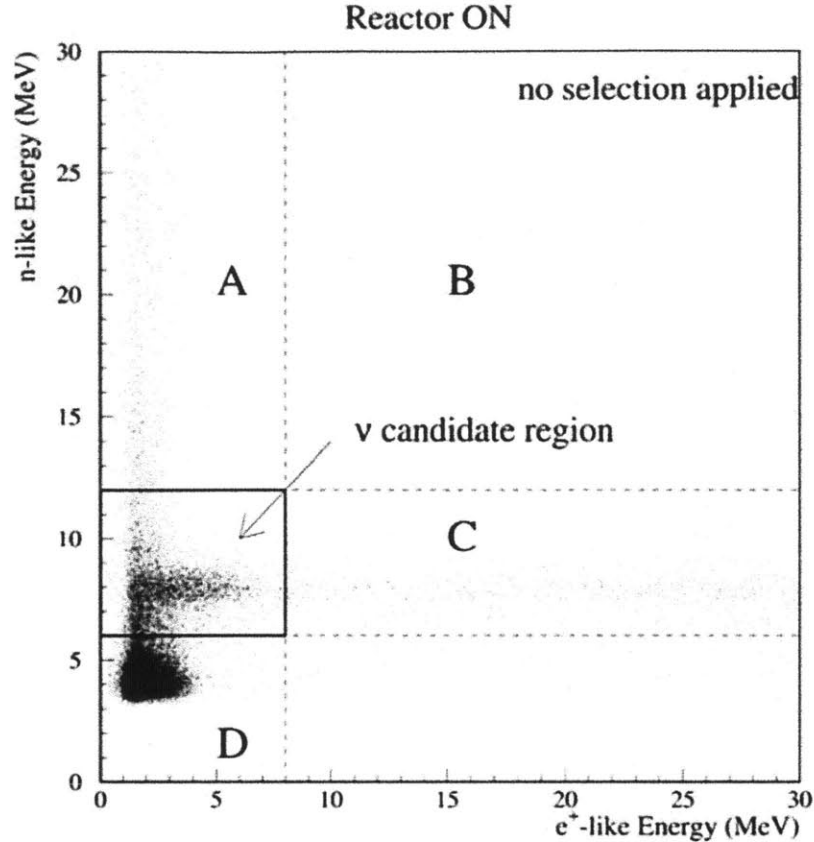


Figure 1-5: Neutron *vs.* positron energies for neutrino candidates in CHOOZ, from [2].

1.4.2.2 Event Selection and Backgrounds

In Figure 1-5, we show the various event classes encountered by the CHOOZ experiment plotted as a function of prompt e^+ -like events versus delayed n -like events. The discussion of these classes follows that given in [2]. Events in Class C showed the 8 MeV Gd capture peak that persisted even when the two reactors were shut down. These events could then be taken to be spallation neutrons created by muons passing through the nearby rock. In this case, the neutron entered the detector and transferred its large kinetic energy to protons. This proton recoil mimicked a prompt positron. The neutron then captured on Gd as in inverse β decay. This is called correlated background. In contrast, Classes A and D showed uncorrelated background.

The low-energy positron-like event most likely came from ambient radioactivity, which had energies less than 4 MeV. The associated neutron-like energy could have been from spallation neutrons (Class A) or another radioactivity signal (Class D). The events in Class B showed high positron- and neutron-like energies. These could be accounted by the presence of stopping muons. These muons penetrated into the detector about 10 or 20 cm; the ionization created the prompt event. The muon then stops and decays, producing a high-energy Michel electron which mimicked the neutron signal. We will show the candidate region with Double Chooz data in Chapter 6.

1.4.2.3 Results

CHOOZ observed 2991 antineutrino candidate events with a total live time of 340 days. In February 1998, both reactors were shut down; by July 1998 when data taking ceased, the reactor-off period accounted for 40% of the live time. 287 candidate events occurred during the reactor-off period. To reduce the uncertainty in the reactor flux measurement, the CHOOZ experiment used the Bugey-4 reactor flux measurement[51]. The experiment reported the ratio of detected to expected (no-oscillation) events:

$$R = 1.01 \pm 2.8\%(stat.) \pm 2.7\%(syst.)$$

A nonzero value of θ_{13} should lead to a shape modification and overall deficit of the detected positron spectrum. In Figure 1-6, we show the detected spectrum from each reactor for CHOOZ. It is seen that both spectra are consistent with no neutrino oscillations, and this is confirmed by a Kolmogorov-Smirnov test which yielded a compatibility probability of 82%. Thus only an upper limit can be placed on the value for $\sin^2(2\theta_{13})$: $\sin^2(2\theta_{13}) < 0.15$. This upper bound sets the stage for more precise measurements of the final unknown mixing angle.

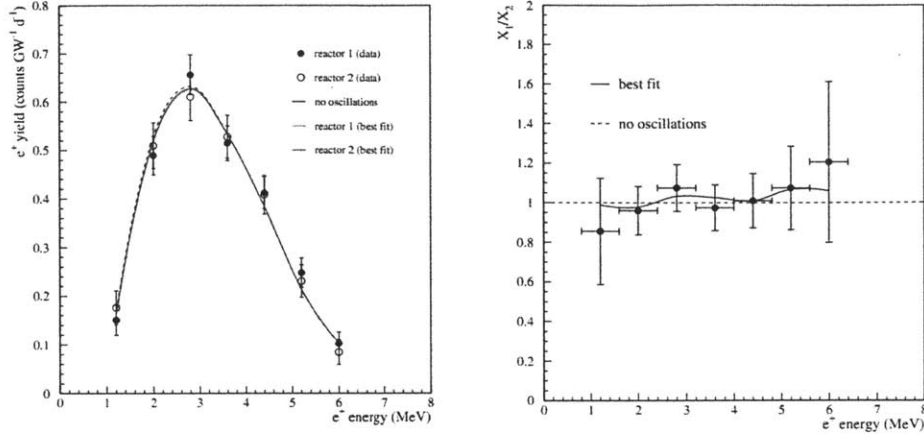


Figure 1-6: Left: Positron yields in CHOOZ. Right: Ratio of positron yields from both reactors, compared to the no-oscillation scenario. Taken from [2].

1.4.3 The Palo Verde Experiment

The Palo Verde experiment [3] took data over a period of 353 days from July 1998 to July 2000 in Arizona. It observed antineutrino interactions from the Palo Verde Nuclear Generating Station, which consists of 3 reactors. The detector was 890 m from two of the reactors and 750 m from the third. The experiment had a 32 m.w.e overburden and is distinguished from CHOOZ by its segmented cell design. The detector is shown in Figure 1-7 and will now be described, following [52]. The central component of the detector consisted of an inner target, made up of 66 detection cells. Each detection module contained liquid scintillator composed of pseudocumene, mineral oil, alcohol, and doped with Gd. At either end of the cell was a mineral oil buffer, and a PMT was attached for light readout. The target contained 11 tons of liquid scintillator and took up a volume of $900 \text{ cm} \times 12.7 \text{ cm} \times 25.4 \text{ cm}$. The target region is surrounded by a 105-ton water buffer, which captured gamma rays and neutrons from the surrounding rock. Finally, the water buffer was surrounded by a muon veto.

The antineutrino signal used inverse beta decay, described in more detail in Chapter 2. However, it is worth noting here that the delayed coincidence signal in Palo Verde consisted of finding triple spatial coincidences, or “triples”, which could either

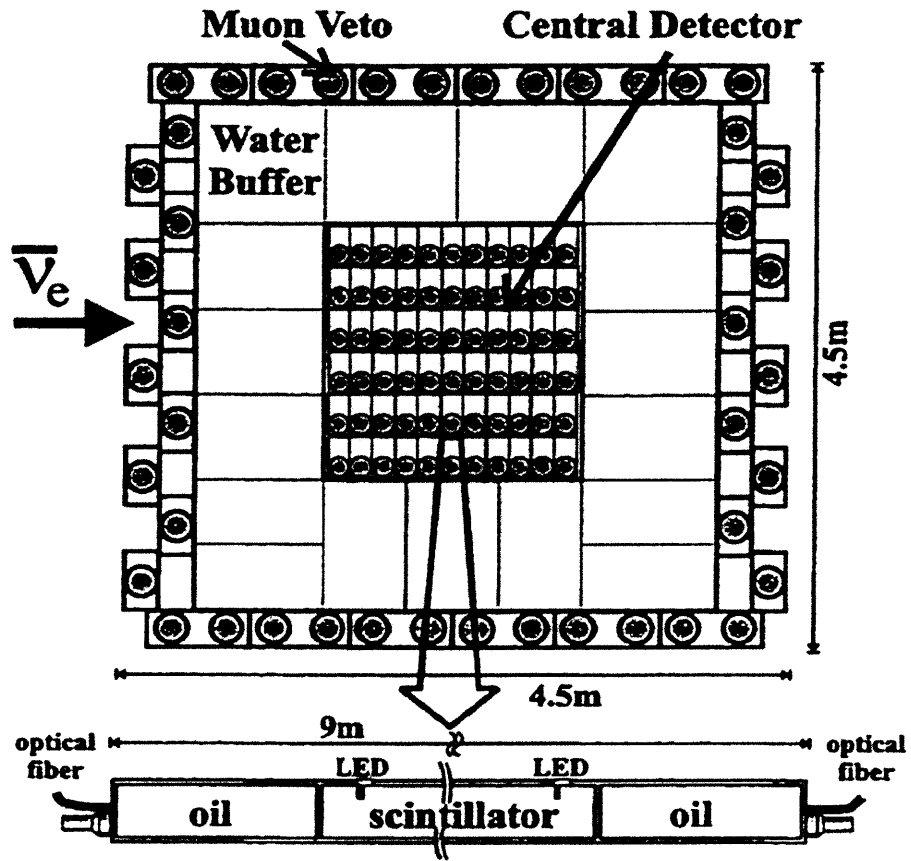


Figure 1-7: The Palo Verde experiment. One of the neutrino modules is shown at the bottom. Taken from [3].

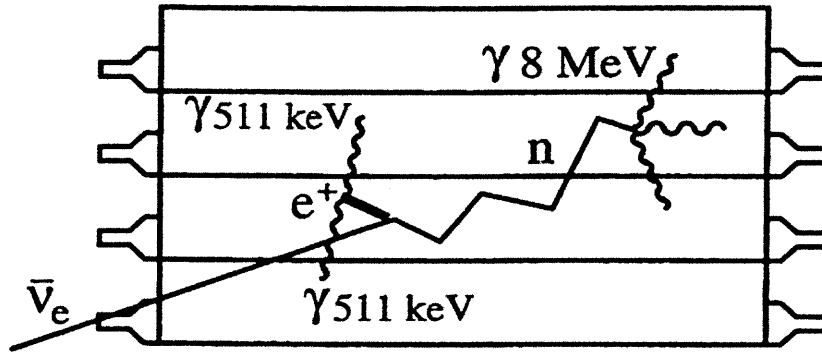


Figure 1-8: A neutrino candidate in the Palo Verde experiment from [3].

be positron-like interactions (ionization by the positron plus 2 photon annihilation) or neutron-like (neutron capture on Gd releasing about 3 gamma rays). Each triple signal had to take place in a different cell, and if they were $450 \mu\text{s}$ apart, they could be counted as a candidate event. A schematic is shown in Figure 1-8. The types of background seen in the experiment are the same as those discussed in the CHOOZ detector section. Like the CHOOZ experiment, Palo Verde used the Bugey reactor flux measurement to reduce the uncertainty of their calculation of the flux. The experiment took data for 353 days reported a ratio of detected to expected events:

$$R = 0.982 \pm 2.3\%(stat.) \pm 5.3\%(syst.)$$

The result is dominated by systematic uncertainty and, like CHOOZ, the experiment saw no evidence for neutrino oscillations[52], and the limit on θ_{13} was $\sin^2(2\theta_{13}) < 0.162$ [3].

1.4.4 Daya Bay & RENO

Like Double Chooz, Daya Bay and RENO are current-generation reactor antineutrino experiments. We outline the improvements of these current-generation experiments over CHOOZ and Palo Verde in the next chapter. The Daya Bay experiment actually

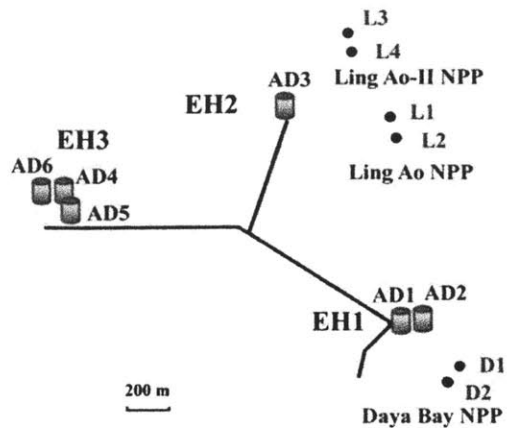


Figure 1-9: The Daya Bay experiment. Here, EH = Experimental Hall, AD = Antineutrino Detector, and NPP = Nuclear Power Plant. L1 through L4 represent the Ling Ao reactors, while D1 and D2 are the Daya Bay reactors. Taken from [4].

consists of three reactor sites in China, north of Hong Kong: “Daya Bay”, “Ling Ao I”, and “Ling Ao II” [48, 4]. Each of these sites has two 2.9 GW (thermal power) reactors. The experiment has two “near halls” called “Daya Bay Near Hall” and “Ling Ao Near Hall”, and a “Far Hall”. At each of the two near halls, there will be two 20-ton antineutrino detectors. The Far Hall will contain 4 20-ton detectors to account for the diminished reactor flux. The near detectors are between 400 - 500 meters from the reactors that they monitor, whereas the 4 far detectors will be between 1500 and 2000 meters from the Ling Ao and Daya Bay halls [4]; see Figure 1-9 for an illustration of the experimental setup. The RENO experiment, on the other hand, consists of 6 reactors at the Yonggwang power plant on the west coast of South Korea. They are lined up over a span of 1300 meters, producing a total of 16.4 GW [53, 49]. The experiment consists of 2 identical detectors: a near detector placed close to the center of this reactor array at a baseline of approximately 300 meters, and a far detector at a distance of 1.4 km; see Figure 1-10 for an illustration. The results of these experiments will be shown in Chapter 7.

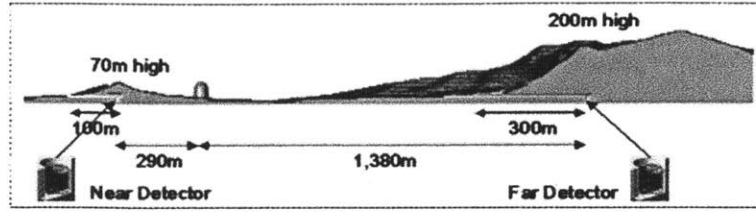


Figure 1-10: The RENO experiment.

1.4.5 Appearance Experiments

1.4.5.1 MINOS

The main goal of the MINOS experiment at Fermilab [54] was to perform precision measurements of the atmospheric neutrino oscillation parameters θ_{23} and Δm_{23}^2 . The experiment detects neutrinos in the ~ 3 GeV range emerging from the NuMI neutrino beam, which in turn was created from 120 GeV protons from the Main Injector. The protons strike a graphite target, producing mostly pions and kaons that decay mostly into muon-type neutrinos. Before the pions and kaons decay, an electromagnetic horn selects the desired sign of the charged mesons. MINOS has a 0.98 kiloton near detector located 1.04 km from the beam source for absolute flux measurements and cross section measurements, and a 5.4 kiloton far detector located 735 km away in the Soudan mine. The detectors themselves are made of alternating sheets of steel and scintillator; the scintillator strips are read out with PMTs and optical fibers [20]. The experiment is sensitive to θ_{13} through ν_e appearance:

$$P(\nu_\mu \rightarrow \nu_e) \approx \sin^2 2\theta_{13} \sin^2 2\theta_{23} \sin^2(1.27\Delta m^2 L/E).$$

MINOS looks for an excess of ν_e events above the expected contamination of $\sim 10^{-4}$, which would occur irrespective of neutrino oscillations. We will present these results in Chapter 5.

1.4.5.2 T2K

The T2K experiment [19, 55] is an off-axis appearance experiment whose primary goal is the measurement of θ_{13} . Protons at 30 GeV strike a graphite target and give rise to the J-PARC beam in Tokai, Japan. The far detector in this case is the water Cerenkov detector Super Kamiokande, 295 km from the target. The near detector is 280 m from the target. Both detectors are 2.5° off-axis relative to the beam. This is done because the ν_μ energy spectrum is peaked at the same energy (≈ 0.6 GeV) of the maximum of the $\nu_\mu \rightarrow \nu_e$ appearance probability, as shown in Figure 1-11. The T2K near detector, called ND280, measures the emitted neutrino flux and counts the ν_e contamination. In addition to the near and far detectors, there is a suite of on-axis iron-scintillator detectors called INGRID that monitors the neutrino beam. There are also proton beam monitors, target monitors, and magnet horn monitors. We will discuss the results from T2K in Chapter 7.

1.4.5.3 NO ν A

Like the T2K experiment, the NO ν A experiment [50] is an off-axis appearance experiment, searching for the $\nu_\mu \rightarrow \nu_e$ reaction. However, its experimental goal is the measurement of θ_{13} and, if the mixing angle is large enough, a resolution of the neutrino mass hierarchy. It also uses the NuMI beam, albeit at higher beam power (700 kW). Like T2K, the angle was chosen to be off-axis. The ν_μ energies peak at ~ 2 GeV, which is also the peak of the $\nu_\mu \rightarrow \nu_e$ appearance probability; see Figure 1-12. A schematic of the detectors can be seen in Figure 1-13. Both are made of the same material, PVC cells containing a mixture of mineral oil and pseudocumene, and function as tracking calorimeters[50]. The near detector weighs 0.22 kiloton and is 1 km from the graphite target, whereas the far detector is 810 km away, and weighs 14 kilotons. Depending on the values of θ_{13} and δ_{CP} , NO ν A may be able to resolve the neutrino mass hierarchy if the parameters are large. The long baseline implies matter effects, and matter effects depend on the mass hierarchy. The near and far detectors should be ready to take data in fall of 2013 [6].

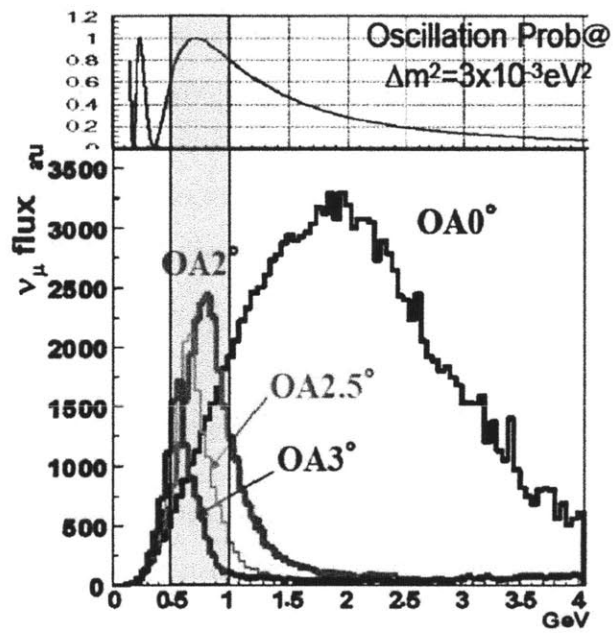


Figure 1-11: The T2K ν_μ beam energy spectra. The $P(\nu_\mu \rightarrow \nu_e)$ probability is superimposed with arbitrary units. The ideal off-axis angle of 2.5° is shown, and is easily seen to be near the maximum of the appearance oscillation probability with a very narrow peak. Figure taken from [5].

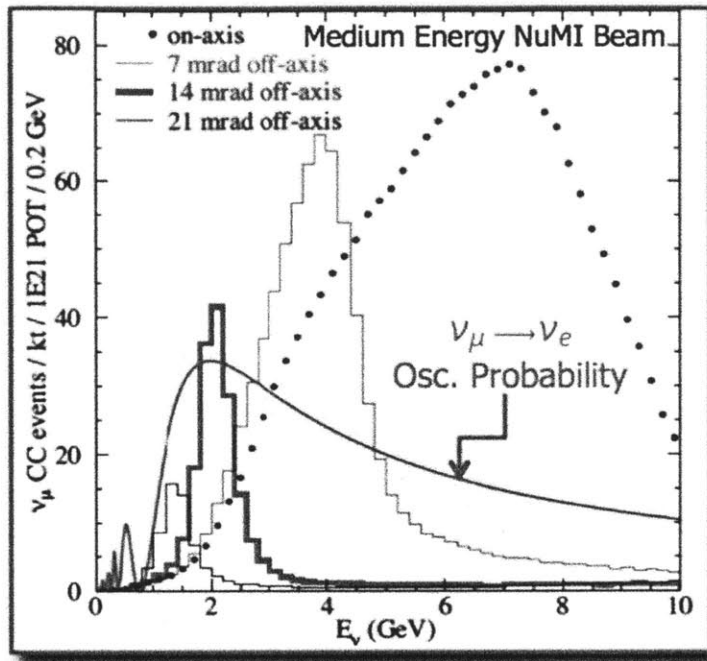


Figure 1-12: The NO ν A ν_μ beam energy spectra. The $P(\nu_\mu \rightarrow \nu_e)$ probability is shown on top. The ideal off-axis angle of 0.8° (14 mrad) is shown in red, and is easily seen to be near the maximum of the appearance oscillation probability with a very narrow peak. Figure taken from [6].

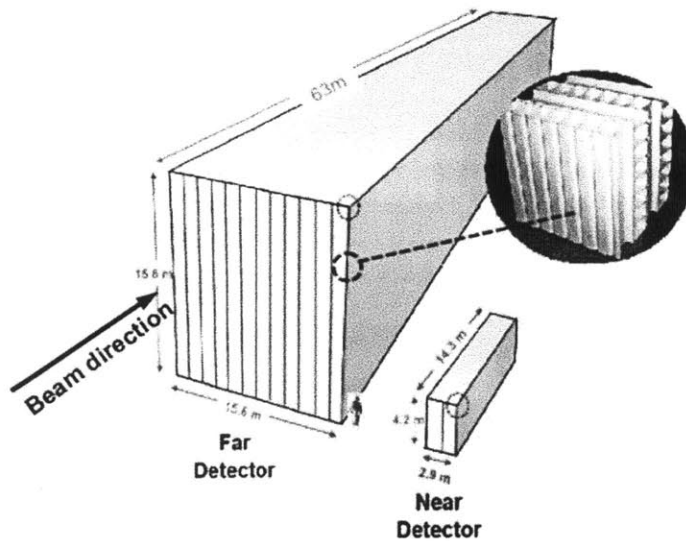


Figure 1-13: The NO ν A detectors.

1.5 The Reactor Antineutrino Anomaly

In order to carry out a disappearance experiment at a reactor, the emitted unoscillated antineutrino flux must be both predicted and measured. Reactors produce antineutrinos through the β decay of the fission products of uranium and plutonium. We can decouple the flux into two components for each fissioning isotope:

$$S_{tot}(E_\nu) = \sum_k f_k S_k(E_\nu). \quad (1.12)$$

Here, k sums over the four fissioning isotopes ^{235}U , ^{238}U , ^{239}Pu , and ^{241}Pu . The f_k represent the fraction of the fissions that are caused by the k th isotope. These are a function of time and of reactor operating parameters, such as the fuel amount and fuel temperature. In fact, calculation of the f_k are a central goal of this thesis, and more details will be found in Chapters 3 through 5. In this section, we focus on the determination and recent re-analysis of the S_k , the reference spectra or the number of emitted antineutrinos per fission as a function of energy.

The reference spectra, $S_k(E_\nu)$ for the four aforementioned isotopes, are extracted from measurements of the β spectra made at the ILL research reactor[56]. By exposing thin foils of uranium and plutonium to the thermal flux of the ILL reactor (the baseline was 80 cm), the β spectrum of ^{235}U , ^{239}Pu , and ^{241}Pu were measured for irradiation times less than 36 hours using a magnetic spectrometer. Because ^{238}U will only fission with neutron energies near 1 MeV, its β spectrum could not be measured and must be calculated from first principles. At the β -branch level, the conversion from β energy to antineutrino energy is simple, neglecting nuclear recoil: $E_\nu = E_0 - E_\beta$, where E_0 is the endpoint of a β branch. The original predictions [57] used a phenomenological model to convert the observed β spectrum from the ILL experiment into an antineutrino energy spectrum. This model used 30 “virtual”, or effective, beta-branches. We now survey the results of the short baseline experiments.

Experiment	Distance [m]	Old	New	Error (%)
ILL	9	0.832	0.788	9.5
Bugey-3	15	0.988	0.930	4.8
Bugey-3	40	0.994	0.936	4.9
Bugey-3	95	0.915	0.861	14.1
Bugey-4	15	0.987	0.926	3.0
Rovno	18	0.969	0.901	6.9
Rovno	18	1.001	0.932	6.9
Rovno	18	1.026	0.955	7.8
Rovno	18	1.013	0.943	7.8
Rovno	18	0.990	0.922	7.2
Goesgen	38	1.018	0.949	6.5
Goesgen	45	1.045	0.975	6.5
Goesgen	65	0.975	0.909	7.6
Krasnoyarsk	33	1.013	0.920	5.8
Krasnoyarsk	92	1.031	0.937	20.3
Krasnoyarsk	57	0.989	0.931	4.9
Savannah River	18	0.987	0.936	3.7
Savannah River	24	1.055	1.001	3.8

Table 1.3: Very short baseline reactor data. The old and new ratios are $N_{measured}/N_{predicted}$, where the predictions contain no oscillation effect [29, 7]

1.5.1 Very Short Baseline Reactor Experiments

In the 1980s and 1990s, several short-baseline reactor experiments took place in order to measure the emitted flux and to search for oscillations. The results are shown in Table 1.3. These experiments are all < 100 m from the reactors. The ILL [56], Bugey-4 [58], Krasnoyarsk [59, 60], Rovno [61] and Goesgen [62] detectors used ^3He and liquid scintillator to search for recoil neutrons produced in inverse β decay, while Bugey-3 [51] used ^6Li . The Savannah River experiments [63, 64] and a later phase of the Rovno experiment [65] used Gd-doped liquid scintillator. With the exception of the ILL experiment, the experimental results were consistent with a no-oscillation prediction.

1.5.2 Reanalysis of Reactor Flux Prediction

In [66, 29, 67], a reanalysis of the predicted S_k was performed. This “*ab initio*” reanalysis used the enormous amount of information that was contained in nuclear databases [68, 31, 69, 70] including thousands of beta-branches to perform a more sophisticated calculation. Where their prediction disagreed with the ILL data, effective β branches were used as a correction. The result of the reanalysis was an overall $\approx 2 - 3\%$ increase in the normalization of the spectra. A similar study using only β branches with endpoint energies from nuclear databases was performed that confirmed this shift[67]. This second work applied a sophisticated treatment of corrections to the theoretical β spectrum, including a detailed treatment of corrections from screening, finite size of the nucleus, and weak magnetism. This increase implies that the ratio of data to prediction then decreases; averaging over all of the very short baseline experiments, the mean ratio shifts from 0.976 ± 0.024 to 0.943 ± 0.023 . The systematic underestimate of this ratio is called the reactor antineutrino anomaly. The current state of the results are shown in Figure 1-14.

After the reanalysis, the predictions are no longer consistent with experiment. It is possible that the lighter neutrinos could be oscillating into a sterile neutrino, explaining the anomaly. However, this is only speculation and will not be considered further in this thesis. Instead, we note the effect of the reanalysis on our knowledge of θ_{13} . The results from CHOOZ and KamLAND were reanalyzed, and with the new prediction, the result yielded a best-fit value of $\sin^2(2\theta_{13}) = 0.13 \pm 0.06$ (1σ error) [29].

Now that our survey of the search for θ_{13} is complete, we turn to a description of the Double Chooz experiment.

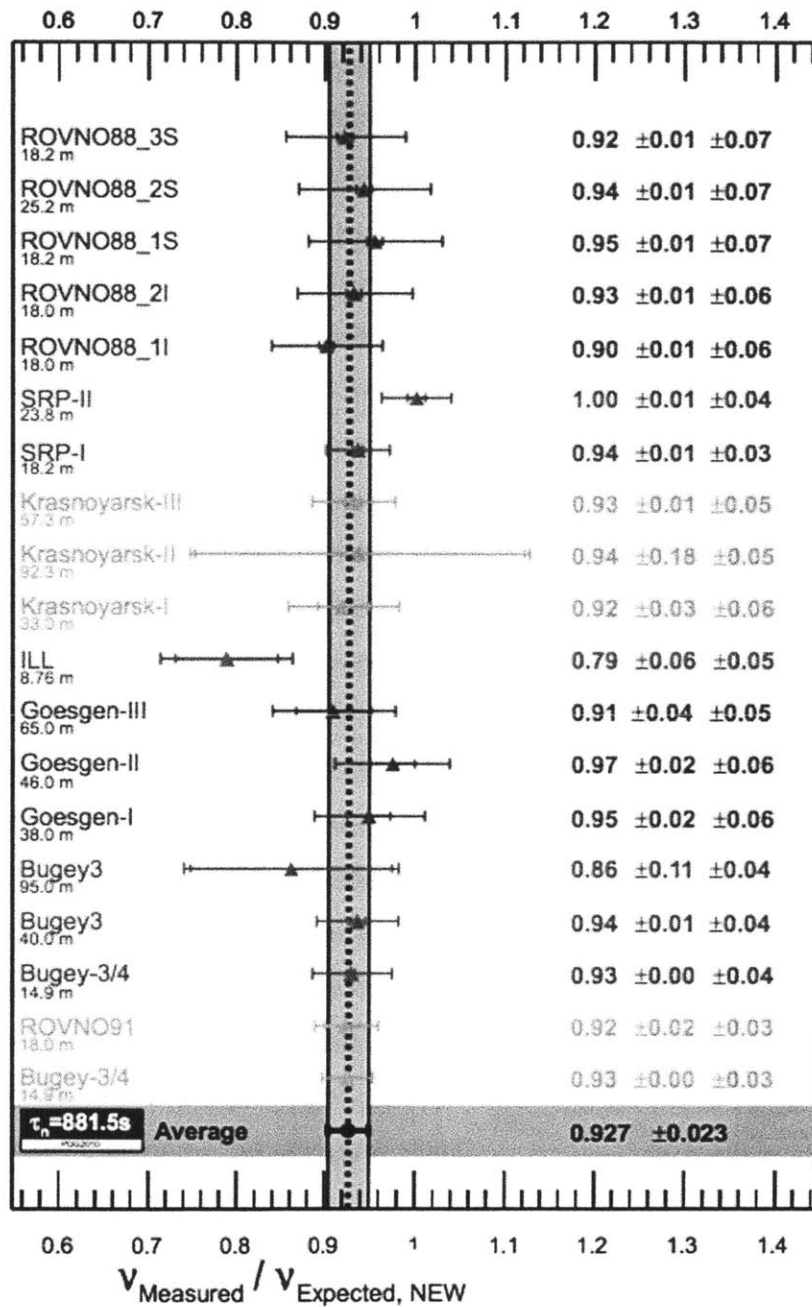


Figure 1-14: The antineutrino anomaly. The data points are the reanalyzed results from the very short baseline reactor flux experiments. Taken from [7].

Chapter 2

The Double Chooz Experiment

The Double Chooz experiment is the successor to the original CHOOZ experiment, and in many ways improves upon the original:

- Where CHOOZ only had a far detector to measure the oscillated antineutrinos, Double Chooz will employ a near as well to measure the unoscillated flux;
- The Double Chooz detectors have improved shielding to reduce backgrounds;
- The PMTs in the Double Chooz detectors are surrounded by a non-scintillating buffer region to reduce the background from the PMTs themselves;
- Double Chooz has a larger target volume;
- Double Chooz will take data for 5 years, much longer than CHOOZ's 15 months.

The total systematic uncertainty from the reactor in the CHOOZ experiment was 2.7%. In 100 days of data taking, Double Chooz has already reduced the upper limit of $\sin^2 2\theta_{13}$, for which CHOOZ could only provide an upper bound of < 0.15 , and the total reactor systematic uncertainty was 1.7%. In this chapter, we describe the detector design and the key features of the analysis software.

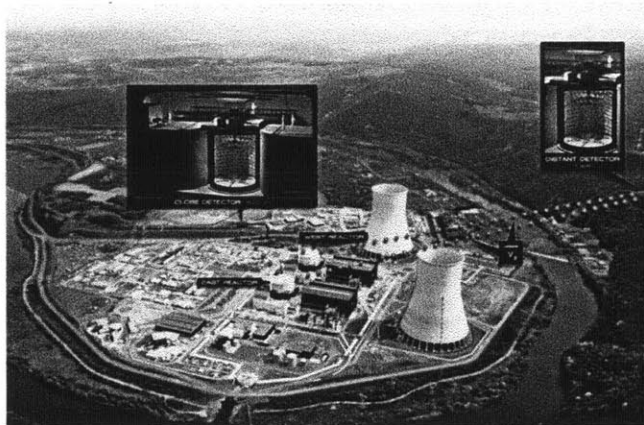


Figure 2-1: Chooz power plant with Double Chooz detectors.

2.1 Location

Per its namesake, the Double Chooz experiment is located in Chooz, France, a village in the northeast that shares a border with Belgium. Chooz is home to a nuclear power plant that consists of two reactor cores, called B1 and B2. The experimental apparatus consists of two identical detectors: the Near Detector, which is being constructed as of fall 2011 and lies approximately 400 meters from the reactor cores, and the Far Detector, which began data taking in April 2011 and is near the oscillation maximum, at approximately 1 kilometer from the cores. The plant can be seen in Figure 2-1. Both detectors are shielded from cosmic ray-induced backgrounds by being underground; the Near Detector is buried to a depth of 120 m.w.e, while the Far Detector is deeper at 300 m.w.e.. The experiment's cost was reduced by placing the Far Detector into the same hall as the CHOOZ experiment, but this limited the size of the detectors.

2.2 The Chooz Reactor Cores

The Chooz reactor cores, B1 and B2, together emit $\sim 10^{21}$ antineutrinos per second as part of normal power generation, and are thus a very low-cost method of obtaining data on neutrino oscillations. What follows is a brief description of the operation of

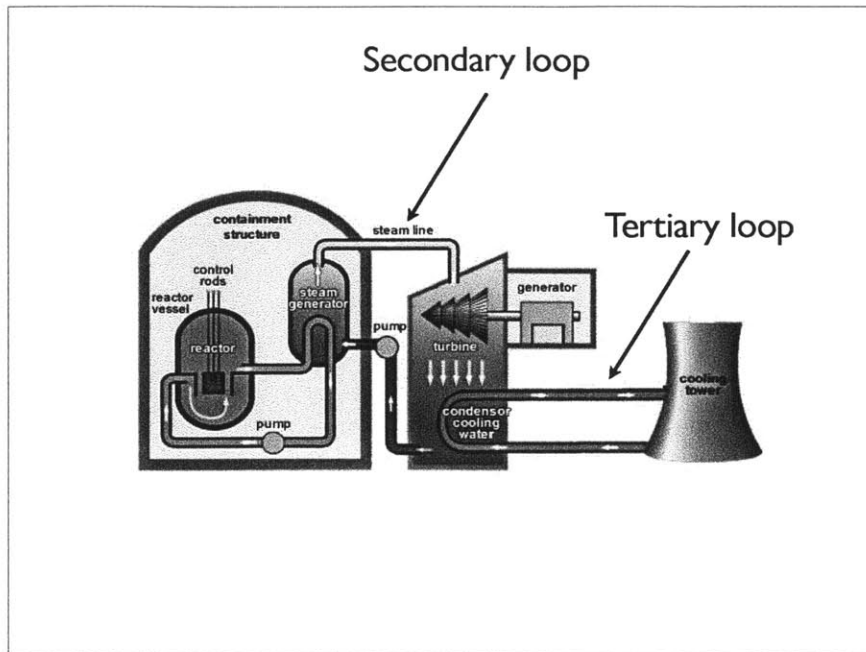


Figure 2-2: Illustration of principal components of a PWR.

the cores.

2.2.1 Reactor Plant Design

The most common reactor design is the pressurized water reactor (PWR). The diagram in Figure 2-2 shows a typical PWR design. As water enters the reactor core via the primary circuit, heat from nuclear fissions of heavy actinides raises the water temperature. This water is kept at pressures exceeding 15 MPa so that it will remain in the liquid state even at high temperatures. Typical temperatures are ~ 575 K. Water from the primary circuit is isolated from water in the secondary steam circuit. Water in the secondary circuit is heated and turned into steam to turn turbines for electrical power. The separation of these two water circuits is desirable since water from the primary loop may become radioactive, and in an emergency situation could become steam if the loops were not separated. This feature thus aids in the prevention of radioactive steam escaping the power plant.

After progressing through the turbines, the steam is condensed in a tertiary loop,

which uses water from the Meuse river for cooling. It is also kept separate from the other two circuits. In this work, we focus only upon the energy generation from the reactor core itself since it is the fissions in the core which generate antineutrinos.

2.2.2 Reactor Core Layout

To describe the reactor core layout, we progress from the smallest units to the largest. For the Chooz cores, the uranium fuel is introduced as cylindrical ceramic pellets, made of uranium dioxide. The pellets have a typical diameter of 1 cm and have a density of about 11 g/cm^3 . The pellets are stacked into a fuel rod, which has a typical length of 4 meters; the rods in the Chooz cores have a length of 4.267 m. The fuel rod is clad in Zircaloy, which is mostly zirconium with trace amounts of chromium, tin, and nickel. Since the neutron flux from fissioning of the fuel can exceed 10^{14} neutrons/cm-s, zirconium is a popular cladding for the fuel rod due to its low neutron absorption cross section.

The pellets and cladding are surrounded by a moderator, which for PWRs is typically normal water. The fuel pellets, cladding, and moderator constitute a square cell, whose side length is typically 1.26 cm. A grid of fuel rods is bundled into a fuel assembly, which is usually referred to by its rectangular dimensions; i.e., a 16×16 assembly contains $16^2 = 256$ cells. Not all of the cells contain fuel rods; other types of cells include the instrumentation cell, which is usually at the center of the assembly and contains a neutron flux detector; and control cells, into which control rods made of boron or cadmium can be inserted to control the fission rate of the fuel. An example fuel assembly is shown in Figure 2-3. Typical uncertainties of the fuel composition is on the order of 5% [71]. The implications of these uncertainties on our fission rate calculations will be explored in Chapter 5. The fuel assemblies in the Chooz reactors are all of the 17×17 type, and are designed by Areva-Framatone. The fuel assembly is the fundamental unit of fuel in typical reactor operations. The assembly is inserted into the core as a whole, irradiated for approximately a year, and then reshuffled in the core in such a way that critical parameters of the reactor core, such as neutron flux and fuel temperature, are kept as uniform as possible.

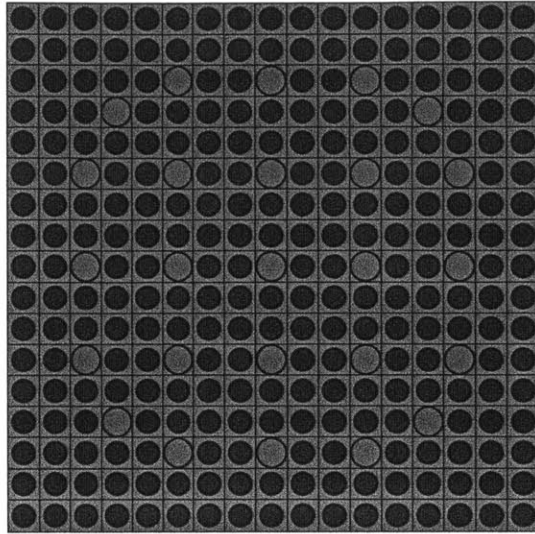


Figure 2-3: Assembly example. This image was made with DRAGON. The color purple refers to fuel, faint green refers to cladding, and grey refers to water.

The reactor core is then a collection of fuel assemblies. A typical core can have 100 to 170 fuel assemblies; the number depends on the application, from nuclear submarine to power plant. B1 and B2 each contain 205 assemblies, one of the largest designs in the world [2], and they each generate 4.25 GW-thermal (GW_{th}) of power. Due to the efficiency of the plant, this amounts to 1.15 GW of available electrical power per core. The core is then surrounded by shielding and a concrete containment structure, whose construction requires a detailed knowledge of thermal hydraulics.

2.2.3 Generation of Antineutrinos in the Core

Out of the hundreds of isotopes generated during nuclear fission, only four are relevant for the generation of antineutrinos: ^{235}U , ^{238}U , ^{239}Pu , and ^{241}Pu . Despite the presence of other fissioning isotopes, such as ^{240}Pu and the fissile ^{233}U , the aforementioned four isotopes account for $> 99.9\%$ of all antineutrinos generated in reactors[72]. The primary fuel is ^{235}U . In reactor fuel, the weight fraction of this isotope is increased, or enriched, from its natural abundance of 0.7% to upwards of 3 or 4%. The Chooz reactor cores have enrichments of 4%, 3.4%, and 1.8%. Figure 2-4 illustrates the key

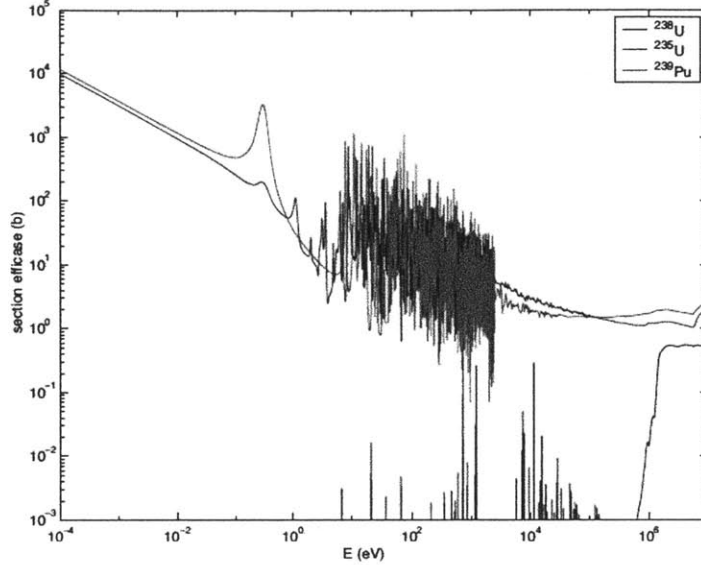


Figure 2-4: Fission cross sections of some radioactive isotopes. ^{235}U and ^{239}Pu have the largest thermal fission cross section of all elements. ^{238}U only fissions with “fast” neutrons, near 1 MeV.

importance of ^{235}U . Note that ^{238}U fissions do not occur below ~ 800 keV. Thus, this isotope is unaffected by thermalized neutrons. ^{235}U will fission on neutrons that are effectively at rest, and at low energies the fission cross section is highest. However, neutrons emitted from a fission of ^{235}U have energies in the MeV range; see Figure 2-5.

Thus it is of crucial importance to reduce the energy of these emitted neutrons so that they can be used to initiate further fission reactions in the fuel. For PWRs, the moderator serves this purpose, and is usually composed of water; in this way, the neutrons lose the most energy per collision and quickly return to thermal energies ($E_n \approx 0.025$ eV). Fissions by thermal neutrons are asymmetric, in that a heavy daughter nucleus ($A \sim 140$) and a light nucleus ($A \sim 70$) are emitted. A typical reaction is



Here the intermediate β -decays have been omitted. On the left side of the reaction, we have 92 protons and 144 neutrons; on the right side, we have 98 protons and 138

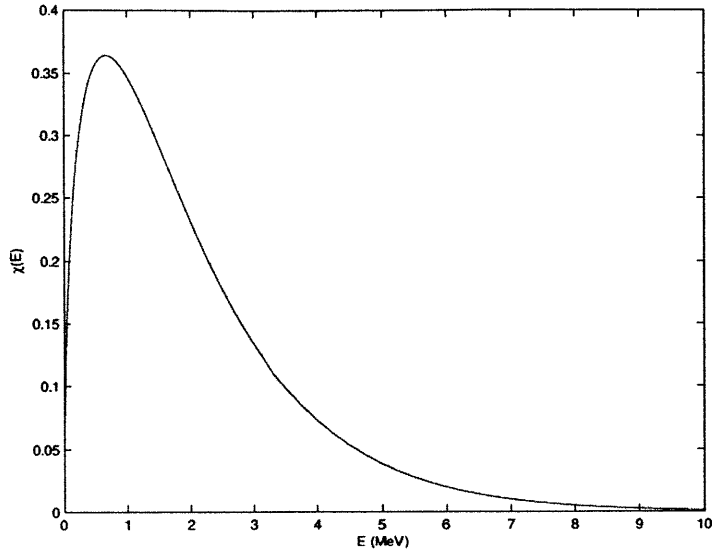
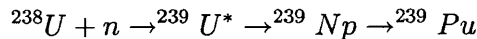
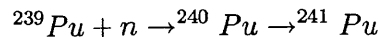


Figure 2-5: Empirical energy spectrum of neutrons emitted in fission reactions, assuming that only ^{235}U fissions. The units are probability per unit energy.

neutrons. Thus we see that there is a deficit of 6 neutrons, which will each β -decay, releasing 6 antineutrinos on average per fission[73]. ^{235}U has the highest fission cross section and is naturally occurring; over the course of a reactor cycle, approximately 55% of the fissions come from this isotope[47]. ^{238}U in contrast only accounts for about 10% of the fissions, and only fissions at energies approaching 1 MeV. However, plutonium, the other fissile isotope, is only produced from fissions of ^{238}U via the following chain reaction:



^{239}Pu accounts for nearly a third of the fissions per cycle. ^{241}Pu , which accounts for approximately 7% of the fissions per cycle, is produced via



These four isotopes are part of the uranium cycle, which is shown in Figure 2-6.

It is now clear that the fission rates of the four aforementioned isotopes are directly

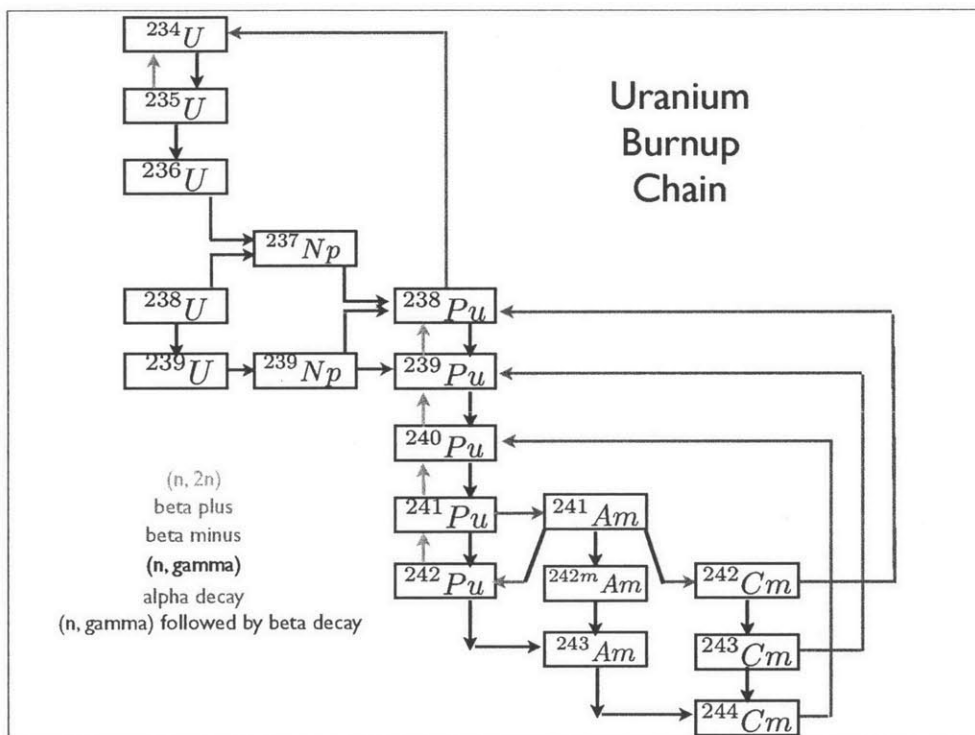


Figure 2-6: Radionuclides involved in the uranium cycle.

correlated with the reactor thermal power: $\sum_k f_k E_k = P_{th}$, where the E_k are the energies released per fission. Thus the precision to which the thermal power is measured is very important. For the Chooz reactors, EDF uses two methods to monitor the power. The first method compares heat exchange between the primary and secondary circuits. It is a very precise measurement, with an uncertainty of 0.46% [74], but is only performed monthly. The second method measures the neutron flux directly via ionization chambers, which happens far more frequently (sometimes by the minute), but is less precise. In fact, the heat exchange method calibrates the neutron flux measurements on a monthly basis.

2.3 Detector Design

We now discuss the design of the Double Chooz detectors, starting with its detection principle, inverse β -decay, and its principal detector components: the inner target, the gamma catcher, the buffer region, and inner and outer veto regions. An illustration of the detector can be found in Figure 2-7.

2.3.1 Detecting Antineutrinos With Inverse β Decay

Reactor antineutrino experiments such as Double Chooz are possible due to the inverse β decay (IBD) reaction:



The neutron produced has energies in the keV range, and so the threshold for this reaction is given by:

$$E_\nu^{min} = \frac{(m_e + M_n)^2 - M_p^2}{2M_p} \approx \Delta + m_e$$

Here, $\Delta = M_n - M_p = 1.293$ MeV. The threshold is at 1.804 MeV. In the two-body interaction where we assume that the nucleus is very massive, the outgoing positron

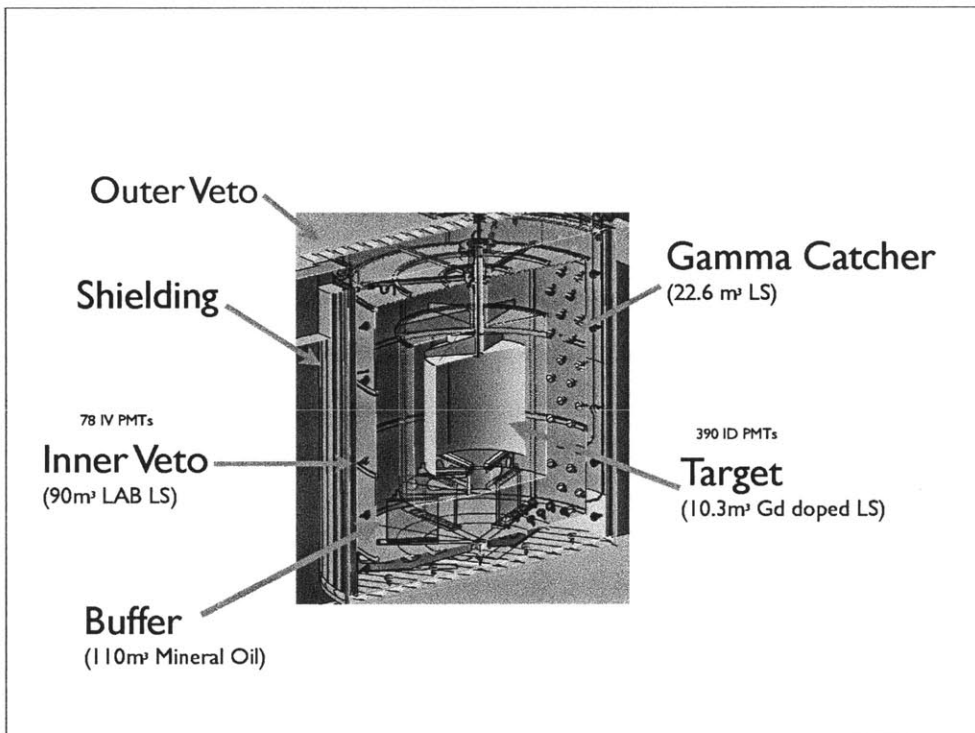


Figure 2-7: Illustration of Double Chooz main detector components.

is related to the antineutrino energy by the formula:

$$E_\nu = E_e + \Delta$$

Thus knowledge of the positron energy leads us to knowledge of the antineutrino energy, and therefore maximizing our detection efficiency of the positrons will dictate the detector design.

Ignoring neutron recoil, and assuming only a Coulombic interaction between the emitted β and the charged nucleus, the zeroth-order cross section for IBD is[75]:

$$\sigma_0(E) = \frac{2\pi^2\hbar^3}{m_e^5 c^7 f \tau_n} p_e E_e$$

Here, f is the neutron phase space factor and τ_n is the neutron lifetime. The value of τ_n used for the Double Chooz experiment comes from the MAMBO-II ultra-cold neutron storage experiment[76]: $\tau_n = 880.7 \pm 1.3 \pm 1.2$ s. However, higher-order corrections on the order of $O(E_\nu/M)$, where M is the nucleon mass, can affect the positron yield on the order of 1%[75]. Taking these corrections into account gives:

$$\sigma(E) = \sigma_0(E)(1 + \delta_{rec}(E) + \delta_{WM}(E) + \delta_{rad}(E))$$

The term δ_{rec} takes into account neutron recoil. At this point, the antineutrino energy and the positron energy are no longer as simply related as shown above (setting $\hbar = c = 1$):

$$E_\nu \approx E_e + \Delta + \frac{1}{M} \left[E_e(E_e + \Delta) + \frac{\Delta^2 - m_e^2}{2} \right]$$

This formula assumes that the emitted positron is forward-peaked and ignores the small angular dependence of the positron distribution. The δ_{WM} term adds effects from weak magnetism, which arise from a difference in the neutron and proton magnetic moment. The δ_{rad} term takes radiative corrections up to $O(\alpha)$ into account. These effects are noticeable; the weak magnetic effects decrease the cross section by 2% for 5 MeV positrons[75]. See also[67] for further discussion of these corrections

and their implications for the antineutrino energy spectra.

2.3.2 The Target Volume

The target is a cylindrical volume composed of acrylic. It has a radius of 1.15 m and a height of 2.46 m, and a thickness of 8 mm. The vessel contains 10 m³ of a liquid scintillator mixture: 80% dodecane and 20% PXE. The wavelength-shifters PPO (7 g/L) and bis-MSB (20 mg/L) have been added to absorb and re-emit the scintillation light into the sensitive region of the photomultiplier tubes (PMTs) that are used to detect the light. 1 g/L of Gd is also added to the mixture to increase the neutron detection efficiency.

The fate of the neutron and positron produced by IBD in the target can now be discussed. The positron, carrying the majority of the incident antineutrino's energy, will ionize the scintillator and eventually come to rest, capturing on an electron and pair annihilating into 2 511-keV photons. These photons in turn cause further scintillation light, which is captured by a set of 390 Hamamatsu PMTs. This event happens immediately after the antineutrino interacts and is called the prompt event. The visible energy E_{vis} can thus be defined as

$$E_{vis} = E_e + m_e = E_\nu + m_e + \Delta$$

If there were no Gd present in the detector, the neutron could be absorbed by hydrogen in the scintillator, which produces a 2.2-MeV photon, which is also in the range of radioactivity background (< 3 MeV). This capture on hydrogen takes approximately 180 μ s to occur. However, the presence of Gd in the scintillator offers improvements in both of these areas:

- Neutron capture on Gd causes a cascade of 3 photons (on average) to be emitted. The sum of their energies is in the range of 6 to 9 MeV, well above background radioactivity,
- The capture on Gd takes place in approximately 30 μ s, allowing stricter cuts to

improve the quality of candidate events, and reduced background contamination in the candidate event sample.

The number of photoelectrons per energy deposited is approximately 215 PE/MeV. We will discuss detector calibration in Chapter 6.

2.3.3 The Gamma Catcher

The gamma catcher is a cylindrical volume that surrounds the target region. Like the target region, it contains liquid scintillator; unlike the target region, it contains no Gd. Its role is to capture escaping gamma rays that leave the target volume. In this way, the gamma catcher serves as an effective fiducial volume of the detector. It can also be used to study the so-called “spill-in spill-out” effect. Since the neutrons produced in IBD events can travel several cm before capture, we can imagine two possibilities for neutrons created in IBD events near the target / gamma catcher boundary:

- The positron from the IBD event is captured in the target, but the neutron reaches the gamma catcher. The ensuing gamma cascade does not register as a candidate event because it does not pass the cascade energy cut of ~ 8 MeV. This is called a spill-out event.
- Conversely, an IBD event could occur in the gamma catcher, but this time the neutron travels inward towards the target and captures there. The gamma cascade is detected and appears to be a candidate in coincidence with the positron annihilation. This is called a spill-in event.

The vessel itself is 12 mm thick, has a volume of 22.6 m³, and is made of the same acrylic as the target region. The scintillator in the gamma catcher must be chemically compatible with that of the surrounding buffer mineral oil. The light yield of the target and gamma catcher have been designed to match. For these constraints, the composition of the gamma catcher is 10% PXE, 30% mineral oil, and 60% dodecane. It also contains PPO and bis-MSB for wavelength shifting.

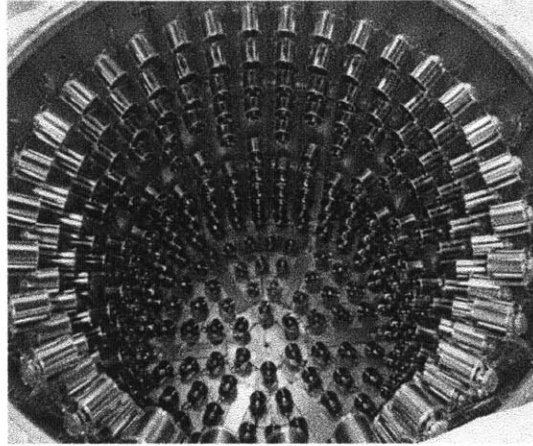


Figure 2-8: The buffer region with PMTs.

2.3.4 The Buffer Region

Surrounding the gamma catcher is the buffer region. This region contains only mineral oil and is thus non-scintillating. It has a volume of 114 m^3 and houses the 390 10-inch Hamamatsu R7081 PMTs. The PMTs are arranged on the top, bottom, and radial wall of the stainless steel region in such a way to have a uniform detector response. The mineral oil is transparent to the photons that must travel from the inner regions to the PMTs through the buffer oil. As mentioned, the mineral oil buffer is one of the chief improvements over the CHOOZ experiment since the PMTs are shielded from their own radioactivity. It also shields against ambient radiation from the surrounding rock. An image of the buffer can be seen in Figure 2-8.

2.3.5 The Inner Veto

The 90 m^3 inner veto (IV) surrounds the inner detector (target, gamma catcher, and buffer) and is optically separated from it. Its purpose is to veto both muons and fast neutrons that enter the detector. To accomplish this, it is filled with liquid scintillator composed roughly half alkanes and half linear alkyl benzene (LAB), containing the same PPO and bis-MSB wavelength shifters as the inner regions. The light in the IV is collected by 78 8-inch PMTs. To increase light collection, the outer wall of the

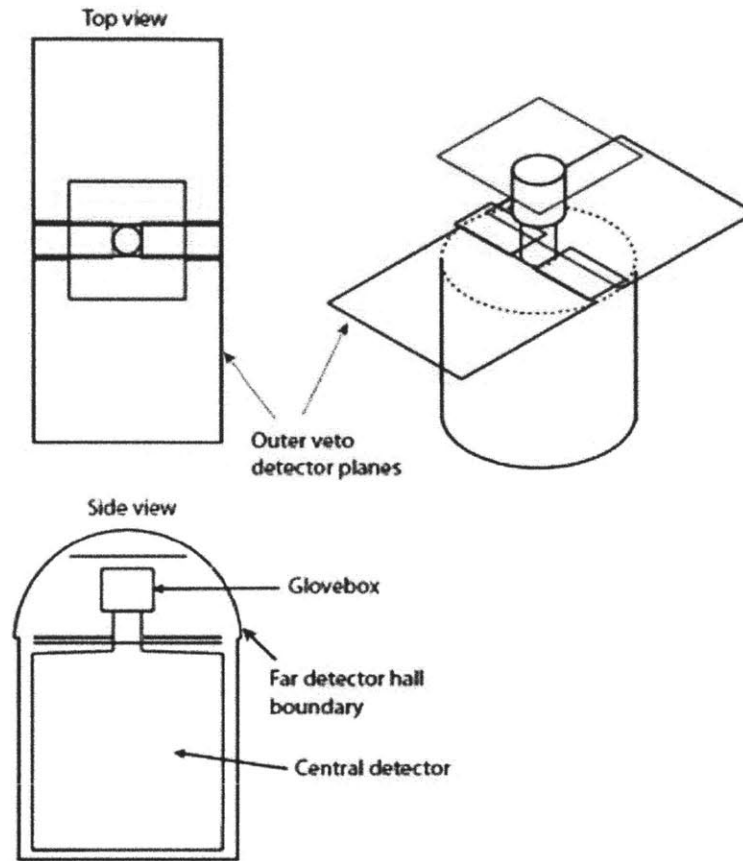


Figure 2-9: Schematic of Outer Veto.

buffer and the inner wall of the IV are covered with reflective foil and paint.

2.3.6 Outer Veto and Shielding

The outer veto (OV) is a muon-tracking system that is installed atop the detector. In order to maximize its coverage area of $6.4 \times 12.8 \text{ m}^2$, its size exceeds the inner detector's cylindrical diameter of 6.5 m; see Figure 2-9. It consists of plastic scintillator strips that are interlaced in the x - and y -directions. Additionally, the detector's large area will allow tracking of muons that graze the detector and subsequently create fast neutrons in the surrounding rock. To shield against radioactivity from the rock, the detector is encased in 15 cm thick demagnetized stainless steel. This is another

improvement over CHOOZ, which only used sand.

2.4 PMT Readout System

An overview of the PMT readout system is shown in Figure 2-10. When light is produced in the inner detector's liquid scintillator, the wavelength shifter in the scintillator shifts the emitted light into the optimal range for the PMTs. Upon reaching the PMTs, the light is converted into an analog pulse. The PMT carries high voltage and signal on one cable, and requires a splitter to separate the HV from the signal. The signal then passes through NIM-based front-end electronics (FEE). Each PMT maps to one channel in the FEE. The FEE amplifies and then sends the signal to a waveform digitizer; this is the meaning of the "1:1" mapping in the figure. The FEE also performs an analog sum of 8 PMT pulses. This sum is reshaped so that the pulse height is proportional to the number of photoelectrons in 8 PMTs[8].

In order to reduce the number of inputs to the trigger, the output pulses of 2 FEE boards are summed, making a sum of 16 pulses, which then passes to the trigger boards. This applies to the inner detector PMTs; there are less inner veto PMTs and so only about 3 to 6 PMTs from that region are connected to the FEE. The Double Chooz FEE are custom-made to match the dynamic range of the two output flash ADCs (FADCs): the μ FADC for muons with a 125 MHz sampling rate and the ν FADC for neutrinos with a 500 MHz sampling rate.

2.5 The Double Chooz Trigger

The inner detector PMTs are partitioned into two trigger groups, A and B. They are distributed uniformly throughout the inner detector, with a Group-A PMT surrounded by Group-B PMTs and vice versa. Half of the PMTs belong to Group A and the other to Group B. This grouping adds redundancy to the measurement since they are observing the same volume [8]. Each group is then fed into its own trigger board; the inner veto PMTs are fed into a veto board. If the summed signals going into

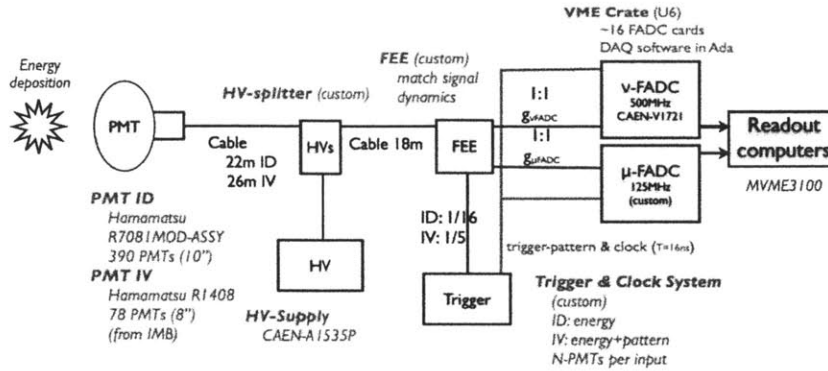


Figure 2-10: Schematic of Double Chooz hardware systems from [8].

any of the boards exceeds a set energy threshold, the FADCs read out the detector. Each trigger reads out 256 ns of both the inner detector and inner veto. The far detector trigger rate is 120 Hz, which allows a low inner detector energy threshold of 350 keV, well below the minimum positron energy[77]. This makes the detector extremely efficient for positron detection.

The trigger board can discriminate between four classes of events: Very High Energy, which are events over 50 MeV and are most likely muons; High Energy, which are between 5 and 50 MeV and are fast neutron-like events; Low Energy events between 0.5 and 5 MeV and are considered positron-like, and Very Low, which are less than 0.5 MeV and used to monitor the low-energy trigger efficiency.

2.6 Calibration

The experiment requires that the relative detection efficiency be 0.5% between the Near and Far Detectors, with an absolute efficiency of 1.5%[47]. Thus it is very important to understand the detector response and triggering efficiencies for the various particles interacting within it. By introducing sources with known energies at known locations, we can obtain energy and position calibration for the experiment. There are two classes of calibration types:

- Intrinsic calibration sources. These include products from cosmic rays, such as

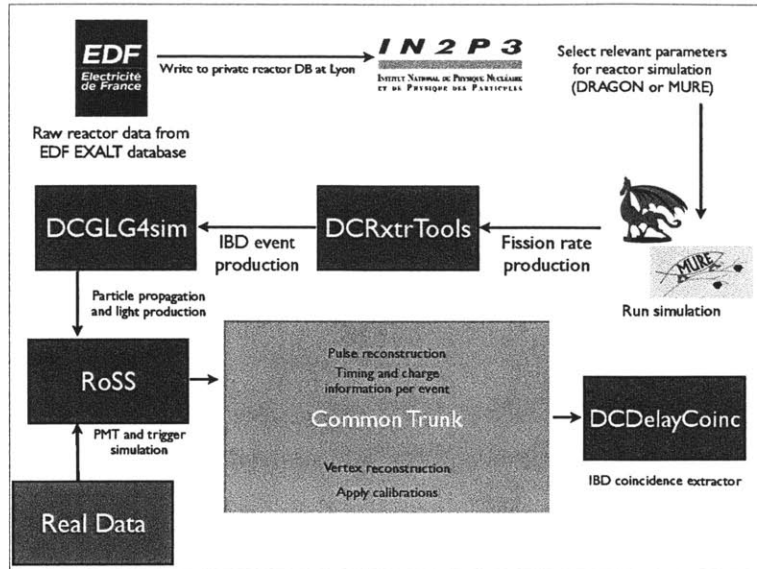


Figure 2-11: Double Chooz software components.

Michel electrons, spallation neutrons, and ^{12}B , a β -emitter.

- Deliberately-introduced sources. This includes gamma, beta, and neutron sources. They can be introduced into the detector via the radiopure “glovebox” above the Outer Veto. The buffer and gamma catcher both have regions into which the sources can be inserted, called the “buffer tube” and “guide tube”. Sources are lowered into these regions through a chimney in the target region. We also employ light injection systems. These are LEDs attached to the buffer wall next to certain PMTs. The LEDs pulses allow us to excite the liquid scintillator and extract important properties, such as the speed of light or attenuation length.

2.7 The Double Chooz Software

The Double Chooz software suite is called DOGS (Double Chooz Offline Group Software) and consists of a collection of software designed for storing, simulating, and analyzing data for the experiment. The schema for the software stack is shown in Figure 2-11. Each stage in the image covers the aspect of the detector that we wish

to understand through simulations:

- **Raw reactor data.** EDF reports over 3000 variables for each reactor and stores them in a private database called EXALT. As the database is updated, authorized members of the Double Chooz Reactor Group can perform a retrieval. EXALT stores information on Excel spreadsheets. These are transformed into MySQL databases, and several QA checks are performed to ensure continuity of the data. The Reactor Group then stores the contents on a private IN2P3 collaboration database. The collaboration database contains data at a granularity of one minute and includes information such as the thermal power, the boron concentration, and the positions of the control rods in the reactor.
- **Reactor simulations.** Double Chooz uses two reactor codes for simulations: DRAGON[78] and MURE[79]. MURE, a Monte Carlo code based off of MCNP, provides the reactor fission rates as a function of time. These fission rates are crucial ingredients to compute the unoscillated antineutrino flux. DRAGON, a deterministic lattice code, computes assembly-level fission rates much more quickly than MURE and is used as a cross-check to the MURE simulations.
- **IBD event generation.** The DCRxtrTools package, which takes the place of DCNuGen, reads fission rate information from the private collaboration database and generates IBD neutron/positron pairs, including their energies, momenta, and positions. It provides a connection between the reactor simulations and the detector database.
- **Scintillation light simulation.** This is carried out by the DCGLG4sim package, which adapts the GLG4sim package[80]. GLG4sim, or “GenericLAND Geant 4 simulation”, was derived from the KamLAND experiment. The package takes IBD candidate events and simulates the light production in the liquid scintillator. The output consists of photoelectrons produced by PMTs.
- **Readout simulation.** The RoSS (Read-out Simulation Software) package simulates PMT output, and creates FADC and trigger output in the same

format as real data.

- **Event reconstruction and calibrations.** The Common Trunk contains several modules that perform pulse reconstruction and calibration, event reconstruction, and quality control.

This thesis focuses on raw reactor data and reactor simulations.

Chapter 3

Simulation of Nuclear Fission Reactors with DRAGON

Lattice calculation theory is peculiar to the field of reactor physics in the sense that most of the useful information is confidential and that the codes themselves are commercial products.

–Alain Hebert, *Applied Reactor Physics* [81]

3.1 The Neutron Transport Equation and its Deterministic Solution

We now turn to the neutron transport equation, the cornerstone of nuclear reactor analysis. All reactor simulation codes, whether they are employed for safety and criticality studies, production of weapons, or fundamental science, must in some way solve this equation. Indeed, the proliferation of codes in industry and academia reflects the myriad approximations and calculational schemes used in the solution of the transport equation. This solution yields the neutron flux, which is a distribution containing the most useful information about the behavior (i.e., location and velocity) of the neutrons in the reactor. Understanding the neutron behavior in a reactor will of course allow us to understand the fission processes that consume and produce them,

which will ultimately inform us about rates of antineutrino production.

Due to the unavailability of high-speed computing, the first generation of simulation codes were required to simplify the transport equation even further, treating neutron transport as a diffusion process with Fick’s law behavior, that is, to linearize the neutron transport equation. That this model is inadequate is explained by noting that while diffusion is characterized by rapid, short-ranged collisions, the neutron-nuclear cross section is on the order of 1 barn, which implies that, compared to diffusive interactions, collisions are much more rare, and the neutron mean free path is $O(1 \text{ cm})$ [82]. This also happens to be the characteristic length of elements in a reactor; a typical PWR fuel rod has a radius of about 4 mm. Also, near the boundary of the reactor core or fuel assembly, or near a strongly-absorbing fuel rod, the diffusion model requires significant, sometimes ad hoc, modification. Instead of working from diffusion “up” to transport, we will follow Duderstadt and choose to start from transport and work “down” to various valid approximations [82]. Indeed, this method justifies the success of the previous generations of reactor codes in their regimes of application, and this allows us to exploit those successes in increasing the speed of our codes.

3.1.1 Derivation

The following derivation follows the developments from [81] and [82]. In the derivation of the neutron transport equation, we only need to appeal to the conservation of (neutron) mass passing through an arbitrary volume in the reactor. In what follows, we will ignore neutron-neutron interactions. We will see that this leads to a linear partial differential equation, as opposed to its more general nonlinear form. This will greatly facilitate the solution. To begin, we take an arbitrary differential volume in a 6-dimensional space (3 dimensions for position, 3 for velocity) and examine the neutrons passing through it. Let $n(\vec{r}, V, \vec{\Omega}, t)$ be the number density of the neutrons pointing in direction $\vec{\Omega}$ (which is a unit vector), moving with speed V , at position \vec{r} , at time t . Thus n is a distribution with respect to all variables. We see that the

number of neutrons at time t is given by

$$n(\vec{r}, V, \vec{\Omega}, t) d^2\Omega dV d^3r \quad (3.1)$$

We can express the number of neutrons passing through the surface of our differential volume in a time Δt by

$$X_1 = \int d\vec{S} \cdot \vec{V} n(\vec{r}, V, \vec{\Omega}, t) dV d^3r \Delta t = \int d\vec{S} \cdot \vec{\Omega} n(\vec{r}, V, \vec{\Omega}, t) V dV d^3r \Delta t \quad (3.2)$$

Using Gauss's divergence theorem, we can rewrite the latter expression as

$$X_1 = \int d^3\Omega \nabla \cdot \Omega n(\vec{r}, V, \vec{\Omega}, t) dV d^3r \Delta t \quad (3.3)$$

We introduce the *macroscopic cross section* Σ as the product of the ordinary microscopic cross section σ with the number density of the interacting material. Thus it has the units of number per inverse meters. Now, if we would like to express the number of collisions moving neutrons out of our phase space in Δt , we can write

$$X_2 = \int \Sigma(\vec{r}, V) n(\vec{r}, V, \vec{\Omega}, t) d^2\Omega d^3r dV d^3r \Delta t \quad (3.4)$$

Neutrons can move into our phase space volume in two ways: they can be scattered into it, moving from original speed V' to speed V , or they can be created in the volume by a fission process. We represent a general source density by Q , and so the number of neutrons passing into the volume is given by:

$$X_3 = Q(\vec{r}, V, \vec{\Omega}, t) d^2\Omega dV d^3r \Delta t \quad (3.5)$$

In general, we can express the rate of change of particles in the volume by

$$X = \int \left(n(\vec{r}, V, \vec{\Omega}, t + \delta t) - n(\vec{r}, V, \vec{\Omega}, t) \right) d^2\Omega d^3r dV d^3r \quad (3.6)$$

$$\approx \frac{\partial n(\vec{r}, V, \vec{\Omega}, t)}{\partial t} \Delta t d^2\Omega d^3r \quad (3.7)$$

This is true to first order in Δt . Finally, we can combine all of these sources and sinks, appealing to the conservation of mass:

$$X = -X_1 - X_2 + X_3 \quad (3.8)$$

Since we are integrating over the same arbitrary volume on both sides of an equation, the integrands must be equal, so we can rewrite the above as

$$\frac{\partial n(\vec{r}, V, \vec{\Omega}, t)}{\partial t} = -\nabla \cdot \Omega n(\vec{r}, V, \vec{\Omega}, t) - \Sigma(\vec{r}, V) n(\vec{r}, V, \vec{\Omega}, t) + Q(\vec{r}, V, \vec{\Omega}, t) \quad (3.9)$$

Since Ω is a unit vector, we see that $\nabla(\Omega F(\vec{r})) = \Omega \cdot \nabla F(\vec{r})$, and we can rewrite the X_1 in terms of a gradient on n .

$$\frac{\partial n(\vec{r}, V, \vec{\Omega}, t)}{\partial t} + \Omega \cdot \nabla n(\vec{r}, V, \vec{\Omega}, t) + \Sigma(\vec{r}, V) n(\vec{r}, V, \vec{\Omega}, t) = Q(\vec{r}, V, \vec{\Omega}, t) \quad (3.10)$$

Now we formally introduce the neutron flux $\phi(\vec{r}, V, \Omega, t) \equiv n(\vec{r}, V, \Omega, t)V$ and rewrite the transport equation:

$$\frac{1}{V} \frac{\partial \phi(\vec{r}, V, \vec{\Omega}, t)}{\partial t} + \Omega \cdot \nabla \phi(\vec{r}, V, \vec{\Omega}, t) + \Sigma(\vec{r}, V) \phi(\vec{r}, V, \vec{\Omega}, t) = Q(\vec{r}, V, \vec{\Omega}, t) \quad (3.11)$$

This is the neutron transport equation. In time-independent situations, the steady-state equation becomes:

$$\Omega \cdot \nabla \phi(\vec{r}, E, \vec{\Omega}, t) + \Sigma(\vec{r}, E) \phi(\vec{r}, E, \vec{\Omega}, t) = Q(\vec{r}, E, \vec{\Omega}, t) \quad (3.12)$$

This occurs during the running of a stable, critical reactor. Here, we have rewritten the speed V in terms of the neutron energy E . The solution to a partial differential equation is not complete until we have specified the boundary conditions. Here we briefly summarize a few classes of conditions. Let \vec{S} be the outward normal to the boundary of the system:

- Albedo condition: $\phi_{incoming}(\Omega) = \beta \phi_{outgoing}(\Omega')$, with $\Omega \cdot \vec{S} < 0$. The factor β

is referred to as the albedo. $\beta = 1$ corresponds to *reflective* conditions. The simulations in this work employ reflective conditions because the fuel assemblies under investigation are all surrounded by a water bath, which tends to reflect outgoing neutrons back into the assembly.

- Specular reflection: $\Omega \cdot \vec{S} = -\Omega' \cdot \vec{S}$
- White condition: all particles striking the boundary are re-emitted back into the volume with an isotropic angular distribution.

3.1.2 The Source Density

So far, we have not elaborated on the nature of the source density Q . We will confine our attention here to the stationary (time-independent) case. Q can be decomposed into two components:

$$Q(\vec{r}, E, \Omega) = \int d^2\Omega \int_0^\infty dE' \Sigma_s(\vec{r}, E \leftarrow E', \Omega \cdot \Omega') \phi(\vec{r}, E', \Omega') + \frac{Q_f(\vec{r}, E)}{4\pi K_{eff}} \quad (3.13)$$

Here we have introduced the notation $\Sigma_s(\vec{r}, E \leftarrow E', \Omega \cdot \Omega')$, which represents the macroscopic scattering cross section, which in turn depicts neutrons originally with energy E' finally obtaining energy E . This quantity is in fact a double differential cross section, but this notation makes the transition of the states more clear. A crucial quantity in the stability of a reactor is K_{eff} , the effective multiplication factor. To understand its importance, recall that we are examining the steady-state transport equation. Thus, we must ensure that neutron leakage and source contributions are continually balanced. We can then imagine that K_{eff} serves the purpose to rescale the fission source Q_f to maintain stationary balance. At any particular equilibrium state, this rescaling will be the ratio of the neutrons produced in the current state to those produced in the previous state:

$$K_{eff} \equiv \frac{\text{Neutrons produced in this state}}{\text{Neutrons produced in previous state}} \quad (3.14)$$

It is clear that if the number of neutrons produced in the present state equals the number of neutrons produced from the previous state, then $K_{eff} = 1$. This is the definition of *criticality*. Likewise, a *supercritical* reactor has $K_{eff} > 1$, and a *subcritical* reactor has $K_{eff} < 1$. During typical reactor operation, K_{eff} begins slightly larger than 1 and ends less than 1 by the end of the running cycle due to depletion of ^{235}U . We can further decompose the fission source term:

$$Q_f(\vec{r}, E) = \sum_i \chi_i(E) \int_0^\infty dE' y \Sigma_{f,i}(\vec{r}, E) \phi(\vec{r}, E') \quad (3.15)$$

Here, y is the number of neutrons emitted per fission, and $\Sigma_{f,i}$ is the fission cross section of the i th fissile isotope. Finally, $\chi_i(E)$ is a spectrum giving the probability density in energy of neutrons emitted from fissions of the i th isotope. As for the scattering term, we can perform a decomposition into spherical harmonics Y_{lm} in terms of the direction Ω . The full expression for the source term is thus:

$$Q(\vec{r}, E, \Omega) = \int_0^\infty \sum_{l=0}^L \frac{2l+1}{4\pi} \Sigma_{s,l}(\vec{r}, E \leftarrow E') \sum_{m=-l}^l R_{lm}(\Omega) \phi_{lm}(\vec{r}, E') \quad (3.16)$$

$$+ \frac{1}{4\pi K_{eff}} \sum_i \chi_i(E) \int_0^\infty dE' y \Sigma_{f,i}(\vec{r}, E) \phi(\vec{r}, E') \quad (3.17)$$

Here, $\Sigma_{s,l}$ is the l th Legendre coefficient of the scattering cross section, $\phi_{lm}(\vec{r}, E) \equiv \int d^2\Omega Y_{lm}(\Omega) \phi(\vec{r}, E, \Omega)$, and $\phi(\vec{r}, E) \equiv \frac{1}{4\pi} \int d^2\Omega Y_{lm}(\Omega) \phi(\vec{r}, E, \Omega)$. The utility of these derivations is apparent if we substitute this form for Q into the neutron transport equation. It thus becomes an eigenvalue problem, with K_{eff} as eigenvalue and the flux as eigenvector. Only the fundamental eigenvector is positive for all energies, and so only its value for K_{eff} has physical meaning. This eigenvalue method is employed in DRAGON to solve for K_{eff} . Also, since multiplying an eigenvector by any scalar yields another eigenvector, the normalization constant is arbitrary. In DRAGON it will be defined via power normalization, wherein the total thermal power output is rescaled by the integral of the flux.

Despite the simplifications we have performed, it is extremely difficult to solve

this equation with its attendant boundary conditions in closed-form except for the simplest and artificial cases. Approaches to making the solution more tractable fall broadly into two categories: Monte Carlo and deterministic schemes. The accuracy of Monte Carlo methods is limited only by computing power and computing time, which is simultaneously an advantage and disadvantage. Despite the more accurate solution of the neutron flux with this method, the solutions can take considerably longer to obtain. Monte Carlo codes, such as MCNP and TRIPOLI, have been industry standards for decades and as such are very useful in the validation of deterministic codes. In this work, we will employ only DRAGON, a deterministic code due to its open-source nature and high-speed results. We now turn to DRAGON’s computational strategy: the multigroup method.

3.1.3 Multigroup Discretization

The neutron flux only weakly depends on the azimuthal angle for thermal reactors like PWRs. This is seen when considering that only the $l = 0$ and $l = 1$ spherical harmonics are necessary to retain in such an expansion. However, for PWRs, the very large spatial heterogeneity requires a very detailed spatial discretization for accurate results. When we discuss the collision probability method below, we will see how this process, called homogenization, can be accomplished. Nearly as important is the energy discretization since the energies of neutrons in a reactor range from thermal energies ($\approx 10^{-3}$ eV) to nearly 10 MeV. Our simulations must be able to compute reaction rates, such as fission rates, at arbitrary energies in this range.

The multigroup method consists of dividing this range into energy groups. Within each group, the neutron energies are taken to be constant. This is the one-speed approximation. These one-speed models are only valid far from abrupt changes in media, such as that seen between fuel pellets and cladding. The general strategy in this approximation is to ensure that, regardless of what type of averaging is performed in the one-speed region, the more simply averaged, or “homogenized”, reaction rates are required to be equal to what would have been obtained had the more detailed calculation been performed.

The partition and averaging of the flux and cross section energies is sometimes called condensation. For a typical PWR at the pin level, one can perform spatial weighting by volume, and partition the energies into G groups, where G can be anywhere from about 70 to over 400. Typically, after this first partitioning the simulation code will perform another condensation into a much smaller number of groups: $G < 10$. Another very important factor that must go into the condensation procedure is assurance that low-energy resonances of crucial fissile isotopes are taken into account. Examples of this are the 0.3 eV resonance of ^{239}Pu and the 6.6 eV resonance of ^{238}U . The analysis of the number and width of these groups that is optimal for reactor calculations is as much art as it is science. After the energy discretization, the single transport equation is replaced with G coupled equations, which will be used in the next section:

$$\Omega \cdot \nabla \phi_g(\vec{r}, E, \vec{\Omega}, t) + \Sigma_g \vec{r}, E \phi(\vec{r}, E, \vec{\Omega}, t) = Q_g(\vec{r}, E, \vec{\Omega}, t) \quad (3.18)$$

Here g ranges from 1 to G .

3.1.4 Solution of the Transport Equation

Now that we have introduced the multigroup linearized transport equation, we must describe the algorithms for its solution. There is a wide variety of options to effect a solution. Some of the more popular methods include the collision probability[78] method, solution via discrete ordinates, and the method of characteristics. The collision probability (CP) method has been employed in several industry-standard simulation codes, including APOLLO2[83] and DRAGON[78]. A particularly useful feature of DRAGON is its modular nature; it allows the user to effect a simulation while only changing the solution algorithm. However, in this work only the CP method is employed. Before we can discuss the CP method, we must first convert the transport equation into a suitable form: the integral form.

3.1.4.1 Characteristic and Integral Form of the Transport Equation

Let us examine the multigroup differential transport equation, ignoring the transport correction. Physically, we can imagine that a neutron, born of source Q_g , will propagate through a medium characterized by the macroscopic cross section Σ_g with a flux ϕ_g . This propagation has an exponential attenuation, as the probability of neutron interaction depends very much on its medium. The attenuation is much like that of photons in matter, hence the term “optical path.” Since we have integrated to infinity, this implies that we are in the lattice scenario, or “infinite domain” case. This is the scenario in which all of our simulations will take place.

$$\Omega \cdot \nabla \phi_g(\vec{r}, \vec{\Omega}) + \bar{\Sigma}_g(\vec{r}) \phi_g(\vec{r}, \vec{\Omega}) = Q_g(\vec{r}, \vec{\Omega}) \quad (3.19)$$

The differential operator in the first term in this equation is known as the *streaming operator*. In order to perform the integration, we introduce the concept of the *characteristic*, which is the fixed-direction trajectory of the neutron. The direction is specified by solid angle $\vec{\Omega}$. The advantage gained is similar to that of characteristic curves in the general solution of partial differential equations: we can characterize the path of the neutron by a single parameter s , so that at $t = 0$ if the neutron is located at position \vec{r} , it will be found at position $\vec{r} + s\vec{\Omega}$ at time $t + s/V$, where V is the speed of the neutron. With this definition, we can recast the streaming operator in terms of a differential on the characteristic:

$$\frac{d}{ds} = \Omega \cdot \nabla + \frac{1}{V} \frac{\partial}{\partial t} = \Omega \cdot \nabla \quad (3.20)$$

since the equation is time-independent. Thus, the *characteristic form of the transport equation* can be written as

$$-\frac{d}{ds} \phi_g(\vec{r} - s\vec{\Omega}, \vec{\Omega}) + \bar{\Sigma}_g(\vec{r} - s\vec{\Omega}) \phi_g(\vec{r} - s\vec{\Omega}, \vec{\Omega}) = Q_g(\vec{r} - s\vec{\Omega}, \vec{\Omega}) \quad (3.21)$$

Here we have replaced s by $-s$ to obtain the so-called *forward* characteristic form. This is analogous to the retarded solutions to the wave equation, which allow us to

predict future positions of the neutron from previous positions. Now we are in a position to integrate the transport equation. To this end, we introduce the *optical path* for the g th energy group, $\tau_g(s)$:

$$\tau_g(s) = \int_0^s dx \bar{\Sigma}_g(\vec{r} - x\vec{\Omega}) \quad (3.22)$$

From the general theory of first-order differential equations, we can use an integrating factor, $e^{-\tau_g(s)}$:

$$-\frac{d}{ds} \left[e^{-\tau_g(s)} \phi_g(\vec{r} - x\vec{\Omega}, \vec{\Omega}) \right] = e^{-\tau_g(s)} Q_g(\vec{r} - x\vec{\Omega}, \vec{\Omega}) \quad (3.23)$$

Now we can integrate from 0 to ∞ and obtain finally:

$$\phi_g(\vec{r}, \vec{\Omega}) = \int_0^\infty ds e^{-\tau_g(s)} Q_g(\vec{r} - s\vec{\Omega}, \vec{\Omega}) \quad (3.24)$$

This is the integral form of the transport equation. We can now tackle the problem of solving the integral equation via the CP method.

3.1.4.2 Solution *via* the Collision Probability Method

We have already discretized the transport equation in terms of energy to obtain the multigroup equations. We now perform a spatial discretization within each energy group. This partitioning, along with the assumption of a uniform flux within each partition, will lead us to a solution method. We begin by integrating the g th flux over the solid angles, and assuming that the neutron source is isotropic:

$$\phi_g(\vec{r}) = \frac{1}{4\pi} \int d^2\Omega \int_0^\infty ds e^{-\tau_g(s)} Q_g(\vec{r} - s\vec{\Omega}) \quad (3.25)$$

Let $\vec{x} \equiv \vec{r} - s\vec{\Omega}$. Then, $d^3x = x^2 dx d^2\Omega$, and we can write:

$$\phi_g(\vec{r}) = \int d^3x \frac{e^{-\tau_g(s)} Q_g(\vec{x})}{4\pi s^2} \quad (3.26)$$

Let the region under consideration (i.e., a fuel cell) be divided into N subregions. We would like to obtain subregion-averaged quantities of the cross section, so we now multiply the above by the cross section and integrate over each subregion:

$$\int_j d^3r \Sigma_g(\vec{r}) Q_g(\vec{r}) = \int_j d^3r \Sigma_g(\vec{r}) \sum_i Q_{i,g} \int_i d^3x \frac{e^{-\tau_g(s)}}{4\pi s^2} \quad (3.27)$$

Here we can see the influence of subregion j on the other regions in the lattice, represented by the sum over i . We can now introduce some notation:

$$\phi_{j,g} = \frac{1}{v_j} \int_j d^3r \phi_g(\vec{r}) \quad (3.28)$$

$$\Sigma_{j,g} = \frac{1}{v_j \phi_{j,g}} \int_j d^3r \Sigma(\vec{r}) \phi_g(\vec{r}) \quad (3.29)$$

$$P_{ij,g} = \frac{1}{v_i} \int_i d^3x \int_j d^3y \Sigma_g(\vec{r}) \frac{e^{-\tau(s)}}{s^2} \quad (3.30)$$

Here, $s = |x - y|$. With these, we can rewrite our cross section weighted flux as

$$v_j \Sigma_{j,g} \phi_{j,g} = \sum_i Q_{i,g} v_i P_{ij,g} \quad (3.31)$$

The first two newly defined quantities are the flux and cross section in subregion j and in energy group g . The third quantity is the *collision probability*, which is defined as the probability for a neutron born in any subregion i to have its first collision in subregion j . If we further assume that the cross sections are constant in each subregion, then we may define the reduced collision probability as $p_{ij,g} \equiv P_{ij,g}/\Sigma_{j,g}$.

In the kernel of this solution, we can see that the optical path is symmetric with respect to direction; that is, a neutron is just as likely propagate from i to j as it is from j to i when born of an isotropic source. Thus the $p_{ij,g}$ satisfy the following

reciprocity relation:

$$p_{ij,g}v_i = p_{ji,g}v_j \quad (3.32)$$

Using this, we can finally arrive at the solution:

$$\phi_{i,g} = \sum_j Q_{j,g} p_{ij,g} \quad (3.33)$$

To calculate the CPs in practice, one creates a certain number of neutron trajectories. These can be specified by assigning an integration line density to the calculation, which defines the number of lines per centimeter. These trajectories, along with cross section information about the traversed medium, are required to calculate the optical path, and thus the CPs. Once the CPs are known, they can be combined with the source information to obtain the flux as stated above.

3.2 The Lattice Code DRAGON

The DRAGON simulation code[78] is an open-source deterministic lattice reactor lattice code. It was developed at Polytechnique Montréal during the 1990s and is a descendant of the WIMS-style simulation codes developed at Winfrith and Chalk River National Laboratories[81]. In this section, we outline the features of lattice codes that are relevant to fission rate predictions. A tutorial for DRAGON appears in Appendix A.

3.2.1 Motivating Lattice Calculations

In general, the goal of a lattice code is to predict the neutron flux of a reactor element, which for our purposes can be a fuel rod or a fuel assembly. The term “lattice” comes from the fact that the code assumes that the element in question does not differ drastically from its neighboring components. Thus, the element under study can be assumed to form an infinite lattice of these elements. A simple calculation

will motivate the utility of a lattice code [84]. Consider the general problem of computing the neutron flux throughout a core. At the fuel rod level, to calculate isotopic evolution properly requires that it be subdivided into about 10 radial regions.

In turn, a typical fuel assembly contains about 200 fuel rods, and a reactor core contains about 200 fuel assemblies. In addition to this, we must divide the axial dimension into slices; we choose 20 slices for the sake of illustration. This requires a mesh of size $\approx 8 \times 10^6$. The problem is further compounded by the energy of the flux being divided into energy groups; the DRAGON results in this work use 172 groups, for example. Finally, to compute the angular dependence of the flux, we must define a binning of angles; we choose 20 for a rather low estimate. This increases the number of unknowns that must be computed to about 1.6 billion for each evolution step. The problem gets worse with only modest increases of any of the above parameters.

The lattice code strategy takes advantage of the fact that the mean free path of neutrons in a reactor is $O(1)$ cm, and therefore, over the spatial extent of a fuel assembly, a neutron is most likely going to be absorbed or scattered before reaching the boundary. Thus, as far as a neutron is concerned, a fuel assembly is a 2D lattice, and for neutrons at the boundary, we choose reflective boundary conditions. Since fuel assemblies are often symmetric in their distribution of fuel rods, we can reduce calculation further by only simulating a fraction of the element. Typically, the results from a lattice are used as inputs to a finite reactor code that explicitly models the core, using reduced assembly-averaged simulations as inputs. However, it is a central point of this work that, with supplementary reactor data (see Chapter 5), the lattice stage can suffice for reactor antineutrino experiments. Thus, we do not speak of true finite-core calculations further.

3.2.2 Relevant Features of DRAGON for Reactor Antineutrino Experiments

DRAGON, like all current-generation lattice codes, can accept nuclear cross section data from a variety of inputs, including any ENDF/VI-formatted libraries. In this

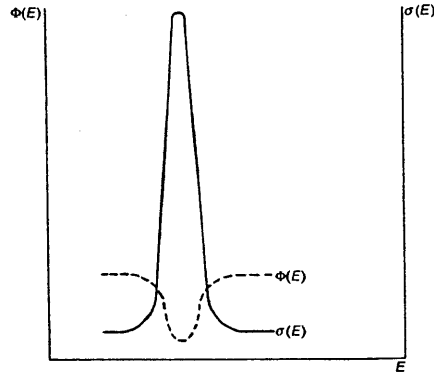


Figure 3-1: Illustration of self-shielding effects. Image from [9].

way, the code serves as a link between nuclear physics (evaluated cross section measurements) and nuclear engineering (reactor criticality and sensitivity studies)[81]. In order to compute the neutron flux and K_{eff} in the reactor element, DRAGON offers self-shielding and leakage corrections. Self-shielding occurs when the fuel itself absorbs moderated neutrons with resonance energies (see Figure 3-1)[82]. This causes a depression in the neutron flux which must be corrected. See Appendix A for an illustration of this correction in DRAGON version 3; see [81] for the USS: module in DRAGON version 4.

In addition to self-shielding corrections, we can introduce a leakage correction to the flux as well. Finally, evolving the fuel in time is of crucial importance, especially for extraction of the fission rates. This is carried out by solving the Bateman equations[81, 82], a series of coupled first-order linear differential equations that govern the evolution of the isotopic concentrations in time:

$$\frac{dN}{dt} = -N(t) \times \int_0^{\infty} \sigma_a(E)\phi(E, t) dE \quad (3.34)$$

Here, $\sigma_a(E)$ is the absorption cross section, which includes fission reactions, and ϕ is the neutron flux. Thus we see the direct importance of the neutron flux in computing the evolution of the fuel.

Having motivated the use of the DRAGON code, we now move to its validation: The Takahama benchmark.

Chapter 4

Simulation of Reactors for Anti-neutrino Experiments Using DRAGON and MURE

Having discussed several details pertinent to reactor modeling, the DRAGON simulation code in particular, we now turn to the validation of DRAGON against actual data. DRAGON has been benchmarked in a variety of scenarios[78], but as will be evident below, reactor simulations often contain a bevy of assumptions, written and unwritten. Thus, it is to our advantage to perform our own simulations and make the details as transparent as possible.

We now discuss the Takahama-3 benchmark[85], which will allow us to predict the fuel inventory in a high-burnup reactor. We produce our paper here, which was accepted into Physical Review D.

Reactor Simulation for Antineutrino Experiments using DRAGON and MURE

C.L. Jones¹, A. Bernstein², J.M. Conrad¹, Z. Djurcic³, M. Fallot⁴, L. Giot⁴, G. Keefer², A. Onillon⁴, L. Winslow¹

¹*Massachusetts Institute of Technology, 77 Massachusetts Avenue, Cambridge MA, 02139*

²*Lawrence Livermore National Laboratory, 7000 East Avenue, Livermore CA, 94550*

³*Argonne National Laboratory, 9700 S. Cass Avenue, Argonne IL, 60439 and*

⁴*Laboratoire SUBATECH, École des Mines de Nantes, Université de Nantes, CNRS/IN2P3, 4 rue Alfred Kastler, 44307 Nantes Cedex 3, France*

Rising interest in nuclear reactors as a source of antineutrinos for experiments motivates validated, fast, and accessible simulations to predict reactor fission rates. Here we present results from the DRAGON and MURE simulation codes and compare them to other industry standards for reactor core modeling. We use published data from the Takahama-3 reactor to evaluate the quality of these simulations against the independently measured fuel isotopic composition. The propagation of the uncertainty in the reactor operating parameters to the resulting antineutrino flux predictions is also discussed.

PACS numbers: 14.60.Lm, 14.60.Pq, 28.41.Ak, 28.50.Hw

As new high-power reactors come online, opportunities for reactor-based antineutrino experiments are rising. Three experiments searching for the last unknown neutrino oscillation parameter, θ_{13} [1], have released results [2–7]. New short-baseline reactor oscillation experiments [8] are motivated by the “reactor antineutrino anomaly”, a recent analysis with results that are consistent with neutrino oscillations at $\Delta m^2 \sim 1 \text{ eV}^2$ [9]. Searches for neutrino-nucleus coherent scattering [10] and studies of antineutrino-electron scattering [11] using reactor sources are also underway. Precise measurements of antineutrino rates may also permit a real-time, non-intrusive assay of the entire reactor core for nonproliferation applications [12, 13].

In the reactor core, neutron-rich fission products β -decay creating antineutrinos. The prediction of the antineutrino flux proceeds in two steps. First, the fission rates of the primary fissile isotopes are calculated. Then, this output is convolved with the antineutrino spectrum, the sum of the spectra from the β -decay of each isotope’s fission products. The antineutrino spectral predictions have recently been updated to include more detailed information on the daughter β -decay isotopes and higher-order corrections to the β energy spectrum [14, 15]. In this paper, we focus on understanding the systematic uncertainties involved in the first step, the fission rate simulations. We introduce two codes: DRAGON [16], a fast 2D parameterized simulation, and MURE (MCNP Utility for Reactor Evolution) [17, 18] a 3D Monte Carlo simulation. While neutrino experiments require fission rate predictions, reactor core simulations in industry focus on other quantities. In particular, the DRAGON code was modified by the authors to produce fission rates, whereas MURE already possessed this ability. DRAGON and MURE are used in the recent Double Chooz result [5], and DRAGON is used by the Daya Bay experiment [6].

In this work, we compare our DRAGON and MURE simulations to the Takahama-3 benchmark. This benchmark allows a comparison of absolute predictions of fissile material production to measurements from destruc-

tive assays of fuel rods from the Takahama-3 reactor in Japan [19]. The Takahama-3 benchmark is the most complete and therefore most common data set to benchmark codes against, though other data sets exist [20]. By focussing on this benchmark, we compare our results to those from proprietary reactor simulations used by industry, and demonstrate the quality of our predictions. This is an important step towards demonstrating that the predicted antineutrino fluxes are accurate.

I. OVERVIEW OF FISSILE ISOTOPE PRODUCTION

Oscillation experiments detect antineutrinos via the signal: $\bar{\nu}_e + p \rightarrow e^+ + n$, which has a threshold at 1.8 MeV. Reactors produce antineutrinos above this threshold primarily through the decay chains of four isotopes: ^{235}U , ^{238}U , ^{239}Pu and ^{241}Pu . However, we point out that both DRAGON and MURE are capable of simulating the full complement of fission products produced during the evolution of a reactor core. These include, but are not limited to, the long-lived isotopes: ^{238}Pu , ^{240}Pu , ^{242}Pu , ^{237}Np , ^{239}Np , ^{241}Am , ^{242}Am , ^{242}Cm and ^{243}Cm as well as the relatively short-lived uranium isotope ^{236}U .

The total fission rate of the four isotopes ^{235}U , ^{238}U , ^{239}Pu and ^{241}Pu is directly correlated with the total thermal power of the reactor. The exact fuel inventory has little effect on the total thermal power because the energies released per fission are very similar, 202.8 MeV per fission for ^{235}U to 211.0 MeV per fission for ^{241}Pu [21]. The antineutrino spectra per fission from these isotopes are significantly different. Consequently, the detected spectrum of antineutrinos is affected by the fuel inventory.

Most high-power reactors, including Takahama and the two Chooz reactors, are pressurized water reactors (PWRs). A PWR core is composed of approximately 200 assemblies, each assembly consisting of several hundred fuel rods. Fresh fuel rods are typically composed of UO_2 . All simulations, including DRAGON and MURE, require

a specification of the initial fuel compositions and the arrangement of the fuel rods within the assembly. Each assembly may also contain some number of instrumentation and control rods for monitoring and controlling the conditions within the assembly. The details of the assembly geometry are integral to a particular reactor design, and therefore are often characterized by the reactor manufacturer, for instance Westinghouse or Areva.

PWR fuel rods are constructed of cylindrical fuel pellets approximately 1 cm in diameter and 1 cm in length. Pellets are then stacked in the fuel rods. The structure of the rod is formed by the Zircaloy cladding. Zircaloy, chosen for its high melting point and transparency to neutrons, is composed of zirconium and trace amounts of chromium and tin. A fresh UO_2 pellet in a PWR typically consists of uranium enriched to between 2.5% to 4% ^{235}U by weight. Specifying the fuel density is important to the simulation as it sets the total amount of fuel in the volume fixed by the cladding dimensions. The density of UO_2 is 10.96 g/cm^3 at 273 K. Simulations often use an effective fuel density which accounts for the gross details of the fuel pellet packing and geometry. This effective density is called the pellet stack density. The default value for this quantity is “95% theoretical density”, and values from 9.98 g/cm^3 to 10.7 g/cm^3 are typical [22]. Because the geometry of the rod is fixed, the pellet stack density determines the total amount of fuel.

Most PWRs burn a mixture of fresh fuel assemblies and assemblies that have been through one or two fuel cycles, where a fuel cycle typically lasts about one year. The assemblies, at varying stages of evolution, are arranged to produce a precise power distribution across the core. Re-burning the assemblies maximizes the energy that is extracted from the fuel.

The assembly from the Takahama core that was used in the benchmark began as a fresh assembly and proceeded through three fuel cycles. This long irradiation makes this benchmark ideal for studying cumulative systematic effects. Systematic uncertainties come from three sources: uncertainties in the reactor data, theoretical uncertainties in the nuclear cross sections, and numerical approximations and methods used by the different codes. Among the inputs from the reactor data, we focus on the moderator temperature and fuel density of the rod, and reactor core properties such as the power and moderator boron content.

II. THE TAKAHAMA BENCHMARK

The Takahama-3 reactor is a PWR that operates with 157 fuel assemblies producing a total thermal power of 2652 MW. The assemblies have a 17×17 design, meaning there are 17×17 locations for rods. Diagrams of the Takahama core and of an assembly are shown in Fig. 1. The benchmark began with assemblies loaded with fresh UO_2 fuel rods with an initial enrichment of 4.11% ^{235}U by weight, with the remainder being ^{238}U with traces

TABLE I: Position of samples within the SF97 rod and the corresponding moderator temperature and burnup for that sample. Measurements are in mm from the top of the rod. The bottom of the rod is at 3863 mm. The moderator temperatures are those for a theoretical light water reactor [19].

Sample	Position [mm]	Mod. Temp. [K]	Burnup [GW-days/ton]
1	163	593.1	17.69
2	350	592.8	30.73
3	627	591.5	42.16
4	1839	575.8	47.03
5	2926	559.1	47.25
6	3556	554.2	40.79

of ^{234}U . Each assembly features 16 gadolinium-bearing (Gd_2O_3) fuel rods containing 2.6% ^{235}U and 6% gadolinium by weight. The original publication shows 14 Gd rods [19]; however, this number was updated to 16 in later publications [23–25].

Samples were taken from three fuel rods. Each sample was a 0.5 mm-thick disk. Each sample was dissolved, and chemical separation was performed to isolate the isotopes of interest. Isotopic dilution mass spectroscopy was used to determine uranium and plutonium inventories; different mass spectroscopy and alpha and gamma counting techniques were used to determine isotopic concentrations of the other elements. For the most relevant isotopes, namely ^{235}U , ^{238}U , ^{239}Pu , and ^{241}Pu , the uncertainty associated with the determination of the isotopic mass fractions is $<0.1\%$ for uranium isotopes and $<0.3\%$ for plutonium isotopes [19].

The three fuel rods came from two different assemblies. From the first assembly, labeled NT3G23, a normal uranium dioxide fuel rod (SF95) and a gadolinium-bearing fuel rod (SF96) were studied after two cycles. From the second assembly, labeled NT3G24, a normal uranium dioxide fuel rod (SF97) was studied after three cycles. We concentrate on SF97 because it has the longest irradiation time and therefore any cumulative systematic effects will be maximized. The rod was present in three consecutive fuel cycles of 385, 402, and 406 days with 88 days and 62 days of cool-down time between cycles. The location of SF97 within fuel assembly NT3G24 is shown in Fig. 1 as is the location of fuel assembly NT3G24 in the three fuel cycles 5, 6, and 7. Samples were taken from SF97 at the six locations indicated in Table I. Sample SF97-1 was located only 163 mm from the top of the rod, making the correct modeling of neutron leakage difficult.

The construction of the SF97 rod simulation starts with a geometric description of the fuel assembly and the initial isotopic inventory of the fuel pellets. The primary inputs used in the simulations are found in Table II. The power history for each sample was determined via the ^{148}Nd method [19, 26]. This technique provides a detailed power history in time and along the length of the rod. The integrated exposure, or burnup, from this tech-

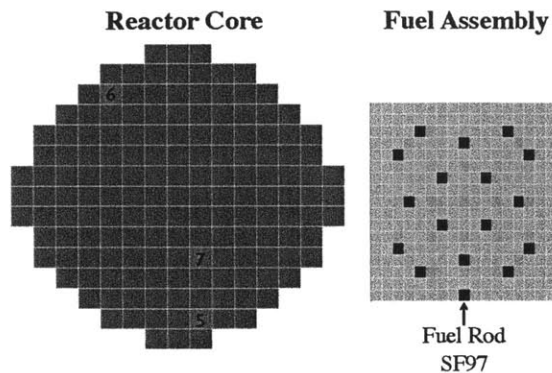


FIG. 1: Cross section of the Takahama reactor core with 157 fuel assemblies (left) and cross section of the fuel assembly (right). The location of the fuel assembly under study in fuel cycles 5, 6, 7 is indicated. In the fuel assembly, the position of the fuel rod referred to as ‘SF97’ is shown in black, $\text{UO}_2\text{-Gd}_2\text{O}_3$ rods are shown in blue, and instrumentation rods are shown in orange.

TABLE II: Takahama assembly parameters used as primary inputs to the DRAGON and MURE simulations.

Parameter	Value
Moderator Density	0.72 g/cm^3
Moderator Temperature	600.0 K
Cladding Temperature	600.0 K
Fuel Temperature	900.0 K
Fuel Density	10.07 g/cm^3
Fuel Cell Mesh	1.265 cm
Fuel Rod Radius	0.4025 cm
Fuel Cladding Radius	0.475 cm
Guide Tube Inner Radius	0.573 cm
Guide Tube Outer Radius	0.613 cm
Mean Boron Concentration	630.0 ppm

nique is summarized in Table I. We use a mean boron concentration of 630 ppm per cycle [19]. This is the standard value used by the other simulations considered in Sec. III. For the pellet stack density we use 10.07 g/cm^3 , 91% of the theoretical density, as suggested by Ref. [27]. This is lower than the standard 95% of 10.96 g/cm^3 , but is reasonable since the original paper Ref. [19] does not specify the exact value.

III. COMPARISON OF REACTOR CORE SIMULATION CODES

Most deterministic codes, including DRAGON, simulate assemblies via a lattice calculation. In a lattice calculation, one chooses a component, which is typically

either a fuel rod or a fuel assembly. The lattice component is assumed to give rise to a typical neutron flux, and therefore all surrounding components are identical, creating a lattice of these units. A Monte Carlo code, like MURE, simulates the neutron flux by actually generating and tracking neutrons.

Simulations are characterized by the number of dimensions used in the neutron transport equation they solve. Thus, codes can be 1D, 2D (like DRAGON) or 3D (like MURE). A 1D simulation models the assembly with an effective lattice component rather than taking into account the actual shape. A 2D simulation models a heterogeneous assembly, taking into account the cross sectional arrangement of the fuel cells as is illustrated in Fig. 1.

The codes used for comparison in this study are SCALE 4.4a [28], SCALE 5 [22], ORIGEN 2.1 [29], MONTEBURNS [30], and HELIOS [28]. SCALE 4.4a is a 1D code with a detailed model of the water/fuel geometry. It contains a separate module, SAS2H, for performing the fuel depletion calculations. SCALE 5 uses the 2D neutron transport model TRITON and the fuel depletion model NEWT. Its validation is described elsewhere [28, 31]. ORIGEN 2.1 is a fuel depletion code that models the buildup and decay of radioactive materials. As such, it does not model the neutron flux nor does it take the assembly geometry into account. MONTEBURNS, like MURE, is a Monte Carlo code that uses MCNP-based transport. It connects the transport abilities of MCNP with the depletion code ORIGEN 2.1. HELIOS version 1.6, like DRAGON, performs lattice calculations in a 2D plane and has a parameterized treatment of neutron transport.

Many cross section libraries are available, including ENDF/B-VI [32] and JENDL 3.2 [33], and there is no consensus on the best choice. The codes listed above use the following cross section databases as inputs: SCALE 4.4a and SCALE 5 use an ENDF/B-V library [34]. ORIGEN 2.1 uses JENDL 3.2, and MONTEBURNS and HELIOS 1.6 uses ENDF/B-VI-based libraries. We discuss systematic uncertainties in final isotopic abundance due to the choice of cross section libraries in Sec. V.

IV. COMPARISON OF SAMPLE SF97 SIMULATION RESULTS

The DRAGON simulation for rod SF97 proceeded as follows. The simulation inputs were separated into two components: time-independent, such as the initial fuel loading and the pellet radii, and time-dependent, such as the power and irradiation period. The boron concentration was kept fixed at a non-burnable value of 630 ppm, the fuel temperature was kept at 900 K, and the moderator temperature was fixed at 600 K for all samples. The input nuclear cross sections used in this simulation were ENDF/B-VI with a WIMS-style [35] transport correction, which accounts for the anisotropy in the scattering

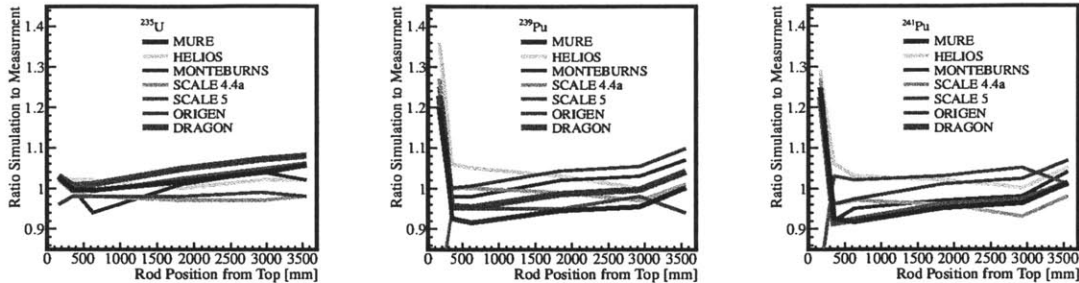


FIG. 2: Comparison of the ratio of calculated to measured mass inventories for SF97 for three isotopes important to antineutrino experiments: ^{235}U , ^{239}Pu and ^{241}Pu . DRAGON results are in green, and the MURE results are in blue. Results from other published codes are overlaid for comparison. A linear interpolation between the six samples is used.

cross section in the laboratory frame. The effect on the comparison to data is less than 1.5% for all isotopes. A correction for molecular effects is included. Results using JENDL 3.2 [33] cross section libraries are also shown.

The simulation reads in the power in time steps provided in Ref. [19]. The status of the simulation for each step is saved and used as the input to the next step. Only the final step of the simulation can be compared against the destructive assay data. However, we can use the results of all intermediate evolution steps to evaluate systematic effects in the fission rate studies as presented below.

By exploiting the symmetry of the assembly, we can model an 1/8 segment and save computation time. In each step, the neutron flux in the segment is evolved using the collision probability method with self-shielding corrections [16]. After the flux is computed, the fuel depletion module evolves the isotopic composition of the fuel by solving the Bateman equations using a Runge-Kutta method. The calculation for the full three fuel cycle evolution takes 27.5 hours on a 2.8-GHz processor. At this time, the DRAGON simulation has not been parallelized.

The MURE simulation proceeds similarly. Instead of an 1/8 segment, the full assembly is simulated in 3 dimensions with specular boundary conditions on all surfaces of the assembly. The height of the assembly was taken to be 1 cm and a different simulation was run for each sample. This effective 2D model is used to allow a comparison between deterministic versus Monte Carlo approaches. The MURE simulation starts with the generation of 10^5 neutrons. Using MCNP, these neutrons are tracked from the parent fission process until they are absorbed. This cycle of neutron generation and tracking is repeated 1900 times to ensure an equilibrium state is reached. At this point, an additional 100 cycles using 10^6 neutrons are used to calculate the parameters of interest for this time step. The fuel evolution is then calculated by solving the Bateman equations using a Runge-Kutta method. The input nuclear cross sections are once again ENDF/B-VI with molecular effects. Simulations with JENDL 3.2 [33] are

shown for comparison. Though MURE can use continuous cross sections, a multi-group treatment is used to increase the speed of these simulations. It uses 179,000 neutron groups (in comparison to DRAGON's 172 groups). The effect of the multi-group treatment compared to running with continuous cross sections is negligible. For the sensitivity studies in Section V, the number of neutrons is reduced to 10^4 and results are averaged over the assembly. The reduction in simulated neutrons increases speed, and the full three cycle evolution takes 9 hours using 10 2.5-GHz processors.

When the MURE and DRAGON simulations are complete, the results for rod SF97 are extracted. Fig. 2 shows the ratio of calculated to experimentally-measured mass inventories. The results for ^{238}U are not shown since its mass does not deplete by more than 0.1%. This is of the same order as the uncertainty in the mass inventory, and therefore does not yield a useful comparison. For the other isotopes, the DRAGON and MURE results are consistent with the data along the rod. However, there is a large deviation in SF97-1, located near the top edge of the fuel rod, which arises from approximations of neutron leakage in the axial dimension. This effect is observed in results from all the codes. The number of fissions from SF97-1 is only a third of those that we see from the other five samples.

Neglecting SF97-1, we calculate the average deviation over the rod by taking the average of the samples. For ^{235}U , the codes range from -2.2% to 4.5% with MURE at 2.1% and DRAGON at 4.3%. Even neglecting sample 1, deviations for ^{239}Pu range from MURE at -5.1% up to 6.5% for ORIGEN, while DRAGON has a deviation of -1.3%. Finally, for ^{241}Pu the codes range from -4.6% up to 3.4% with MURE and DRAGON at -4.6% and -4.4% respectively.

Since a principal aim of this work is the prediction of quantities useful to reactor antineutrino experiments, we have ensured that the simulation inputs are identical between DRAGON and MURE. The libraries used by the Monte Carlo codes only contained moderator cross section information evaluated at 600 K. Thus, in order to

TABLE III: Study of the systematic effect of varying the thermal power, fuel density, moderator temperature and boron concentration on the mass inventory for SF97-4. The ratios of the varied simulation to the nominal simulation are shown. MURE results use the average over the full assembly.

	^{235}U		^{239}Pu		^{241}Pu	
	MURE	DRAGON	MURE	DRAGON	MURE	DRAGON
Thermal Power						
+3%	0.940	0.944	0.999	1.001	1.020	1.021
-3%	1.063	1.059	1.001	0.999	0.981	0.978
Fuel Density						
+1.5%	0.992	0.991	0.988	0.989	0.990	0.992
-1.5%	1.007	1.009	1.008	1.013	1.007	1.011
Moderator Temperature						
+100K	1.025	1.024	0.938	0.940	1.000	1.002
-100K	0.969	0.973	1.073	1.069	0.994	0.996
Boron Concentration						
+10%	1.005	1.006	1.006	1.007	1.005	1.006
-10%	0.995	0.995	0.992	0.993	0.993	0.994

maintain identical inputs between our simulations, the DRAGON simulation used a moderator temperature of 600 K as well for all six samples. In fact, the moderator temperature varies along the rod as shown in Table I. The SCALE simulations used the more detailed moderator temperature and calculated the corresponding moderator density change [26]. This may explain the better performance of this code.

V. SYSTEMATIC UNCERTAINTIES

The primary systematic uncertainties in describing a reactor core for simulating fission rates were identified in Ref. [36]. We have reconfirmed that these are the major uncertainties in describing the core and present specifics for the Takahama benchmark. Beyond this, we present a systematic study of the effect of cross section uncertainties on the result.

The most significant uncertainties related to the reactor core description arise from the thermal power and the temperature of the moderator. The density of the fuel and the mean boron loading are secondary effects. The uncertainty in the specific thermal power is taken to be 3%, the uncertainty of the ^{148}Nd method [37]. Usually, simulations are given individual assembly power densities and the full core thermal power. The uncertainty for the thermal power for the core is typically <2% [36]. Though the ^{148}Nd method has a larger uncertainty, it allows for a more detailed study of the response along the rod and is the only power information available for the benchmark. The variation of moderator temperature along rod SF97 is approximately 50 K [19]. However, the continuous cross section libraries only contained evaluated data at 500 K and 700 K, and so we performed a ± 100 K variation for the moderator with both codes. MURE

used ENDF/B-VII [38] libraries that included molecular effects to improve the water model in this study and ENDF/B-VI for the other nuclei. The density of the moderator was kept constant.

We have chosen to vary the fuel density by 1.5% [39]. Both DRAGON and MURE contain parameters that can explicitly vary the fuel density. However, a simple variation of this density parameter changes the total amount of fuel. Since we seek to compare our results against an empirical determination of the inventory, we have instead elected to vary the fuel density and fuel rod radius simultaneously, while keeping the initial mass of uranium constant. The boron variation used for the study is 10% [19].

In Table III, the results are summarized for sample SF97-4. MURE ran with smaller statistics and averaged over the all of the rods of the assembly. Power variation is particularly important to the uncertainty on ^{235}U . This follows from the fact that ^{235}U is the primary reactor fuel and drives the thermal power. Since ^{239}Pu and ^{241}Pu are the products of neutron reactions on ^{238}U , they are more sensitive to changes in temperature. Increasing the amount of boron in the moderator will prohibit thermal fissions. The 10% variation in the mean boron concentration leads to a small effect, less than 0.5%.

Fig. 3 shows the effect of varying the above inputs within the systematic errors on the prediction for the SF97 data. The variations are overlaid, with the smallest effects shown on top of larger variations. In the case of ^{235}U , the variations contain both the measured mass inventory and the spread in other codes. For ^{239}Pu , the larger 100 K variation in temperature would include both measurements and the results of the other codes. In addition, the total mass of uranium can be increased by 4% by increasing the pellet stack density, improving the agreement for both plutonium isotopes.

To examine the effect of moderator temperature on our benchmark results, we held the moderator density fixed. The effect is large for ^{239}Pu because changing the moderator temperature affects the neutron capture cross section of ^{238}U , which drives the production of ^{239}Pu . In contrast, ^{235}U is the primary source of fissions, and so it is more sensitive to a power variation. We find that for ^{235}U , the uncertainty always grows. For power variations, we see the uncertainty in the plutonium isotopes reduces along the rod axis. We note that in the cases where the systematic uncertainties are large, the masses are smaller and therefore the average effect is small.

We have also examined uncertainties arising from the fission and capture cross section inputs. As mentioned in Sec. III, there is no consensus on the best choice of library. However, we note that all libraries are evaluating the cross sections based on the same data sets, and so are highly correlated. In Fig. 3, we compare the nominal ENDF/B-VI [32] to JENDL 3.2 [33]. The difference between cross section libraries is most important for ^{235}U , causing a 1.1% change in sample SF97-4 for MURE and a 3.0% effect for DRAGON. For ^{239}Pu , DRAGON shows a 0.1% effect while MURE sees a 0.7% effect. Finally, for

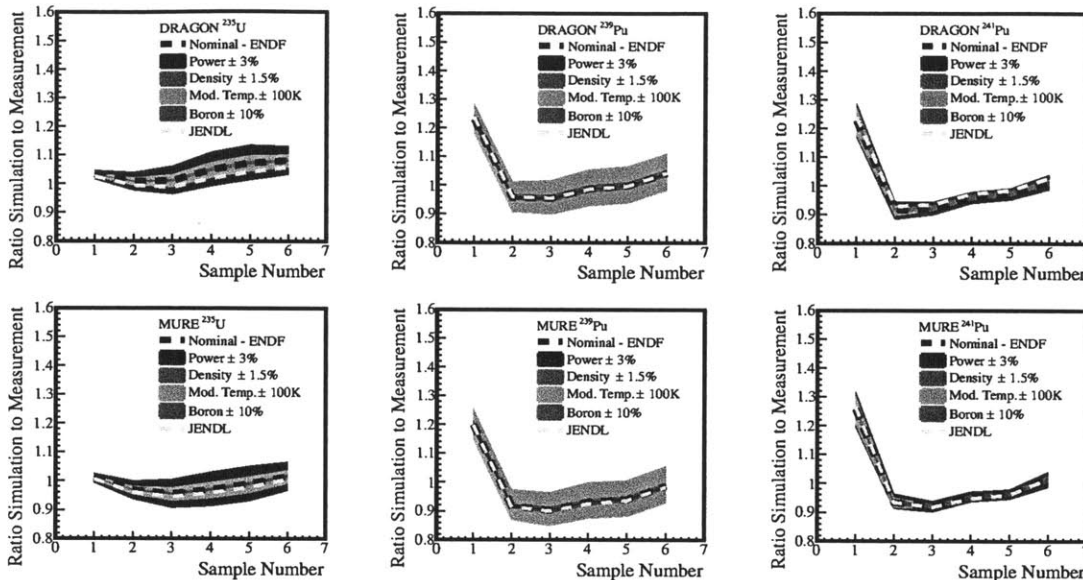


FIG. 3: Sensitivity of the Takahama benchmark predictions for SF97 to four uncertainties on the fuel rod design and operation. The uncertainties are overlaid. MURE results use the average over the full assembly. The sensitivity is plotted as a function of sample number, which can be a proxy for both the axial position along the rod as well as the burnup reached in that sample.

^{241}Pu , MURE and DRAGON see a 0.6% and 1.2% effect respectively.

MURE can easily modify the energy released per fission which is used to tie the fission rate to the thermal power measurement. In DRAGON, this is more difficult as it is integrated into the calculation with a particular cross-section library. To understand the effect of these values, MURE was run with energies per fission as calculated by DRAGON, and found this to be a 1% effect for SF97-4.

VI. CORRESPONDENCE BETWEEN MASS INVENTORY AND FISSION RATES

This paper has used comparisons of the DRAGON and MURE predictions of mass inventories to the Takahama data to demonstrate the quality of the simulations. However, neutrino experimenters are interested in fission rates rather than mass inventories. In the upper portion of Fig. 4, we show the instantaneous fission rates as a function of burnup for the assembly containing SF97. This simulation used the inputs for SF97-4 through the three fuel cycles. For a given fuel assembly, the fissions of ^{235}U dominate the antineutrino production until the beginning of the third fuel cycle, when the ^{239}Pu contributes equally. This occurs at a burnup of ~ 35 GW-days / ton. The fissions from ^{238}U and ^{241}Pu contribute approximately 10% of the flux until the end of the third fuel cycle when they reach parity with those from ^{235}U .

The difference in instantaneous fission rates between

MURE and DRAGON is on average 2.6% for ^{235}U , 2.9% for ^{238}U , 4.9% for ^{239}Pu and 9.5% for ^{241}Pu . The differences are largest during the first fuel cycle. Since great care was taken to use the same inputs, this can be used as a systematic uncertainty between Monte Carlo based codes like MURE and deterministic codes like DRAGON. We note that with some tuning of the inputs and evolution step size, some reductions in this uncertainty are possible.

Fundamentally, the Takahama benchmark is a test of a code's ability to simulate a fuel assembly. There is insufficient information about the fuel inventory and power distribution over the full core to make statements about systematic uncertainties across it. In general, fuel assemblies at the edge of the core have fission rates that are $\sim 50\%$ less than those at the center due to power variation across the core, and variations of $\sim 10\%$ are expected between neighboring assemblies due to fuel inventory differences. If given this more detailed information, a full-core simulation can be constructed, as was done for [5] and will be discussed in future work by the authors [40]. It is also difficult to make statements about fuel rods other than SF97. The power input as a function of z comes from the ^{148}Nd method, and we have this information for only rod SF97. By construction, all rods in the assembly have the same power distribution, and the assembly-averaged integrated number of fissions is the same as those from rod SF97. Since burnup is a proxy for the number of fissions, the distribution of fissions in must also agree with the provided burnup values for the samples [19]. We see in Table IV that the results of the

TABLE IV: The assembly-averaged total integrated number of fissions from DRAGON and the integrated burnup over the three fuel cycles from [19] as a function of z and normalized to sample SF97-4. The final column shows the axial neutron flux along the z -axis, also normalized to SF97-4.

Sample	z [cm]	Fissions [%]	Burnup [%]	$\sin(\pi z/H)$ [%]
1	16.3	38.4	37.6	12.78
2	35.0	66.0	65.3	27.17
3	62.7	89.9	89.6	47.35
4	183.9	100.0	100.0	100.00
5	292.6	100.5	100.5	76.79
6	355.6	87.0	86.7	36.86

simulation are consistent with the integrated burnup.

For the individual fuel rod SF97, we can make statements about the integrated number of fissions as a function of z . The axial component of the fission rate F is proportional to the axial component of the neutron flux. For an ideal cylindrical reactor, this axial component can be described analytically: $F \propto \sin \frac{\pi z}{H}$ [41] where $z = 0$ is defined as the top of the core and $H = 403$ cm is the total height of the core. The assembly-averaged integrated number of fission from DRAGON, $\int F(t) dt$, is compared to the analytical calculation in Table IV. The results across the rod are more flat for the simulation than for the analytic calculation. The contribution of SF97-1 to the total integrated number of fissions is less than half of the contribution from SF97-4, thus the larger uncertainties on this sample are mitigated by its lower contribution to the total antineutrino flux.

The correlation between the instantaneous fission rates and the mass inventories is what permits us to use the measured mass inventories to evaluate the performance of these codes. The mass inventories and the instantaneous fission rates maintain a linear correlation to first order over the three fuel cycles. This is shown in the middle part of Fig. 4. It is this relationship that allows antineutrino detectors to monitor the mass inventories in reactors for non-proliferation applications. To understand the systematic uncertainties in the fission rates, we vary the input parameters as was done in Section V for the mass inventories. The results of this study at the end of three fuel cycles are summarized in Table V, and, as with the mass variation studies, the major systematic uncertainty is the thermal power.

The systematic uncertainties are not constant as a function of burnup, as shown in the bottom part of Fig. 4. This effect is also seen in the mass studies when comparing the samples with different burnup values. During the first fuel cycle, the moderator temperature variation is the largest systematic uncertainty for the plutonium isotopes, but it is not a comparable effect for ^{235}U until a burnup of 20 GW-days / ton, halfway through the second fuel cycle. The sensitivity plots have an intersection when the upper and lower variations coincide. This crossover occurs because all variations use the same ini-

tial amount of fuel and are simply evolving it at different rates according to the varied parameter.

The technique of varying the inputs of the simulation to determine the correlated uncertainty is applicable to all reactor antineutrino analyses. However, setting a systematic uncertainty on the fission rates from the benchmark is difficult since the mass inventories are only available at the end of three fuel cycles for a limited number of fuel rods. Also, the Takahama benchmark has a 3% uncertainty in the thermal power, which is determined from the ^{148}Nd method. This value is larger than the typical $\approx 0.7\%$ from standard reactor instrumentation [36]. The benchmark also lacks detailed density information. This leads to the large systematic uncertainties in the fission rates shown in Fig. 4. For these reasons, the benchmark is used to understand the systematic uncertainty from using different codes, and to provide an upper limit on the systematic uncertainties for full-core simulations.

VII. CONCLUSIONS

This paper has demonstrated the quality of two codes available for use in the prediction of reactor antineutrino fluxes, MURE and DRAGON. We have established that MURE and DRAGON make accurate predictions based on their comparison to the well-known Takahama benchmark. They reproduce the mass inventory of rod SF97 to the level of other widely-used codes. We have demonstrated how these codes can be used to study systematic errors associated with the reactor flux predictions. We have confirmed that the thermal power is the dominant contributor to the overall uncertainty in the prediction of the mass inventory for the Takahama assembly. We have shown that the mass inventory tracks the fission rates, and thus the thermal power uncertainty can be expected to be the most important issue in predicting the flux for neutrino oscillation experiments. We have ensured that the simulations use identical inputs, and have thus provided a study of the difference between deterministic and Monte Carlo codes.

This paper has demonstrated the high quality of the simulations; however, the results presented in this paper are specific to the Takahama benchmark. General conclusions about fission rates and uncertainties cannot be drawn as each reactor core and fuel cycle is unique. Instead, we encourage neutrino experimenters to acquire the DRAGON and MURE codes to model their individual reactor cores.

Acknowledgements

The authors thank the NSF, DOE, CNRS/IN2P3 and PACEN/GEDEPEON for their generous support. The authors thank the Double Chooz collaboration for their valuable input. The authors also thank Dr. Guy Marleau

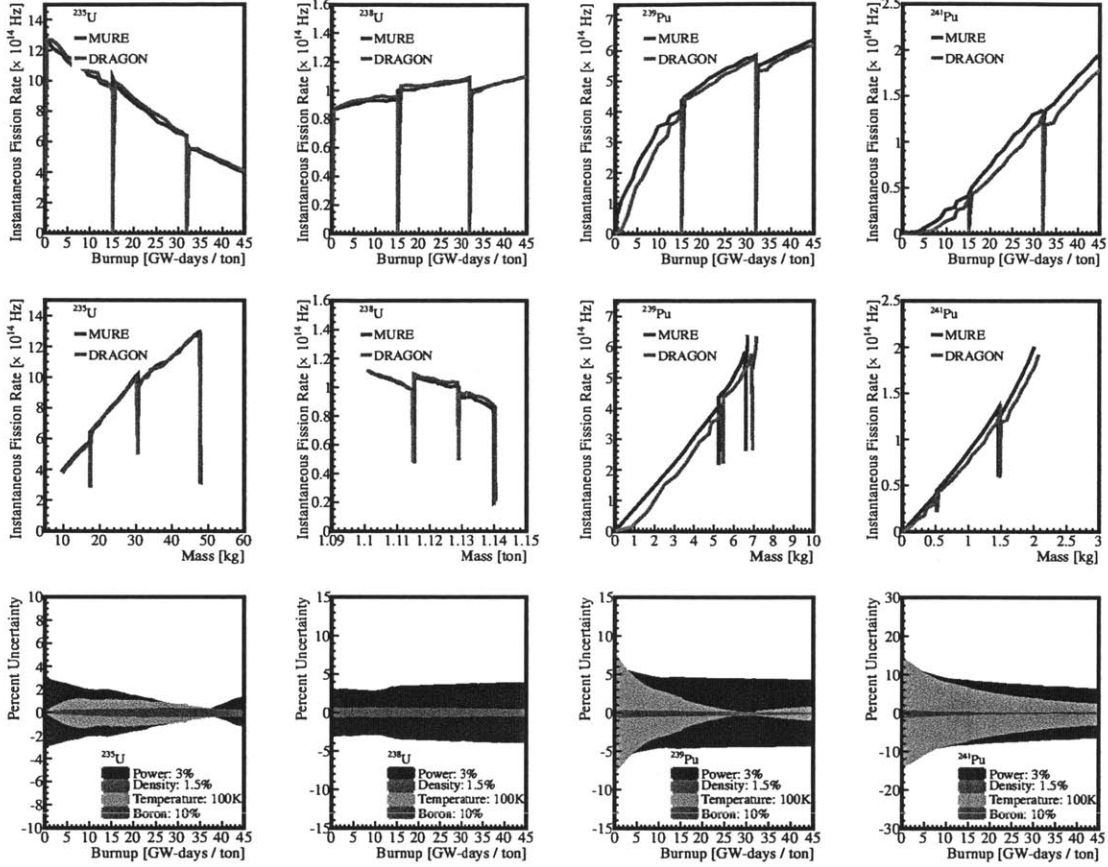


FIG. 4: Assembly-level instantaneous fission rates from DRAGON and MURE for the Takahama simulation for SF97-4. Top: Instantaneous fission rates shown for the nominal simulation. Middle: The correlation between the instantaneous fission rate and resulting mass is shown. Bottom: Sensitivity of the instantaneous fission rates to the major uncertainties in the simulation inputs. The DRAGON results are shown and are consistent with MURE.

TABLE V: Study of the systematic effect of varying the thermal power, fuel density, moderator temperature and boron concentration on the fission rates for SF97-4. The ratios of the varied simulation to the nominal simulation are shown. MURE results use the average over the full assembly.

	^{235}U		^{238}U		^{239}Pu		^{241}Pu	
	MURE	DRAGON	MURE	DRAGON	MURE	DRAGON	MURE	DRAGON
Thermal Power								
+3%	0.981	0.987	1.038	1.039	1.043	1.044	1.065	1.065
-3%	1.014	1.012	0.958	0.961	0.957	0.957	0.938	0.936
Fuel Density								
+1.5%	1.002	1.002	0.996	0.995	0.999	1.000	1.002	1.004
-1.5%	0.999	0.997	1.002	1.003	1.000	1.002	0.999	0.999
Moderator Temperature								
+100K	1.005	1.001	1.002	1.001	0.990	0.992	1.021	1.025
-100K	0.998	0.999	1.001	0.994	1.012	1.009	0.970	0.971
Boron Concentration								
+10%	0.998	0.998	0.997	1.004	1.001	1.000	0.999	0.999
-10%	1.002	1.002	0.995	0.996	1.000	1.000	0.996	1.001

and Dr. Ben Forget for extensive support in using the DRAGON code.

-
- [1] K. Nakamura et al. (Particle Data Group), J. Phys. **G37**, 075021 (2010).
- [2] F. Ardellier et al. (Double Chooz) (2006), hep-ex/0606025.
- [3] X. Guo et al. (Daya Bay) (2007), hep-ex/0701029.
- [4] J. K. Ahn et al. (RENO) (2010), 1003.1391.
- [5] Y. Abe et al. (Double Chooz), Phys. Rev. Lett. **108**, 131801 (2012), hep-ex/1112.6353.
- [6] F. P. An et al. (Daya Bay), Phys. Rev. Lett. **108**, 171803 (2012), hep-ex/1203.1669.
- [7] J. K. Ahn (RENO) (2012), hep-ex/1204.0626.
- [8] N. Bowden et al., SCRAAM (2011), URL https://www-pls.llnl.gov/data/docs/about_pls/office_of_science_programs/hep/bowden_DOE_110209.pdf.
- [9] G. Mention et al., Phys. Rev. **D83**, 073006 (2011), 1101.2755.
- [10] C. Haggmann and A. Bernstein, IEEE Trans. Nucl. Sci. **51** 2151 (2004), nucl-ex/0411004.
- [11] Z. Darakcheva (MUNU), Phys. Atom. Nucl. **67**, 1119 (2004).
- [12] A. A. Borovoi and L. A. Mikaelyan, Atomic Energy **44**, 589 (1978).
- [13] N. S. Bowden et al., J. Appl. Phys. **105**, 064902 (2009).
- [14] T. A. Mueller et al., Phys. Rev. **C83**, 054615 (2011), 1101.2663.
- [15] P. Huber, Phys. Rev. **C84**, 024617 (2011), 1106.0687.
- [16] G. Marleau et al., Report IGE-157 (1994).
- [17] O. Meplan et al., in *ENC 2005: European Nuclear Conference ; Nuclear power for the XXIst century: from basic research to high-tech industry* (2005).
- [18] NEA-1845/01 (2009), documentation for MURE.
- [19] Y. Nakahara et al., ORNL/TR-2001/01 (2001).
- [20] G. Ilas et al., ORNL/TM-2008/072 (2010).
- [21] V. Kopeikin et al., Physics of Atomic Nuclei **67**, 1892 (2004).
- [22] G. Radulescu et al., ORNL/TM-2010/44 (2010).
- [23] K. Suyama et al., Nuclear Technology **138**, 97 (2002).
- [24] N. E. Agency, *Sfcompo - spent fuel isotopic composition database* (2012), URL <http://www.oecd-nea.org/sfcompo>.
- [25] K. Suyama (2012), private communication.
- [26] C. E. Sanders and I. C. Gauld, ORNL/TM-2001/259 (2001).
- [27] B. Roque et al., NEA/NSC/DOC(2004)11 (2004).
- [28] M. D. DeHart and O. W. Hermann, ORNL/TM-13317 (1998).
- [29] S. Ludwig and J. Renier, ORNL/TM-11018 (1989).
- [30] H. M. Dalle et al., in *INAC 2009: International nuclear atlantic conference. Innovations in nuclear technology for a sustainable future* (2009).
- [31] O. W. Hermann et al., ORNL/TM-12667 (1995).
- [32] V. McLane et al., *ENDF/B-VI Summary Documentation Supplement I ENDF/HE-VI Summary Documentation* (1996).
- [33] T. Nakagawa et al., J. Nucl. Sci. Technol. **32**, 1259 (1995).
- [34] T. R. England et al., EPRI NP-3787 (1984).
- [35] J. R. Askew et al., J. Brit. Nucl. Energy Soc. **5**, 564 (1966).
- [36] Z. Djurcic et al., J. Phys. **G36**, 045002 (2009), 0808.0747.
- [37] I. C. Gauld and J. C. Ryman, ORNL/TM-2000/284 (2001).
- [38] M. Chadwick et al., Nuclear Data Sheets **112**, 2887 (2011), ISSN 0090-3752, URL <http://www.sciencedirect.com/science/article/pii/S009037521100113X>.
- [39] M. Fallot (2011), private communication from Double Chooz collaboration.
- [40] A. Onillon (2012), Private communication from Double Chooz collaboration.
- [41] E. Lewis, *Fundamentals of Nuclear Reactor Physics* (Academic Press, Massachusetts, 2008).

Chapter 5

The Double Chooz Antineutrino Flux Prediction and Uncertainty

5.1 From EDF Inputs to Antineutrino Flux

The emitted antineutrino flux is a function of both the antineutrino energy and time:

$$\frac{d^2 n_{\bar{\nu}}}{dE_{\bar{\nu}} dt} \propto \sum_k^{\text{isotopes}} f_k(t) S_k(E_{\bar{\nu}})$$

Here, the f_k are the simulated fission rates of the i th isotope from DRAGON or MURE, and S_k is the energy spectrum per fission from the k th isotope, like those from [66, 33] that we mentioned in Chapter 1. In what follows, we discuss the simulation of the f_k and the propagation of the uncertainty in the f_k and the S_k to the antineutrino flux.

5.1.1 Producing Fission Rates with EDF Inputs

In order to make a prediction of the reactor antineutrino flux from the two Chooz cores, we require several pertinent pieces of information from the French electric company Electricité de France (EDF). The DRAGON simulation in particular requires inputs at the assembly level to perform its computations.

However, the majority of the information available to us from EDF is irrelevant to our calculations. Indeed, for each of the two Chooz cores, there are approximately 3000 variables capturing the state of the reactors! The first task, then, is to select only the most relevant input information from EDF. The Double Chooz Reactor Group (DCRG) are the only members of the collaboration who, in the interest of keeping the antineutrino flux blinded, are able to have administrative access to this information. Furthermore, the data from EDF are proprietary and are restricted by EDF to the DCRG.

Within the DCRG are a smaller set of so-called “Elected Ones” (EOs) who can not only access the EDF data but also run the reactor simulation framework. The EOs are required to discuss with the greater DCRG which inputs are most important for the simulations and the general simulation strategy. The DCRG has a dedicated PC connected by landline to the EDF network. Only EOs are able to access this PC. Upon access, the EO must use a Microsoft Excel macro to download the data from EDF’s reactor database, known as EXALT. This spreadsheet can contain information in either 100-second or 12-hour increments. The DCRG has decided that simulations at the 100-second granularity are unnecessarily fine, and only performs simulations with a 12-hour δt . However, the 100-second information is stored on the private DCRG database and used to average the prediction over 1 hour periods.

Each retrieval from EXALT has a maximum size, and so the set of Excel spreadsheets must be inspected for data corruption during the retrieval. The author has written the cross-check macros to ensure continuity of the spreadsheet data as well as to properly format them for upload into a MySQL DCRG database. With these inputs from EDF, simulations of B1 and B2 can be performed. MURE constructs a full-core model, while DRAGON has an assembly model. Here, we will discuss the requisite DRAGON inputs. See Appendix A for a more detailed discussion of a DRAGON input file.

- **Geometry** For each assembly in the cores, we require a specification of the support structure and fuel rods. These details are usually endemic to a particular reactor design, for instance, by Westinghouse or Areva. Areva designed the

assemblies that comprise the N4-type Chooz cores. There are in fact a number of different assembly designs in the core, but at this stage in the core simulation, these slight differences will be ignored and all assembly designs will be taken to be of the same canonical type.

- **Initial Fuel Loading** To begin the calculation, DRAGON requires the initial configuration of fuel distribution throughout the assembly, This is called the *isotopic vector*. This information is usually given as a function of the species of fuel rod; for example, there may be an isotopic vector for pure UO₂ rods but a different one for heavy absorber rods as we saw in the Takahama-3 study. However, the information directly obtainable from EXALT is of a global nature, providing data only for the entire core and not details at the assembly level. Now we will describe how we can infer this isotopic vector with supplemental EDF inputs. The key ingredient necessary for our estimate is the neutron flux map from EDF. The flux map is a monthly report from EDF that contains several computations done at the assembly level based on flux measurements of the core. An important datum in this flux map is the burnup of each assembly as a function of time. The DCRG has been supplied the flux maps for each core for the beginning of the current fuel cycle in addition to the previous two.¹ Thus, critically, we possess information about the burnups at the very end of the fuel cycle, the subsequent rearrangement of the assemblies, and the burnups seen by each assembly at the beginning of the next cycle. The other important ingredient is the knowledge of the original fuel enrichment of the assembly, the fresh enrichment. Thus for each assembly, we have a fresh enrichment and a beginning-of-cycle (BOC) burnup. We then evolve an assembly with the fresh enrichment and evolve it at an arbitrary power until the BOC burnup is reached. At this point, the evolution stops, and we extract the isotopic vector. This vector becomes our estimate for the BOC isotopic vector. The error on the initial burnup is 5% [11].

¹Double Chooz data taking began during Cycle 12, the current cycle as of the writing of this thesis.

- **Specific Power** The reactor core is surrounded by flux monitors, which observe the neutron flux. The data from these instruments are used to compute the thermal power of the full core:

$$P = n\sigma_f\phi E_f$$

where n is the concentration of the fissile isotopes, σ_f is the fission cross section, ϕ is the neutron flux, and E_f is the energy released per fission. This power is stored in the EXALT database. The power is reported in 12-hour intervals. For blinding purposes, it was reported in 10% bins on an Analysis Group-accessible database until the data set was unblinded.

The input to DRAGON is a slightly different quantity, the specific power. This is defined as the power output of a fuel assembly per initial mass of fuel (usually uranium). Similar to that of the initial isotopic vector, the thermal power in EXALT is reported for the whole core, and thus we must compute the specific power per assembly. We must ensure that these values are consistent with the EXALT-given global thermal power. To accomplish this, we use information derived from with the flux map; we will call this the power map.

The power map assigns to each assembly a value between approximately 0.3 and 1.5 which can be taken to represent the normalized contribution to the total thermal power of the reactor at the time it was reported. The power map is updated monthly along with the flux map, which implies that we can only update the power in DRAGON approximately every 30 days with the power map, despite having global power updated every 12 hours from EXALT. For a sample computation, assume that for a particular assembly, the power map yields a value of 0.5, the reactor total power was 4 GW = 4000 MW, that there are 200 assemblies in the core, and that the initial mass of fuel in the assembly was 0.5 metric ton. Then the specific power in DRAGON for this time step is:

$$\frac{0.5 \cdot 4000}{200 \cdot 0.5} = 20 \text{ MW/T}$$

Typical values for PWRs are between 20 and 40 MW/T². To obtain this power information on the 12-hour time scale from the EXALT database, we fit the power map points with a spline. This way, at each value of the time on the EXALT database when the power is retrieved, we can also assign a value of the radial contribution factor. We can then assign an error based on the global uncertainty of the reactor power, 0.5%.

- **Boron Loading** In addition to this, the moderator surrounding the fuel rods is *borated*, containing a variable concentration of boron, ranging from about 2000 ppm at the beginning of the fuel cycle to near 0 ppm by its end. This boron loading is given as a function of time in EXALT and, even though it is a global property of the reactor core, it is applied to each assembly uniformly. Note that this boron loading is distinct from the interstitial control rods in the reactor.
- **Evolution Time** EXALT reports the boron loading and the thermal power as a function of time, so that the fuel evolution time step that DRAGON takes is 12 hours long. However, DRAGON supports the option of evolution with variable time step, which may be useful for future low-power / reactor-off background studies.

With these ingredients, we can evolve a DRAGON assembly for one time step. The output of this evolution is a new isotopic vector, the fission rates of interest, and a large amount of other information that will be called the burnfile. The burnfile contains the simulation state of DRAGON at a particular time, and so long as the burnfile for that state exists, the evolution can be resumed at any time. We then have a burnfile corresponding to each 12-hour entry in EXALT. The author has written a Python class that parses the raw DRAGON output for ease of performing further cross-checks.

²Other common equivalent units are kW/kg and W/g.

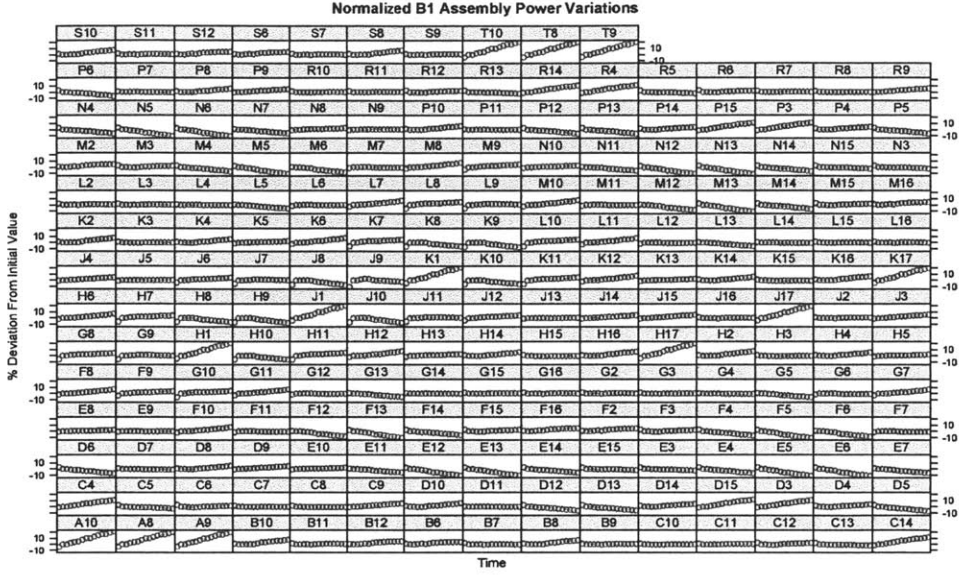


Figure 5-1: Radial contribution factors for each assembly as a function of time. The contributions have all been normalized to their initial value so that what is plotted is in fact the percent deviation.

5.1.2 Connection to Experiment: DCRxtrTools

After the fission rates are stored in a database, they can be accessed by DCRxtrTools. DCRxtrTools[86] is a toolkit that connects the efforts of the RG with that of the analysis groups. As noted in Chapter 2, it extracts fission rate information from the RG database and produces an unoscillated antineutrino flux. From this point, it also generates MC events and an associated covariance matrix whose bins are in E_{ν}^{true} . This section describes event generation. As a connection between the reactor software and detector software, DCRxtrTools requires a variety of inputs from the detector and reactors to produce an antineutrino flux:

- Detector geometry, taken from a DCGLG4sim file (see Chapter 2).
- Several non-geometrical parameters about the detectors: the distances and orientations of the detectors from the two reactors, the detector efficiency and uncertainty, the uncertainty on the number of target protons, and the components of the detector that should be considered in generating the MC,

- Gross reactor properties, such as the size and shape of the reactors, the uncertainty in the thermal power,
- A table with detector run information, specifically the run number, start time, and run duration,
- An optional list of run numbers to be processed.
- A table of fission rates as a function of time for each of the 4 important isotopes,
- A table containing reactor power information as a function of time,
- The energy spectra of the antineutrinos emitted per fissile isotope. These are typically referred to as “Schreckenbach spectra” [57]. The reanalysis of these spectra were discussed in Chapter 1.
- A specified type of interaction. Here, an analytical expression for IBD events was used: [86]

$$\sigma_{IBD}(E_{\nu}^{true}) = 0.961 \times 10^{-43} \cdot E_{e+} \sqrt{E_{e+}^2 - m_e^2}$$

Here, the units are cm^2 , and E_{e+} is the positron energy:

$$E_{e+} = \frac{1}{2} \left(-M_n + \sqrt{M_n^2 - 4M_p \left(-E_{\nu} + \Delta + \frac{\Delta^2 - m_e^2}{2M_p} \right)} \right)$$

One key feature of DCRxtrTools is its ability to convert between the timestamps produced by the DCRG fission rates and the run numbers from the detector, and to perform appropriate merging of fission rate intervals into run numbers. A description of the toolkit’s function follows [86, 87]. For each run being analyzed, the run’s duration is determined, and fission rates generated during that same interval are retrieved. With the fission rates, Schreckenbach spectra, and specified interaction cross section, a histogram binned in E_{ν}^{true} is created. From this, the expected number of antineutrinos can be computed for each run. We now turn to the estimation of the error on the reactor flux.

5.2 Reactor Simulation Cross-Checks with DRAGON

The Reactor Group (RG) has no direct contact with the B1 and B2 cores, and EDF does not generate fission rates with which we can compare our simulations as a reference. Thus, we must rely solely on indirect cross-checks to validate our fission rate predictions. These cross-checks include examining the thermal power expected shape of the fission rate curves as well as comparing DRAGON simulations to an example EDF APOLLO simulation. We briefly go over both.

5.2.1 Thermal Power

DRAGON simulates fuel assemblies and requires the thermal power in each assembly to be provided as an input. Figure 5-3 shows the reactor thermal power for B1 and B2. This input consists of a product of 3 components:

- The nominal thermal power of the core, 4.25 GW,
- The radial contribution factor as a function of time, which is a number in the approximate range [0.25, 1.3] that represents the contribution towards the total thermal power of the core,
- The percent of nominal power of the core as a function of time, which comes from the EDF EXALT database.

The actual input into DRAGON is not simply the thermal power, but the specific power, which is the thermal power divided by the initial mass of fuel (see Section 5.1). A simple cross-check is to ascertain whether the thermal power we input can be constructed from its output. The power at any given time can be computed from the fission rates from DRAGON by:

$$P(t) = \sum_i^4 f_i(t) \cdot E_i$$

where we sum over the 4 primary isotopes ^{235}U , ^{238}U , ^{239}Pu , and ^{241}Pu and E_i is the energy released per fission for the i th isotope. Typical deviations of DRAGON from

the EDF-derived values of the power, shown in Figure 5-4, are much less than the 0.46% uncertainty on the thermal power.

5.2.2 Fission Rate Evolution

The values of the fission rates over a finite core evolution will depend on the amount of fissile isotopes in the core; however, over time, each isotope has a characteristic evolution curve modulo core power fluctuations. The expected evolution of the four primary fission rates are as follows:

- ^{235}U , being the primary fuel in reactors like B1 and B2, fissions the most and depletes monotonically.
- ^{238}U , which only fissions for neutrons with energies in the fast (1 MeV) region, should have a slightly increasing fission rate since, for a constant thermal power, the fast neutron flux increases as uranium is depleted.
- ^{239}Pu , which is generated ultimately from neutron capture on ^{238}U , is monotonically increasing. As ^{235}U becomes depleted, its production from ^{238}U is counteracted by its own fissioning since this isotope, like ^{235}U , is fissile.
- ^{241}Pu , which is formed via $^{239}\text{Pu} \rightarrow ^{240}\text{Pu} \rightarrow ^{241}\text{Pu}$, should be monotonically increasing and follow the behavior of ^{239}Pu .

From figure 5-2, we can see that the fission rates computed from inputs for Cycle 12 have the expected shape.

5.2.3 Assembly-level Systematic Uncertainties with DRAGON

The Double Chooz reactor simulations depend critically on the initial isotopic vector of fuel in each assembly. Since this is not given to us, we must compute it ourselves. To do this, we compare our simulations to that of an example EDF APOLLO simulation of a fresh 4.0% enriched fuel assembly. This EDF simulation contained the mass inventory for each of the isotopes of interest for us. The simulation also included a

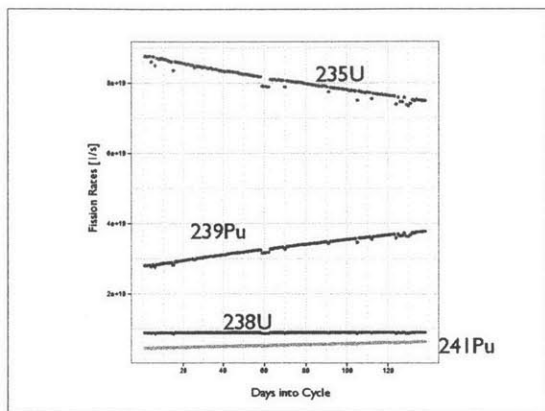


Figure 5-2: Example fission rates during a typical fuel cycle.

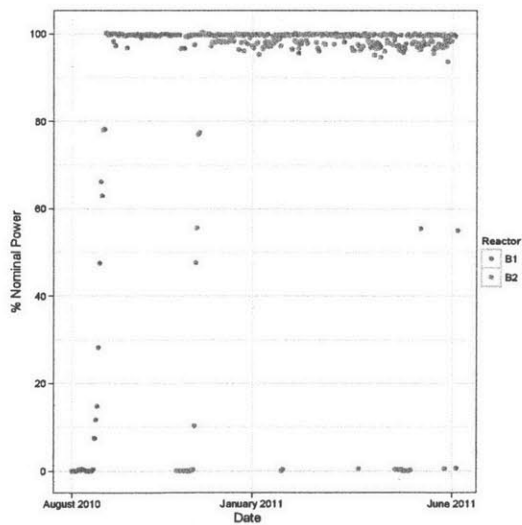


Figure 5-3: B1 and B2 thermal power for Cycle 12.

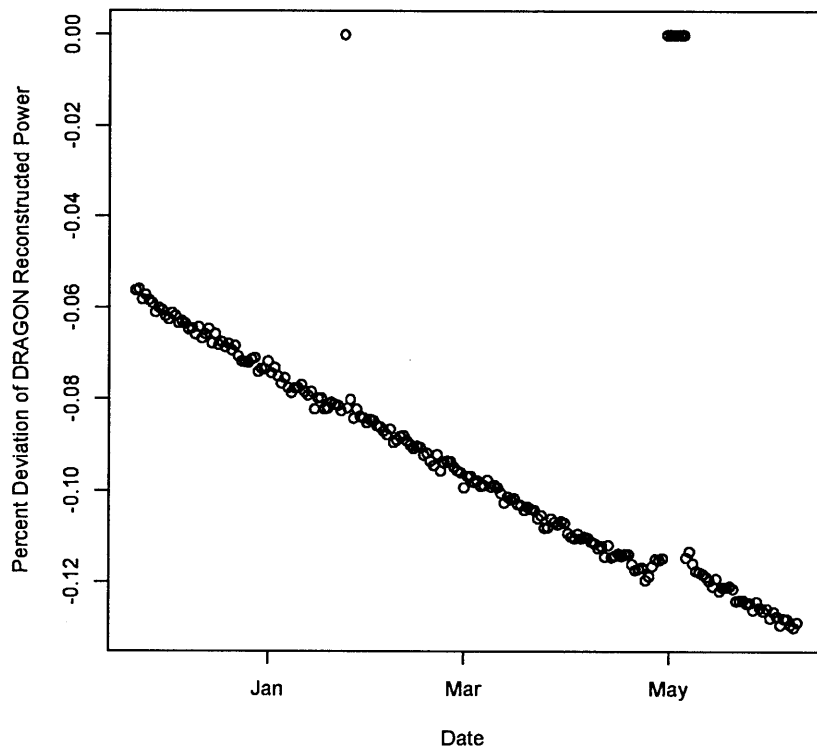


Figure 5-4: Deviation of reconstructed power from DRAGON for core B2 during Cycle 12.

calculation of k_{eff} as a function of burnup. Since we will be matching the burnup for real assemblies to our simulations of this fresh assembly, we should understand the magnitude of deviations from these simulations. The large deviations seen for low burnup for the plutonium isotopes are partially due to simulation input error and internal interpolation schemes in DRAGON.

5.2.4 k_{eff} Cross-Check

As mentioned in Chapter 3, the quantity k_{eff} is defined as the ratio of neutrons produced by fission to the number of neutrons being absorbed by fission. If a reactor is critical, then $k_{eff} = 1$, representing stability of the chain reaction. However, k_{eff} can be greater than 1 (a supercritical reactor) or less than 1 (a subcritical reactor). The example EDF APOLLO simulations include computations of k_{eff} that DRAGON should be able to reproduce. In Figure 5-5, we see the comparison between EDF and DRAGON. While the Gd-free assembly comparison shows a 0.5% deviation, the Gd simulation shows a more striking discrepancy for burnup values less than 10 GWd/T. This is due to the presence of Gd in the assembly. As neutrons are absorbed by Gd, the energy is released by photons; a proper modeling of this energy release is not present in our simulations. Once the Gd is depleted, the discrepancy disappears.

5.2.5 Systematic Uncertainty for Fission Rates

The collaboration chose to use the MURE code[79] to generate fission rates for ^{235}U , ^{239}Pu , ^{238}U , and ^{241}Pu . The DRAGON code was used to provide a cross-check of the MURE simulations at the assembly level. This check is important since DRAGON, a fast, deterministic, and 2D code, uses a very different computational philosophy than the MURE code, which is slower, Monte Carlo-based, and 3D. DRAGON's speed allowed rapid decisions to be made about the size of the uncertainties in our simulations.

We now show the DRAGON and MURE comparison to the APOLLO[83] fuel inventory simulations. Despite the agreement between DRAGON and MURE for

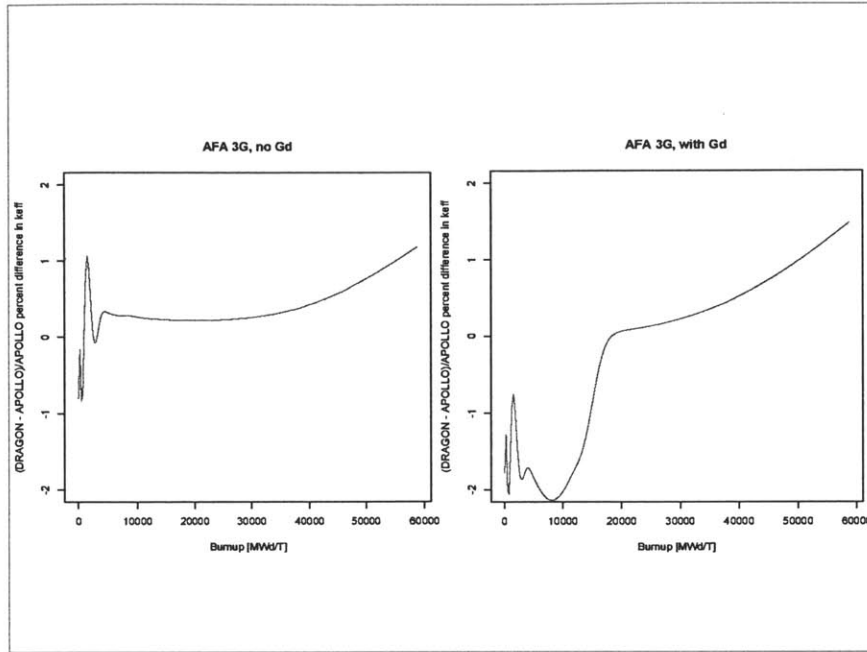


Figure 5-5: DRAGON deviation of APOLLO k_{eff} calculation for AFA 3G assembly, with and without Gd.

the Takahama-3 simulation, comparing our codes to APOLLO would allow both sets of simulations to see how they compared to EDF's own well-tuned simulation. The simulations were for 2 types of fuel assembly in the Chooz reactors: a 17×17 assembly with and without Gd absorber rods. Most of the fuel assembly types in the reactors were of these two types. Because the APOLLO simulations are proprietary, the simulation inputs and raw outputs cannot be shown; however, the percent deviation of DRAGON and MURE from APOLLO can be shown. The deviations of DRAGON from APOLLO are shown in Figures 5-6 and 5-7; the comparisons of DRAGON to MURE are shown in Figures 5-8 and 5-9. We can see that both codes agree very well with APOLLO for ^{238}U ; this is expected since the majority of the fuel ($\approx 96\%$) is composed of this isotope. The poor performance at low values of burnup are due to poorly-specified data from the EDF simulation. The codes agree to within 5% for all isotopes on the fuel inventory. The beginning of data taking was on April 13, 2011, while Cycle 12 began on September 6, 2010 for core B1 and on November 22, 2010 for core B2. Thus, data taking began 219 days into B1's cycle and 142 days into

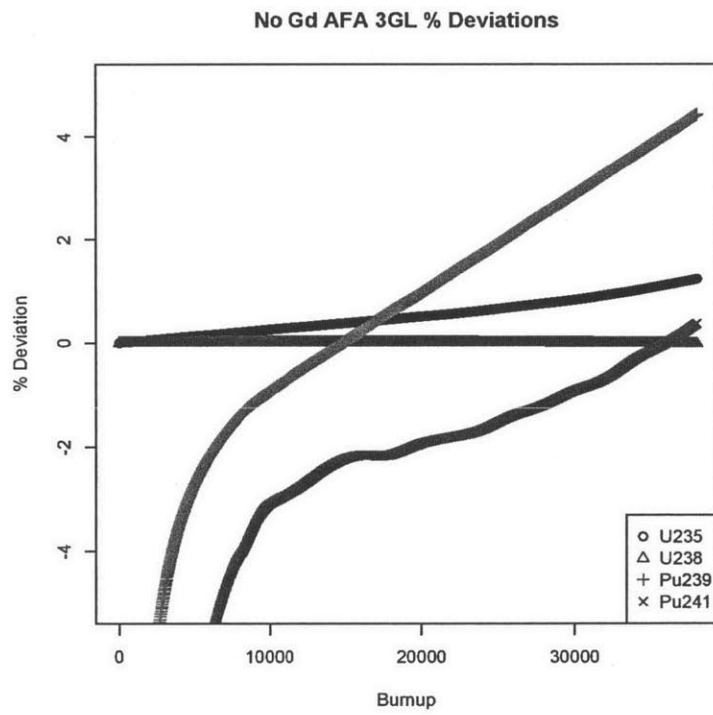


Figure 5-6: DRAGON deviation of APOLLO AFA 3G simulation without Gd. Units are in MW-day / ton.

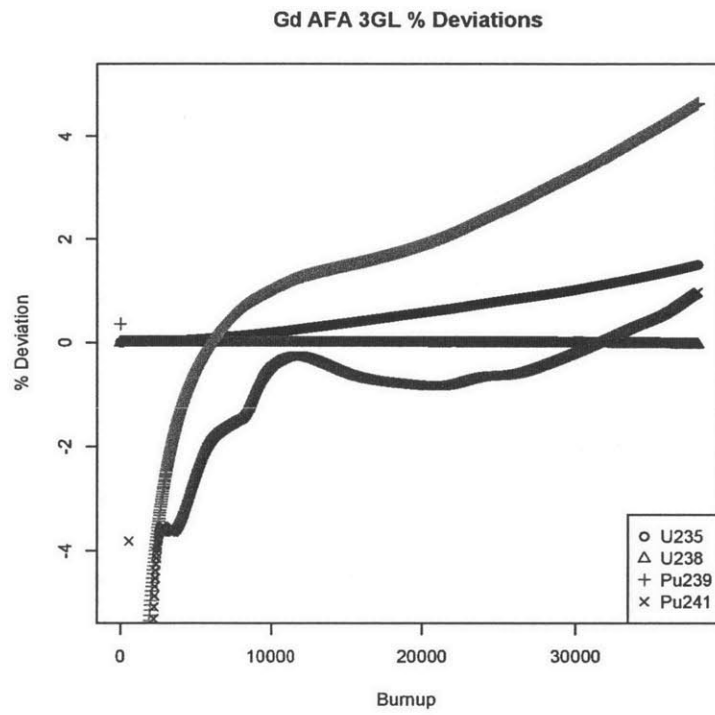


Figure 5-7: DRAGON deviation of APOLLO AFA 3G simulation with Gd. Units are in MW-day / ton.

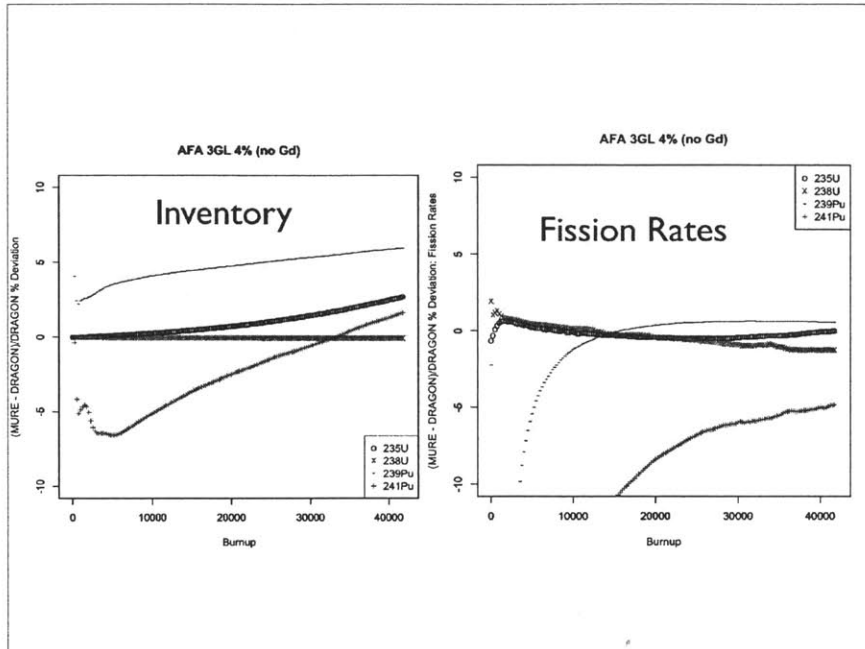


Figure 5-8: DRAGON vs. MURE for AFA 3G assembly without Gd: fuel inventory and fission rates.

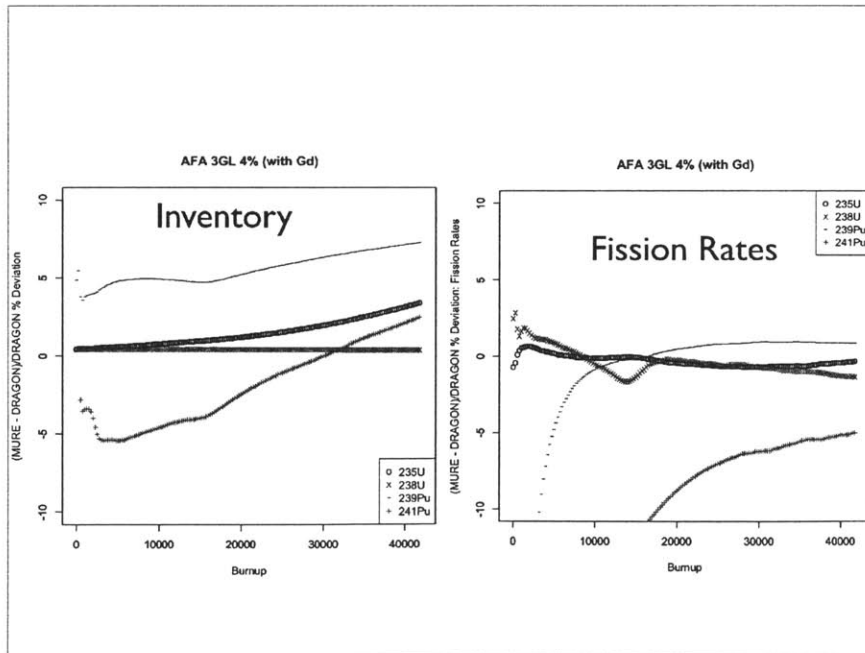


Figure 5-9: DRAGON vs. MURE for AFA 3G assembly with Gd: fuel inventory and fission rates.

Reactor Parameter	Variation
Thermal Power	1%
Boron Concentration	10%
Moderator Density	6%
Moderator Temperature	50 K
Fuel Temperature	100 K

Table 5.1: Fission rate variations, taken from [11].

B2's fuel cycle, corresponding to a burnup of approximately 8300 MWd/T for B1 and 5300 MWd/T for B2. The comparisons are thus useful to the experiment after 5300 MWd/T, and the agreement for the fission rate comparison is better than 5% for all isotopes except for ^{241}Pu , which counts for less than 7% of the total fission rate.

The influence of the Gd rods is clear when comparing the two figures. In an assembly with Gd, the neutron flux gradually diminishes the Gd until very little remains; this process manifests as the kinks in the plutonium curves. Due to the presence of Gd, the neutron flux spectrum becomes harder, providing more higher-energy neutrons to capture on ^{238}U and produce more plutonium; the kink occurs when the Gd is mostly depleted.

We move now to a discussion of the sensitivity study performed by MURE, and in particular, the validation curves that the DRAGON simulations provided. The relevant parameters to vary are listed in Table 5.1. Many of the parameters either had an uncertain central value (i.e., the moderator / water temperature), or an unknown uncertainty (such as the fuel temperature). For the former, the MURE simulations used a set of values that gave good agreement with the APOLLO AFA 3G simulations[10]. The DRAGON simulation inputs were chosen to match as closely to the MURE inputs as possible. For the latter, we chose similar variations as were used in the Takahama-3 simulation, shown in Chapter 4. Because the majority of fissions in a reactor come from fissions of ^{235}U and ^{239}Pu , the MURE group plotted the results of this sensitivity study as a function of the ratio $^{239}\text{Pu} / ^{235}\text{U}$. This ratio has other desirable features, such as the uncertainty curve's being invariant under a variation of

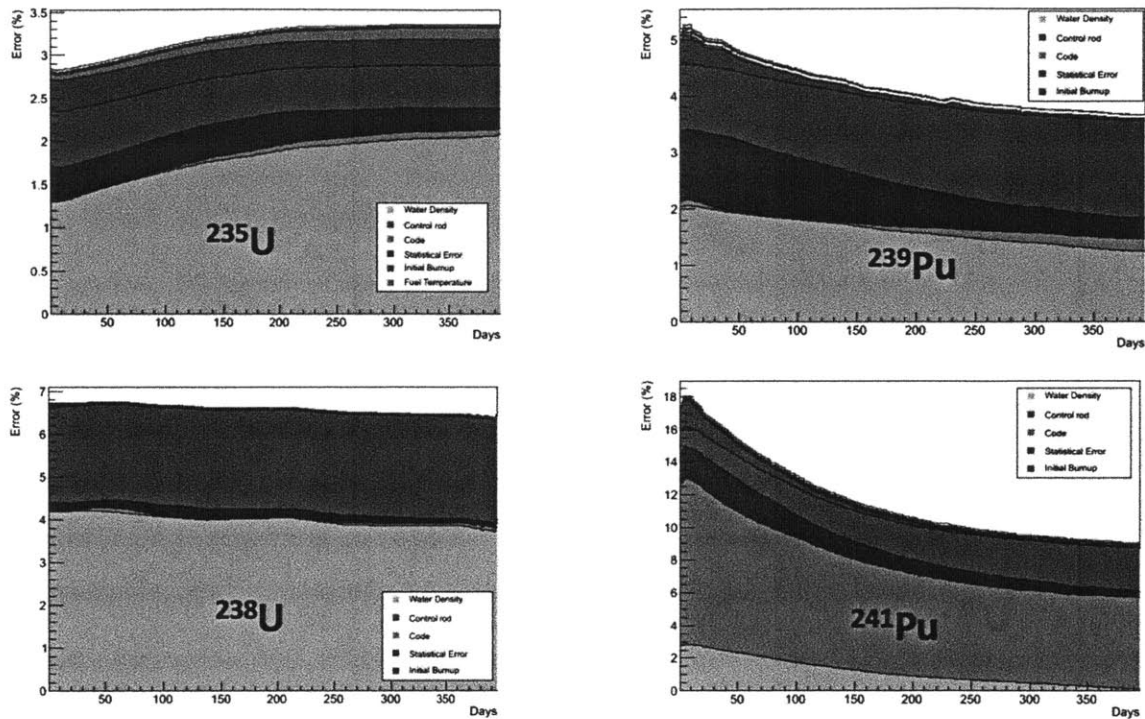


Figure 5-10: Fission rate systematic errors as a function of time. The DRAGON result is labeled “Code”. From [10].

input parameter[11]. Since the data-taking period began well after the beginning of the reactor fuel cycle, the figures highlight the relevant data-taking region. We show more conventional plots as well in Figures 5-10, which are the uncertainty curves as a function of time. It is clear from the figures that the code philosophy is far from the dominant error and in fact shows good agreement with MURE.

5.2.6 Anchoring to the Bugey-4 Reactor Experiment

In Chapter 1, we introduced the reactor antineutrino anomaly[29], which introduced a $\sim 3\%$ shift in the normalization of the antineutrino energy spectrum. At present, the nature of the anomaly is unknown, but until the near detector is completed, the analysis must contend with this shift. To avoid being sensitive to this anomaly and

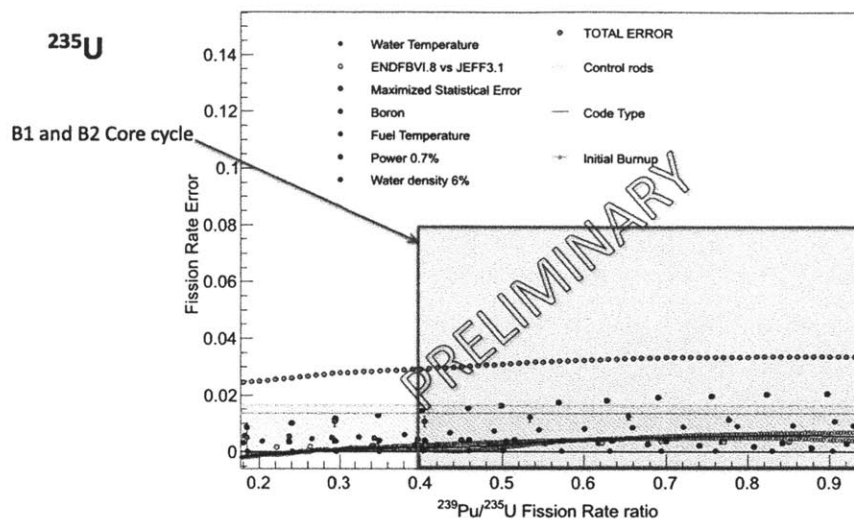


Figure 5-11: Fission rate systematic errors as a function of time. The DRAGON result is labeled “Code”. From [11].

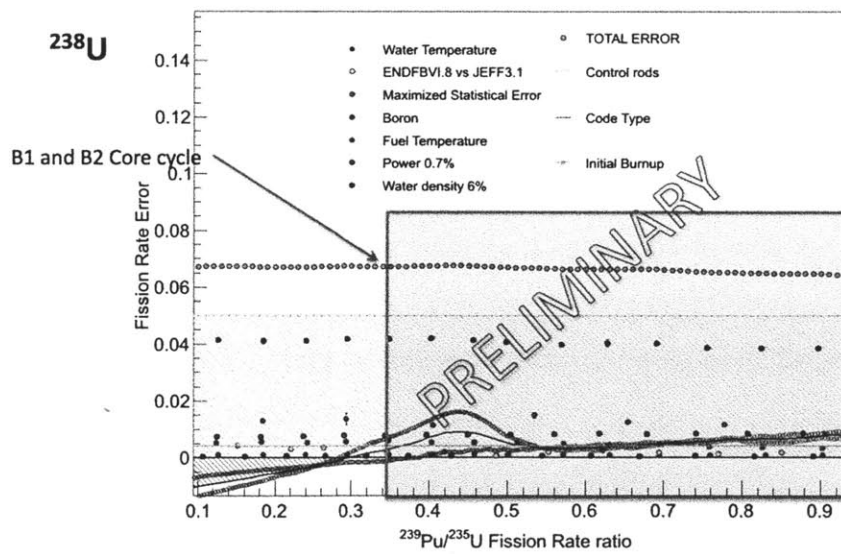


Figure 5-12: Fission rate systematic errors as a function of time. The DRAGON result is labeled “Code”. From [11].

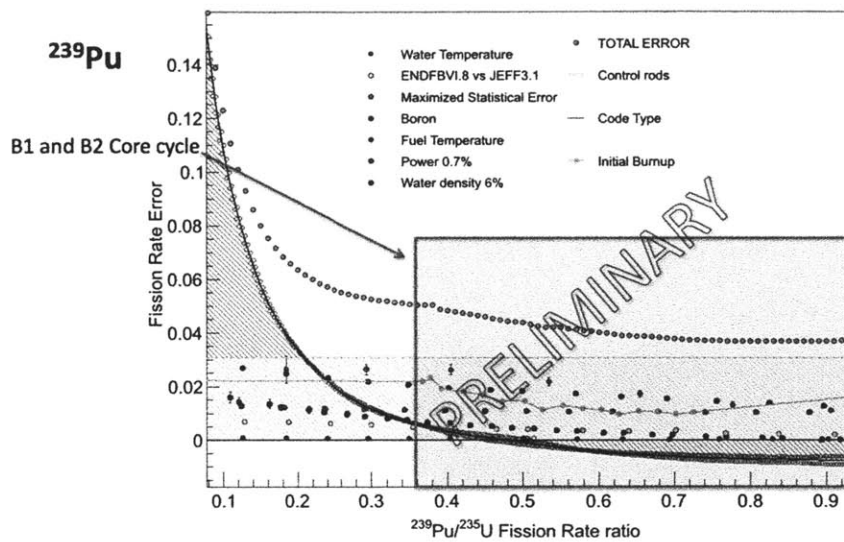


Figure 5-13: Fission rate systematic errors as a function of time. The DRAGON result is labeled “Code”. From [11].

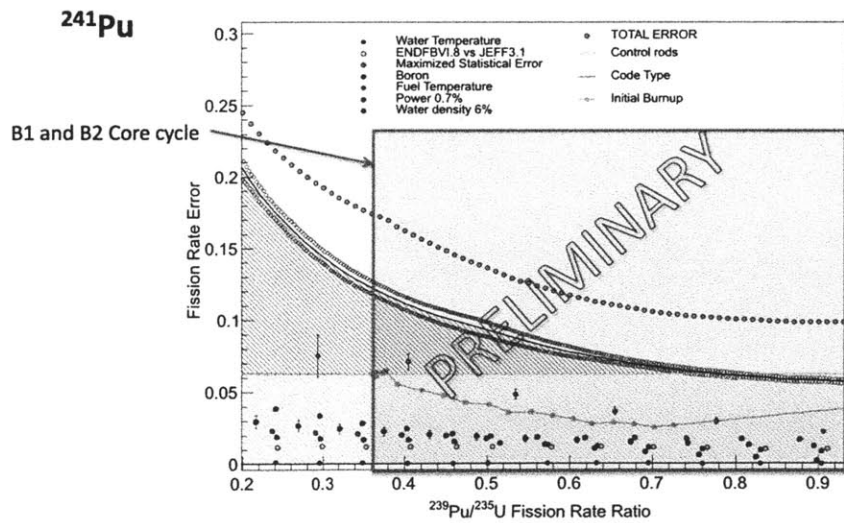


Figure 5-14: Fission rate systematic errors as a function of time. The DRAGON result is labeled “Code”. From [11].

the uncertainties in the S_k , the collaboration decided to anchor the flux calculation to that of the well-measured Bugey-4 experiment[58], as was done for CHOOZ and Palo Verde. In general, the detected antineutrino rate can be written as

$$N_\nu^{det} = N_p \epsilon \sum_{B1, B2} \frac{1}{4\pi R_i^2} \frac{P_i^{th}}{\bar{E}_i} \bar{\sigma}_f.$$

Here, N_p is the number of target protons, R_i is the baseline to the i th reactor, P_i^{th} is the thermal power of the i th reactor, \bar{E}_i is the average energy released per fission, defined as $\bar{E} = \sum_k f_k E_k$, where f_k is the fission rate of the k th isotope and E_k is its associated energy released per fission. The average fission cross section $\bar{\sigma}_f$ per reactor is defined as

$$\bar{\sigma}_i = \sum_k f_k \sum_j \int_{j\text{th energy bin}} S_k(E) \sigma_{IBD}(E) dE.$$

The S_k are the neutrino energy spectra that have recently been re-evaluated.

Since the Bugey-4 experiment reported cross sections and the average contribution of each isotope to the total number of fissions, we can “anchor” our normalization to theirs using the following formula:

$$\bar{\sigma}_f = \bar{\sigma}_{Bugey} + \sum_k (\alpha_k^i - \alpha_{Bugey}^i) (\bar{\sigma}_f)_k$$

Here, α_k is the ratio of the fission rate of the k th to the total fission rate: $\frac{f_k}{\sum_k f_k}$. The second term corrects for different fuel inventories of the Chooz and Bugey reactors. It is a small correction and makes us less sensitive to the recent cross section predictions $(\bar{\sigma}_f)_k$ [29]. The anchoring to Bugey-4 means that we share their systematic uncertainty of 1.377%.

5.3 Summary of Reactor Flux Uncertainties

Now that our anchor point has been established, we can list the final list of signal uncertainties. The uncertainties of the various inputs to the antineutrino signal are given in Table 5.2 [77]. With the reactor-related uncertainties, we can now discuss

Source of Error	Value
Bugey-4 Anchor Point	1.377%
Thermal Power	0.46%
Reference Spectra and IBD Cross Section	0.170%
Energy per Fission	0.157%
Reactor-Detector Baseline	0.038%
Fuel Composition	0.872%
Total	1.745%

Table 5.2: Reactor antineutrino signal uncertainty, taken from [30].

detector-related uncertainties and the first result in the following chapter.

Chapter 6

First Results from Double Chooz

In this chapter, we present the first Double Chooz θ_{13} measurement. We highlight the role of reactor simulations towards constraining the antineutrino flux uncertainty.

6.1 Analysis Overview

In Chapter 2, we discussed how an antineutrino candidate appears in Double Chooz. The antineutrino reacts with a proton in the liquid scintillator to produce a positron and neutron. The positron promptly deposits energy via ionization and annihilates with an electron, producing the prompt signal. Approximately $30 \mu\text{s}$ later, the neutron captures on a Gd atom in the scintillator, emitting a cascade of photons whose summed energy is 8 MeV on average. The coincidence between the prompt event and the neutron capture on Gd, called the delayed event, defines a candidate event. Now we discuss further selection criteria of candidate events.

6.1.1 Candidate Event Selection

For the first experimental result, the data-taking period began on April 13, 2011 and ended on September 18, 2011 for a total of 101.52 days of running time[30]. We now explain the selection requirements in detail:

- $E < 10,000$ DUQ (digital units of charge).

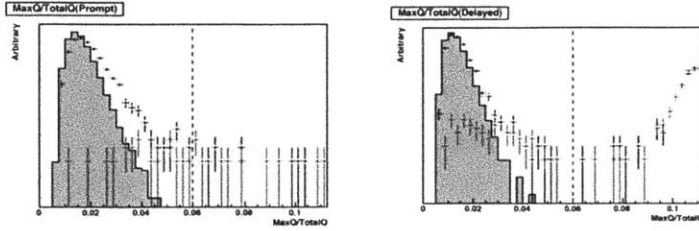


Figure 6-1: The MQTQ discriminant on prompt and delayed events. The black points are antineutrino candidates in the coincidence window $4 < \Delta t < 100\mu\text{s}$; the red points are a measurement of accidental background by looking at an off-time window of $1\text{ s} + 4\mu\text{s} < \Delta t < 1\text{ s} + 100\mu\text{s}$. From [12].

This corresponds roughly to $E < 5\text{ MeV}$. This selection vetoes cosmic-ray muons that pass through the detector target as well as fast neutrons that could recoil off of protons in the target. It applies to both prompt and delayed events.

- $\text{MQTQ} < 0.09$ for prompt events, $\text{MQTQ} < 0.06$ for delayed events.

Some PMTs have electrical sparking in their bases that creates light noise. For these “hot” PMTs, the light is localized on the PMT and is spread out in time[77]. To eliminate this type of event, we define a quantity MQTQ, which is the ratio of the maximum charge collected by a single PMT in the event to the total charge collected by all PMTs. MQTQ is effective because it has good rejection power, but does not remove IBD events [12]. Figure 6-1 shows how this discrimination on this variable helps to eliminate light noise. The figure shows events with a high (> 0.08) MQTQ are mostly caused by light noise.

- $t_{RMS} < 40\text{ ns}$.

This selection eliminates the large spread in time of light noise from the PMTs.

- $0.7 < E_{prompt} < 12.2\text{ MeV}$, $6.0 < E_{delayed} < 12.2\text{ MeV}$

The delayed energy cut serves to eliminate low-energy background and to capture the photon cascade from the neutron capture on Gd. The lower limit for the prompt event is the energy threshold. The upper limit is chosen to guaran-

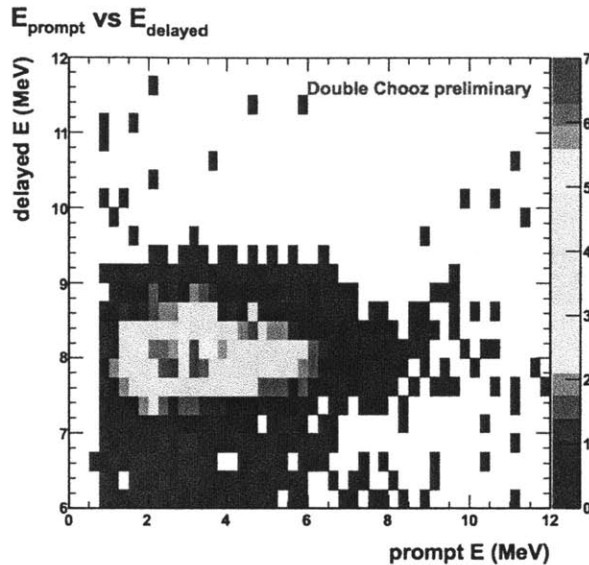


Figure 6-2: Scatter plot of prompt and delayed energy for IBD candidates. From [13].

tee that we detect all $\bar{\nu}_e$ candidates and obtain a sample of ${}^9\text{Li}$ and fast neutrons for constraints in the final oscillation fit.

- $2\mu\text{s} < \Delta t < 100\mu\text{s}$

This criterion for the coincidence selection window is to retain delayed events that have a mean neutron capture time of $\approx 30\mu\text{s}$.

- No triggers $100\mu\text{s}$ before the prompt and no triggers $400\mu\text{s}$ after the prompt event[77, 30]

This reduces correlated background from muon spallation.

In Figure 6-2, we show a plot of the candidate delayed energy versus the candidate prompt energy. This matches the equivalent image from the CHOOZ experiment mentioned in Chapter 1.

6.1.2 Backgrounds

Understanding the background is not only important for understanding our detector response, but it is also crucial to understand for the extraction of θ_{13} . A misunder-

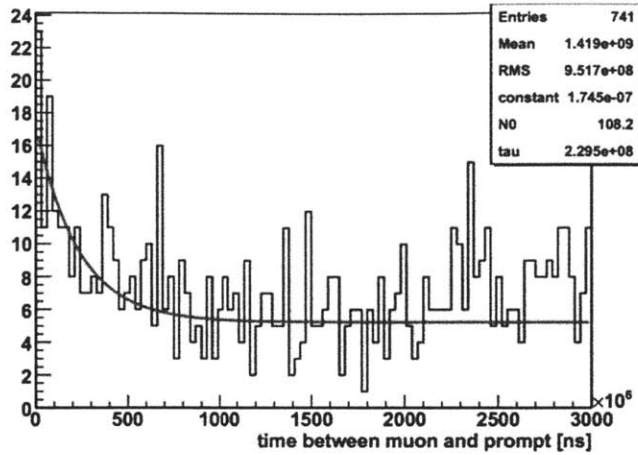


Figure 6-3: A plot of interevent time between an observed coincidence and the previous muon. From [14].

standing of background processes can lead to an incorrect prediction of the mixing angle. We examine three known sources of background events in order of decreasing importance.

6.1.2.1 ${}^9\text{Li}$ Background

The largest source of background events comes from cosmic muon spallation in the inner detector scintillator. Muon spallation creates several light radioactive isotopes; of these, ${}^9\text{Li}$ is the most problematic because it is a delayed β -emitting isotope[14], which mimics antineutrino signals. In order to estimate this background, first, ${}^9\text{Li}$ triple coincidence were searched for. For a particular coincidence, the time to the previous muon was plotted. Muons that were not involved in a coincidence appeared as a flat background, whereas muons involved in spallation exhibited an exponential decay with a characteristic time constant of the half-life of ${}^9\text{Li}$, which is 178 ms[77, 14]. See Figure 6.1.2.1 for an example. This measurement was compared to a large MC sample of ${}^9\text{Li}$ was generated in the inner detector and these MC events were passed through the IBD selection cuts. The total estimated rate from ${}^9\text{Li}$ from this fit yielded 2.3 ± 1.2 events per day.

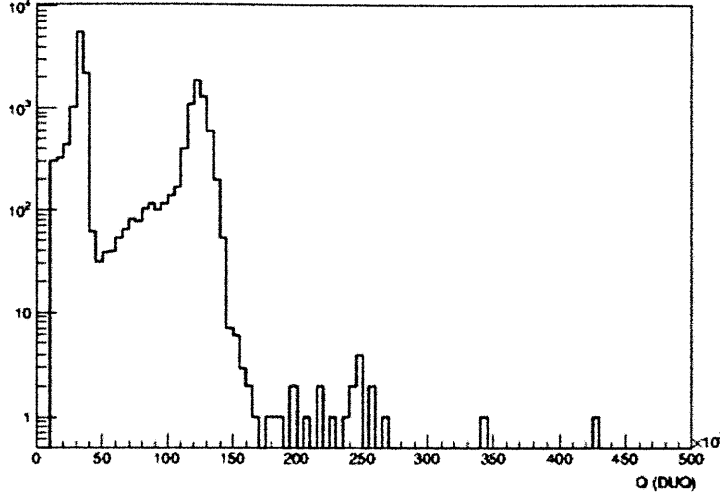


Figure 6-4: Prompt energy spectrum of coincidences happening between $40\mu\text{s}$ and $150\mu\text{s}$ after a muon. The Gd and H peaks are visible. The abscissa units are in DUQ ($15020 \text{ DUQ} \approx 1 \text{ MeV}$). From [14].

6.1.2.2 Fast Neutron and Stopped Muon Background

Cosmic muons striking the rock outside of the detector can send fast neutrons ($E > 12 \text{ MeV}$) into the detector. These fast neutrons can recoil off of protons and then capture on H or Gd, contaminating the antineutrino signal. See Figure 6.1.2.2 to see an example of fast neutron events. To estimate this background, first, the same IBD selection criteria were applied with one change: the prompt energy had to be between 12 and 30 MeV. Then, the number of events were extrapolated into the signal region, $[0.7, 12] \text{ MeV}$ [77]. In order to combine this background with that of the stopped muons, a concern was whether in fact this extrapolation of the muon energy extended to lower energies[30]. For the first publication, a flat spectrum was assumed of the low energy muons, but a large (70%) error was assigned to the shape of this spectrum. The collaboration has assigned a rate of 0.83 ± 0.38 events per day.

6.1.2.3 Accidental Background

The accidental background arises from the random association of a positron-like event with a neutron-capture-like event occurring in the IBD selection coincidence window.

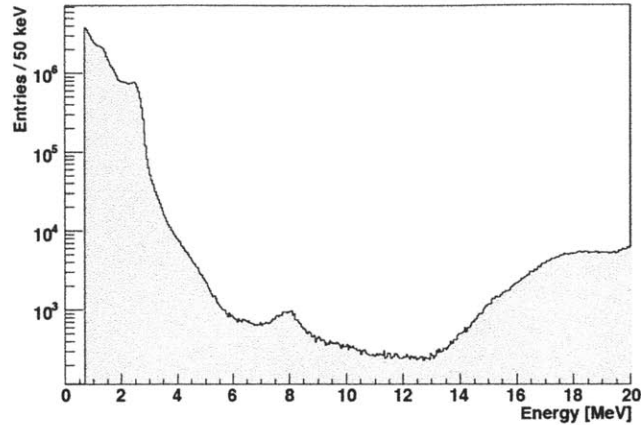


Figure 6-5: The accidental spectrum. From [15].

Positron-like events can be due to ambient radioactivity, which occurs at a rate of 7.6 Hz, whereas a subsequent neutron capture on Gd will mimic an antineutrino signal[77]. In order to measure this background, the same IBD selection cuts presented above were used with one change: the coincidence window was shifted by 1 ms. Thus, the $[2, 100] \mu\text{s}$ window is shifted into an off-time window; this is informative because if the coincidences are accidental, then the rate of these events should have a flat distribution. To further refine this measurement, the 1 ms window was split into 198 intervals, i.e., $[1.002, 1.1]$, $[1.502, 1.6]$, $[2.002, 2.1]$, etc., with each subsequent window being shifted by $500 \mu\text{s}$. The total number of candidates were summed and then scaled by $1/198$ to obtain the estimate of 0.33 ± 0.03 event per day. See Figure 6-5 for the rate of single interactions.

6.1.3 Selection Efficiencies

In this section, we discuss the detection and IBD selection efficiencies.

6.1.3.1 Target Proton Measurement

In order to determine the number of target protons, a precise measurement of the inner target scintillator weight was performed[88]. First, an empty weighing tank (WT) was weighed. Then the tank was filled with target scintillator and reweighed

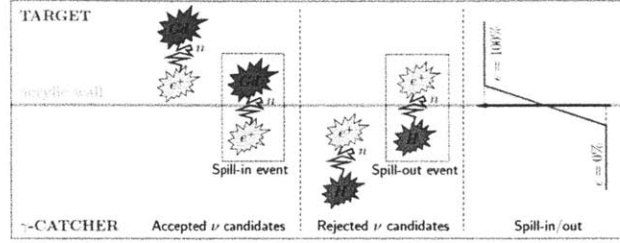


Figure 6-6: Spill-in and spill-out events. From [16].

at various heights. Then the scintillator is filled to the maximum height in the tank; due to thermal expansion, it overflowed into the XTOS (eXpansion Tank Operating System), part of the DFOS (Detector Fluid Operating System)[88, 30]. These multiple weighings, when combined with precise knowledge of the WT volume, could be converted to a number of target protons. The collaboration assigned an uncertainty of 0.295% to this measurement.

6.1.3.2 Spill-in / Spill-out Effects

From Chapter 2, we recall that a gamma catcher, which contains undoped scintillator, surrounds the doped inner target. Since the analysis cuts require that a delayed event occur on a Gd atom, it is important to understand how many Gd captures actually occurred. In [89], the spill-in and spill-out were computed from MC. Spill-in refers to the case where a neutron produced outside of the target volume travels into the target to capture on a Gd atom, and spill-out refers to a neutron created in the target that exits the target and captures on hydrogen in the gamma catcher. A spill-in event effectively increases the fiducial volume of the detector, since they allow us to record events outside of the target region. On the other hand, spill-out events cause an inefficiency in our measurement, in that we do not measure all the antineutrinos that were generated in the target. See Figure 6-6 for an illustration. In [89] and [16], it was found that the spill-in and spill-out rates were unequal, with the spill-in rate exceeding the spill-out rate by $1.37\% \pm 0.37\%$ [30]. The MC predicted a smaller net rate of 0.8% and so the MC was adjusted accordingly.

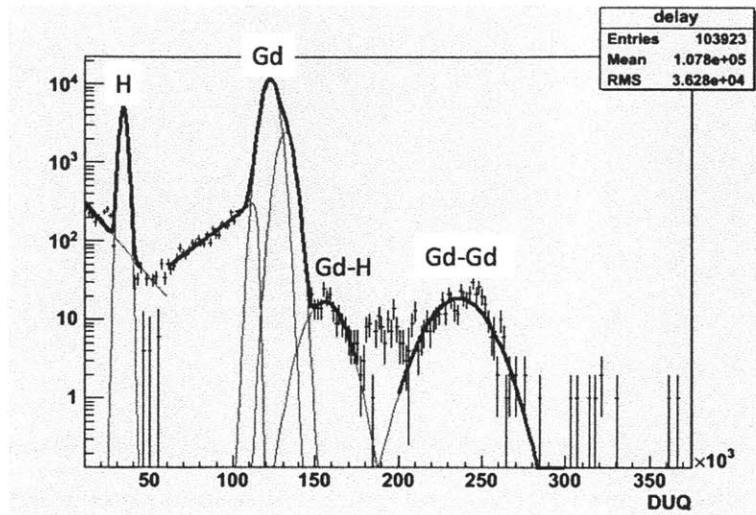


Figure 6-7: Combined fit neutron capture on Gd and H peaks. From [17].

6.1.3.3 Gd/H Ratio

An IBD candidate event requires that the delayed event contain a Gd capture, we must ascertain how many neutrons actually captured on Gd versus capture on hydrogen. That is, we want to determine the ratio $Gd / (Gd + H)$. Using ^{252}Cf calibration data along the z-axis, the fraction of neutrons that capture on Gd was estimated by a combined fit of the H peak, Gd peak, Gd-H peak, and Gd-Gd peak and comparing the relative areas of those curves[17]. See Figure 6-7 for the combined fit. The ratio was determined from data to be 0.860 ± 0.005 , compared to 0.880 ± 0.005 from MC. The MC was thus rescaled and the uncertainty was determined to be 0.6%.

6.1.3.4 Trigger Efficiency

Above the 700 keV threshold, the trigger efficiency is $\approx 100\%$ [77]. This was determined from IDLI (Inner Detector Light Injection) and IVLI (Inner Veto Light Injection) runs as well as from waveform data [90]

6.1.3.5 Efficiency of Δt cut

To evaluate the efficiency of the selection window, the amount of ^{252}Cf events in the window (2, 100) μs for the delayed event is compared to those in the window (0, 200) μs . This result is compared to the MC prediction, and the uncertainty is given as 0.5% [91].

6.1.3.6 Containment Efficiency

This efficiency takes into account the delayed energy window of (6, 12) MeV. To evaluate it, the ratio of events in the window (4, 12) MeV to those in the (6, 12) MeV are computed in both MC and data, and the associated uncertainty is 0.6% [92].

6.1.4 Detector Energy Scale

This is a brief summary of the work done for the detector energy scale; for more details, see[93]. In order to evaluate the detector response, we use the calibration methods and sources from Chapter 2 to compare to our Monte Carlo (MC) predictions. In Figure 6-8, the ratio of calibration data deployed at the center of the detector to MC is shown. In the figure, we can see that both the ^{60}Co and ^{137}Cs data exceed the MC by about 5%. The deviations from calibrations are due to phenomena not modeled in the first publication (1stPub) MC, including some reflection and optical model effects as well as nonlinearities in the electronics [30, 18]. For the 1stPub results, we use an empirical correction function; in the figure, we show the logarithmic fit. In addition to the energy-dependent correction, there is also a z-axis-dependent correction function, as seen in Figure 6.1.4. Both the energy calibration and z-axis calibration are used to form the detector covariance matrix[94]. In Table 6.1, we show the selection efficiencies and their systematic uncertainties.

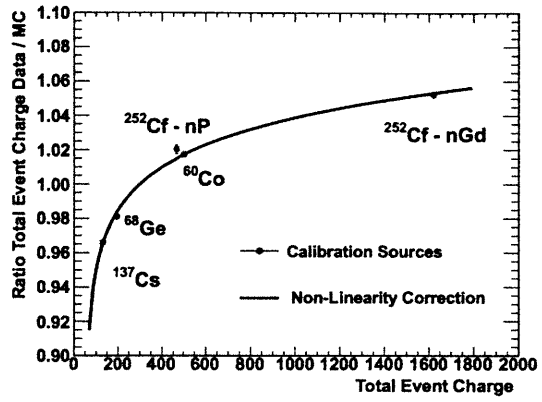


Figure 6-8: The empirical MC correction function. The reduced $\chi^2 \approx 4$. From [18].

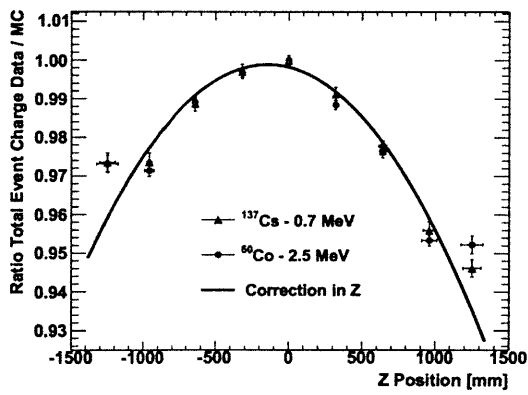


Figure 6-9: The empirical MC correction function. The reduced $\chi^2 \approx 3$ and 5 for ^{60}Co and ^{137}Cs respectively. From [18].

Uncertainty	Correction Factor	Associated Uncertainty
Muon veto	0.9547	Negligible
Isolation and multiplicity	0.995	Negligible
ΔT	1.0	0.5%
Gd/H ratio	0.98	0.58%
Delayed energy	1.0	0.6%
N_p measurement	1.0	0.3%
Trigger threshold	1.0	0.4%
Spill-in/out	0.9929	0.37%
Total	0.9243	1.1%

Table 6.1: Detector-related uncertainties, taken from [30].

6.2 Oscillation Fit

At this stage, we have a reactor antineutrino flux prediction from MURE and DCRx-trTools, whose fission rate-related errors were constrained by DRAGON simulations. In Figure 6.2, we show the ratio of the rate from data to the rate from MC as a function of time, verifying that our prediction is in good agreement with the data. In the figure, the background is subtracted and the muon dead-time is taken into account. Now we can compute the expected number of antineutrinos in a no-oscillation scenario to be used as a reference flux to be compared to actual data. Over the 101 days of data-taking, the expected number of antineutrinos should have been 4009.96 ± 108.87 (systematic uncertainty), including background[30]. The number of IBD events observed at the far detector were 4121 ± 64.195 (statistical uncertainty), corresponding to a daily rate of $42.6 d^{-1}$. From the previous section, we enumerated the background rates, which correspond to those listed in Table 6.2. With these quantities, we can calculate the ratio of observed events to expected events:

$$\frac{N_{obs} - N_{bkg}}{N_{pred}} = 0.944 \pm 0.016(stat) \pm 0.040(sys)$$

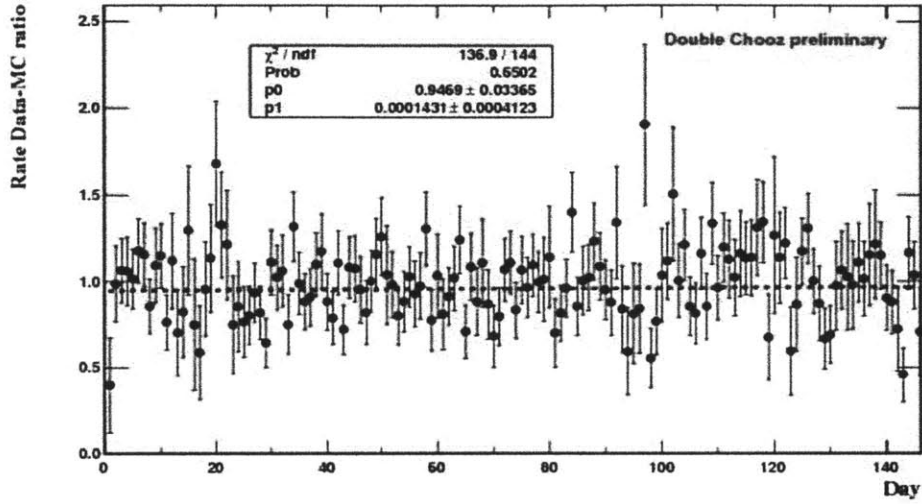


Figure 6-10: Data vs. MC rate comparison for the first publication data set, from[95].

Source of Background	Central Value and Uncertainty
${}^9\text{Li}$	222.88 ± 116.30
Correlated Background	80.90 ± 37.50
Accidental Background	32.00 ± 2.91
Total	335.78 ± 122.23

Table 6.2: Far detector backgrounds, taken from [30].

Using $\Delta m_{13}^2 = 2.4 \times 10^{-3}$, this rate-only analysis corresponds to[77]

$$(\sin^2 2\theta_{13})_{Rate} = 0.104 \pm 0.030(stat) \pm 0.076(sys)$$

We can improve the analysis by comparing the MC predicted spectral shape of the detected positron events to that measured from data. This is called a shape analysis because we perform a bin-by-bin comparison of the predicted and detected positron spectrum. See Fig 6.2. The procedure performs a χ^2 minimization with covariance matrices from the reactor signal production, detector response, background shape, and signal / background statistics. The blue dashed line is the no-oscillation prediction, which comes about from reactor simulations. The shape analysis can be combined with the rate analysis[30, 77]:

$$(\sin^2 2\theta_{13})_{Rate+Shape} = 0.0856 \pm 0.041(stat) \pm 0.030(sys)$$

We can now compare our result to those of other experiments, which we do in the next and final chapter.

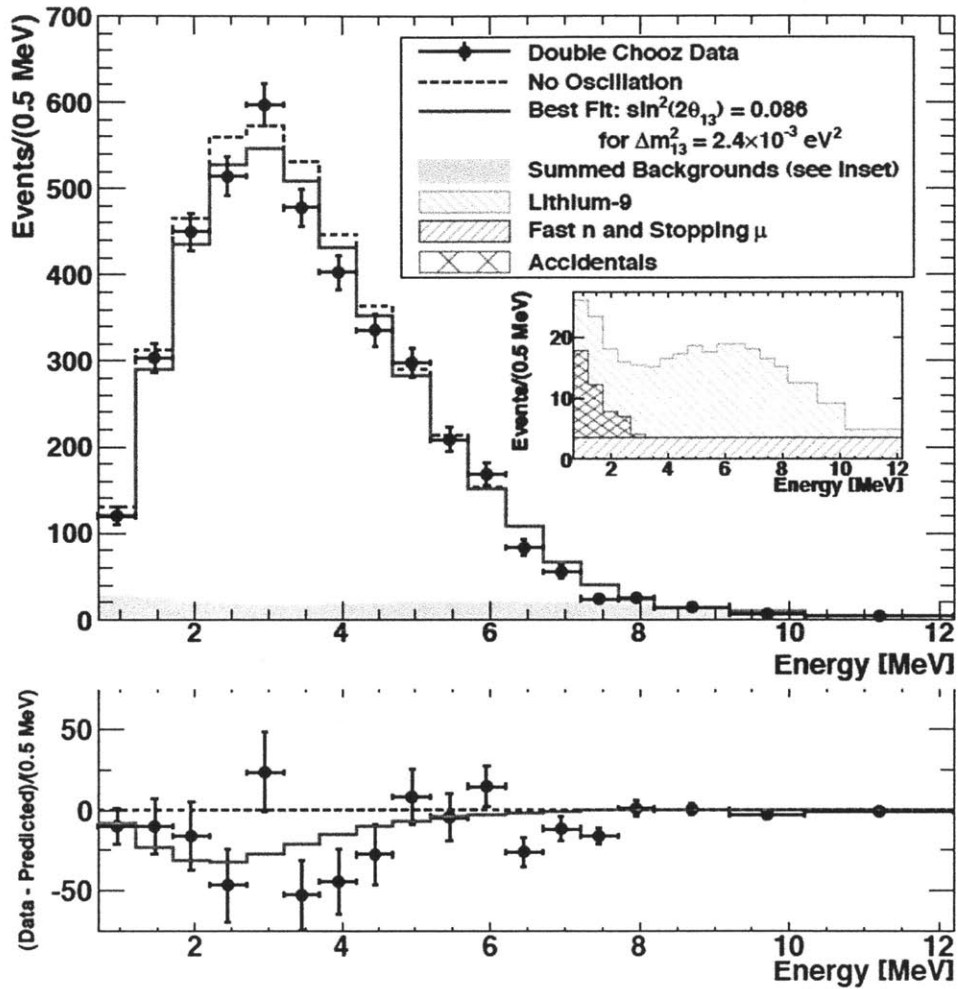


Figure 6-11: Data and best-fit spectra. The measured prompt energy spectra are shown with statistical error bars. The blue dashed line shows the no-oscillation scenario, which is predicted from reactor simulations and detector Monte Carlo. The best-fit spectra is shown in red and is derived from a χ^2 minimization technique. The green band shows the background contributions and are seen in more detail in the inset.

Chapter 7

Comparisons and Conclusions

People should stop calling θ_{13} the last unmeasured ν mixing angle; soon it will be the best measured angle.

–Maury Goodman, March 2012 long-baseline neutrino newsletter

We now move to a comparison of the Double Chooz θ_{13} result to those of recent experiments. Over the last year, May 2011 to May 2012, was a particularly fruitful time for the measurement of this mixing angle. We first discuss findings from accelerator appearance experiments. We then compare the results from the three reactor antineutrino experiments. In Figure 7-1, we show the results of 5 recent measurements of θ_{13} along with their gaussian errors.

7.1 Accelerator Appearance Experiments

Accelerator appearance experiments were mentioned in Chapter 1. These experiments produce neutrinos by focusing a beam of protons onto a fixed target, producing a hadronic shower, including charged pions which are focused with a magnetic horn. The pions then decay:

$$\pi^\pm \rightarrow \mu^\pm + \bar{\nu}_\mu(\nu_\mu)$$

The μ then decay:

$$\mu^\pm \rightarrow e^\pm + \bar{\nu}_e(\nu_e)$$

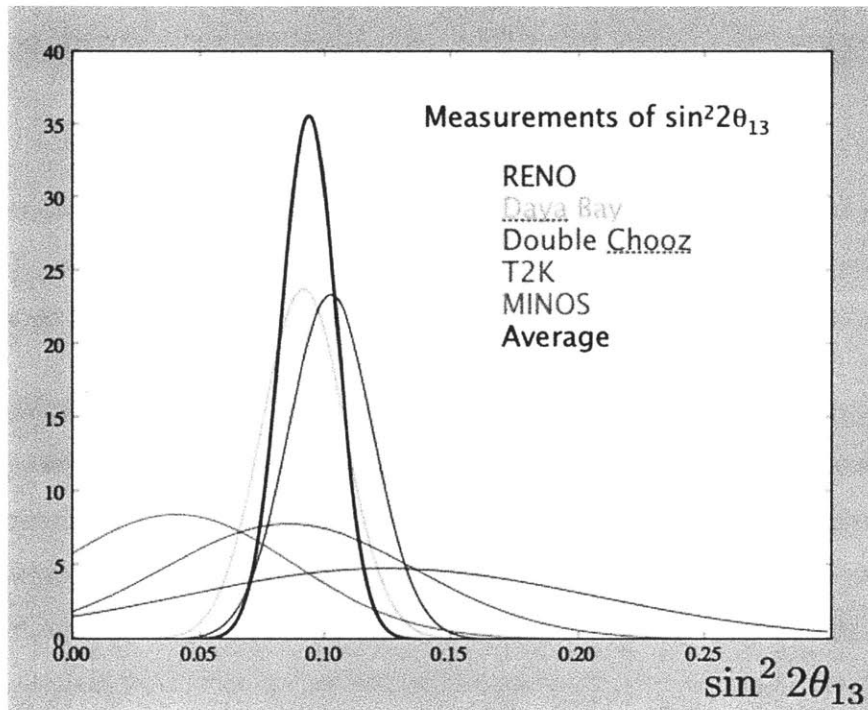


Figure 7-1: Summary of recent measurements of θ_{13} . For each experiment, the value of θ_{13} and its 1σ error is plotted, assuming a gaussian shape. The combined best-fit is also shown. The experiments comprising this plot are [20, 21, 22, 96, 77].

With a near detector, the unoscillated ν_μ flux can be compared to the far detector's flux, which will contain a ν_e component due to oscillations. We examine the results from T2K and MINOS in the following sections.

7.1.1 Results from T2K

The T2K result is reported in [19]. In July 2011, the collaboration performed a study of electron-like events at the Super-Kamiokande (SK) detector in order to search for $\nu_\mu \rightarrow \nu_e$ appearance over a span of 11 months. The signal at SK consisted of a single electron-like Cerenkov ring. The main backgrounds were ν_e that were produced by muon and kaon decays, as well as neutral current events involving $\pi^0 \rightarrow 2\gamma$ decays that were incorrectly reconstructed as a single electron in SK.

The selection requirements for a ν_e event at SK included: a diffuse Cerenkov ring, an energy above 100 MeV to remove backgrounds such as electrons from muon decays, and an energy less than 1.25 GeV in order to suppress the intrinsic ν_e contamination[19]. Also, a π^0 mass was reconstructed for each event. If the mass exceeded 105 MeV/c², the event was rejected to remove photons from π^0 decays[96]. Finally, events with delayed activity were rejected since these were interpreted as electron events from muon decays. To handle uncertainties of the neutrino flux, data from the near detector ND280 was used to renormalize the no-oscillation expectation at SK[96]: $N_{SK}^{exp} = (N_{ND280}^{data}/N_{ND280}^{MC}) \times N_{SK}^{MC}$. As shown in Figure 7-2, only 6 events passed the selection criteria. The collaboration reports an expectation of 1.5 ± 0.3 events if $\sin^2 2\theta_{13} = 0$, or 5.5 ± 1.0 events if $\sin^2 2\theta_{13} = 0.1$. The null hypothesis is converted into a 90% confidence limit: $0.03(0.04) < \sin^2 2\theta_{13} < 0.28(0.34)$ assuming $\delta_{CP} = 0$, $\Delta m_{23}^2 = 2.4 \times 10^{-3} \text{ eV}^2$ under the normal (inverted) mass hierarchy. The best fit values are

$$\sin^2 2\theta_{13} = 0.11(0.14) \tag{7.1}$$

for the normal (inverted) hierarchy.

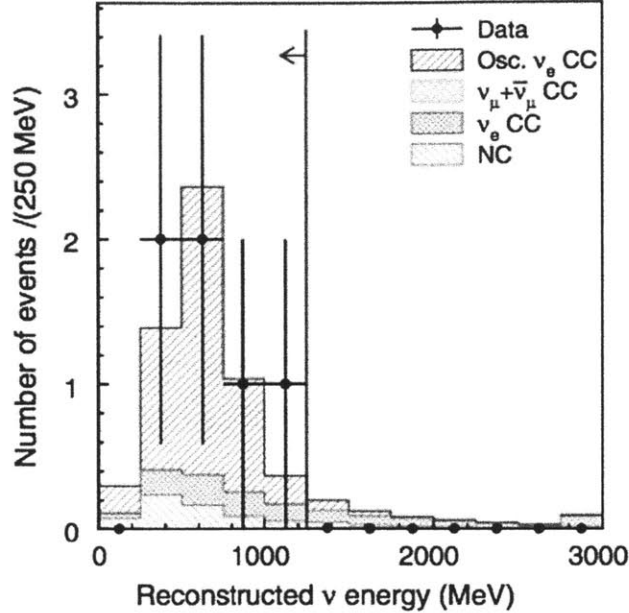


Figure 7-2: Energy spectrum of reconstructed neutrinos at T2K far detector. The blue line shows the 1.25 GeV energy cut. Taken from [19].

7.1.2 Results from MINOS

The MINOS result is described in [20]. In October 2011, the MINOS collaboration reported their study of $\nu_\mu \rightarrow \nu_e$ appearance, quickly following T2K’s result. MINOS, along with CHOOZ, had previously only set a limit for θ_{13} [97]. An outline of their analysis follows. To eliminate muon tracks from ν_μ events, a cut was placed on tracks that were longer than 24 planes or on tracks that were 15 planes beyond a hadronic shower. Events were required to have at least 5 contiguous planes and to have deposited at least half of the energy of a minimum-ionizing particle. The event energy was required to be greater than 1 GeV to eliminate neutral current background and less than 8 GeV since above this energy the $\nu_\mu \rightarrow \nu_e$ probability is negligible.

To separate signal from background, the collaboration employed a technique known as “Library Event Matching” (LEM). This algorithm compared every event that satisfied the requirements from the previous paragraph with 5×10^7 simulated signal and background events (the library), and accepted a library event if the number of

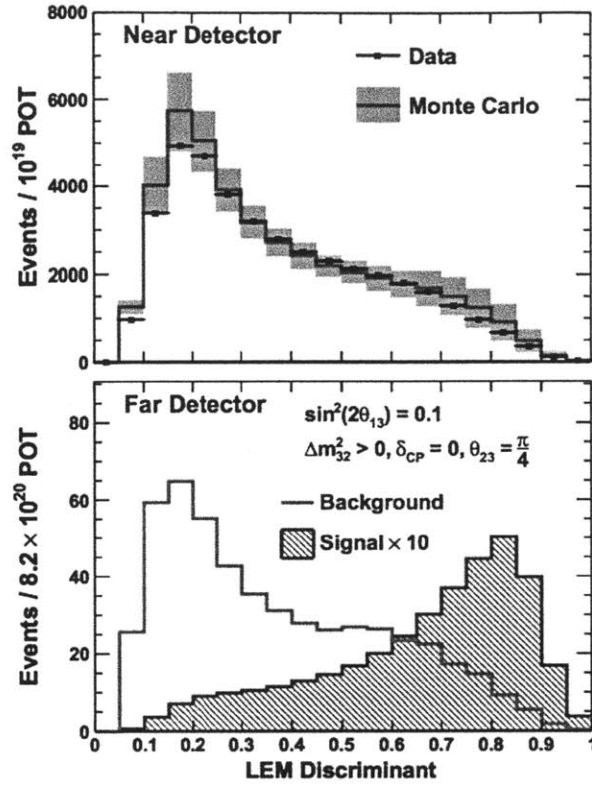


Figure 7-3: Top: MC vs. data for the MINOS near detector, with systematic uncertainty shaded in red. Bottom: Background and signal as function of the LEM discriminant, assuming $\sin^2 2\theta_{13} = 0.1$. Taken from [20].

active strips, active planes, or reconstructed energy each differed less than 20% from that of the candidate event. This comparison to library events was implemented with a likelihood minimization. Quantities such as the reconstructed energy of the event, along with statistics about the top 50 likelihood-ranked events, were fed into a neural network. The signal and background events as a function of the neural network discriminant are shown in Figure 7-3. Like T2K, MINOS used data from its near detector to constrain the prediction at the far detector[98]:

$$FD_{\alpha,i}^{\text{predicted}} = ND_{\alpha,i}^{\text{data}} \times \frac{FD_{\alpha,i}^{\text{simulation}}}{ND_{\alpha,i}^{\text{simulation}}} \quad (7.2)$$

This prediction was then used to compare against data in various bins of the LEM dis-

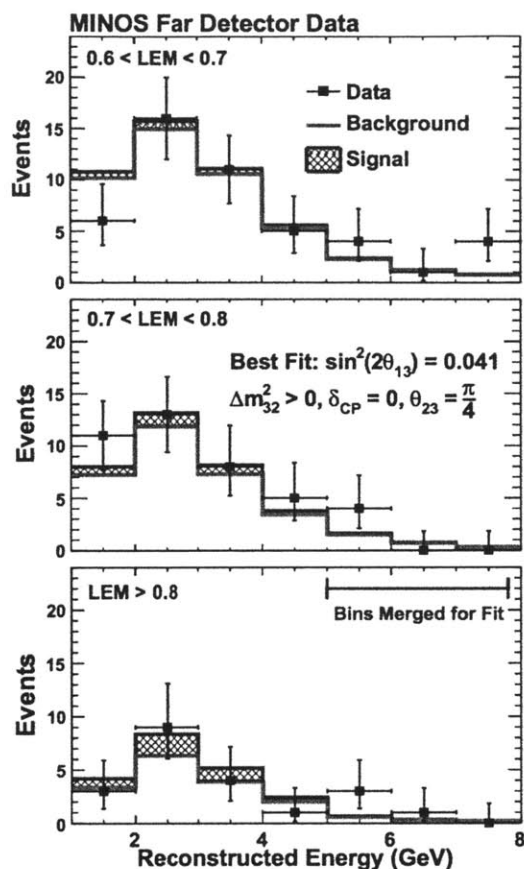


Figure 7-4: MINOS best-fit value at the far detector with multiple values of the LEM discriminant. Taken from [20].

criminant. As shown in Figure 7-4, the best-fit value of $\sin^2 2\theta_{13} = 0.041^{+0.047}_{-0.031} (0.079^{+0.071}_{-0.053})$ for the normal (inverted) hierarchy, assuming that $\theta_{23} = \frac{\pi}{4}$.

7.2 Reactor Disappearance Results

Reactor disappearance experiments were described in Chapters 1 and 2. These experiments use the large $\bar{\nu}_e$ flux from nuclear reactors to search for $\bar{\nu}_e \rightarrow \bar{\nu}_x$ oscillations at $O(1)$ km baselines. These experiments require far detectors placed 1 to 2 km from the reactors to observe a deficit in the $\bar{\nu}_e$ flux. If the experiment employs a near detector to directly measure the unoscillated $\bar{\nu}_e$ flux, it does not require a reactor antineutrino flux prediction as described in Chapter 5.

7.2.1 Results from the Daya Bay Experiment

The Daya Bay[48, 21] experiment reported observation of antineutrino disappearance from the Daya Bay and Ling Ao reactors. The collaboration used 55 days of data from December 2011 until February 2012 and saw 10,416 reactor antineutrinos at its far detector hall. For energy calibration, all 6 antineutrino detectors (ADs) used the 2.506 MeV peak of a deployed ^{60}Co source in the center of an AD. PMTs attached to the water shields surrounding the target were used as muon vetoes. Like Double Chooz, Daya Bay selected IBD candidates with prompt energy in the range [0.7, 12.0] MeV and delayed energy in the range [6.0, 12.0] MeV. Furthermore, an event was rejected if a muon in a water shield preceded a delayed event by at most $600\mu\text{s}$, if a muon that passed through the inner detector preceded a delayed event by 1 ms, or if more than 0.7 MeV was deposited in the time window $[t_{\text{prompt}} - 200\mu\text{s}, t_{\text{delayed}} + 200\mu\text{s}]$, serving as an isolation cut.

Like Double Chooz, the experiment had to consider backgrounds from accidental coincidences, ^9Li β -emission from muon spallation, and fast neutrons. In addition, they evaluated the rate of α -capture on ^{13}C and found it to contribute a rate of $\approx 0.04 \pm 0.02 \text{ d}^{-1}$ for all ADs. The small size of this background justifies its omission from the Double Chooz result. Daya Bay accounted for background events due to their own Am-C calibration neutron sources. Daya Bay also observed a spill-out deficit of 2.2% due to neutrons being created outside of the target that later drifted into it.

Due to the presence of near detectors to measure the unoscillated antineutrino flux from the reactors, Daya Bay was not sensitive to the reactor antineutrino anomaly. Despite this, the collaboration also employed the DRAGON code, but only to study the correlations of the fission rates of the 4 primary radioisotopes. The collaboration was given the fission fractions for each core as a function of burnup, eliminating the reliance on reactor simulations. Daya Bay was thus able to compute the ratio of observed to expected events by using a weighted average of the results from the near

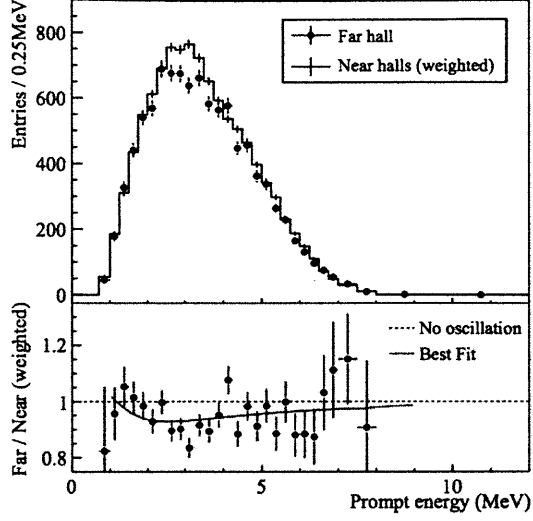


Figure 7-5: Top: The measured positron spectrum from the far hall compared to the no-oscillation expectation from the near halls. Bottom: ratio of far hall prediction to the no-oscillation scenario. Taken from [21].

detectors for the prediction:

$$R = 0.940 \pm 0.011(stat) \pm 0.004(sys) \quad (7.3)$$

Using a χ^2 minimization with pull terms, the collaboration was able to extract a measurement of $\sin^2 2\theta_{13}$:

$$\sin^2 2\theta_{13} = 0.092 \pm 0.016(stat) \pm 0.005(sys) \quad (7.4)$$

with a $\chi^2/dof = 4.26/4$. Note that this result is a rate-only fit; the spectral distortion from the positrons is only noted to be consistent with the rate-only analysis[21]. See Figure 7-5 for evidence of spectral distortion.

7.2.2 Results from the RENO Experiment

Within weeks of the Daya Bay result, the RENO collaboration[49] produced a third measurement of θ_{13} [22]. The experiment took data for 229 days, from August 2011

to March 2012. RENO observed 154,088 antineutrino candidates at its near detector, and 17,102 candidates at its far detector. RENO defined its antineutrino candidates as follows: $Q_{max}/Q_{tot} < 0.03$ for PMTs (i.e., the MQTQ variable mentioned in Chapter 6) to eliminate light noise, a rejection of all events that were 1 (10) ms after a muon with more than 70 MeV (1.5 GeV) passed through the target, the same prompt and delayed event energy cuts as Double Chooz and Daya Bay, the same coincidence window between prompt and delayed events that was used by Double Chooz, and finally, an isolation cut that rejected any coincidence pairs if they were preceded by a trigger in the inner or outer detector within 100 μ s. Like Daya Bay and Double Chooz, the primary backgrounds were ^9Li β emissions, fast neutrons, and accidental coincidences. Like Daya Bay, RENO used multiple detectors (two, in this case) to eliminate difficulties in measuring the antineutrino flux emitted from the Yonggwang reactors. They produced estimates for the contributions of each of the 4 primary radioisotopes using the Westinghouse ANC code[99]. They were able to compute the ratio of observed events to expected events:

$$R = 0.920 \pm 0.009(stat) \pm 0.014(sys) \quad (7.5)$$

Like Double Chooz and Daya Bay, RENO used a χ^2 minimization with pull terms and the collaboration was able to extract a measurement of $\sin^2 2\theta_{13}$:

$$\sin^2 2\theta_{13} = 0.113 \pm 0.013(stat) \pm 0.019(sys) \quad (7.6)$$

Like Daya Bay, RENO only provided a rate-only fit; see Figure 7-6.

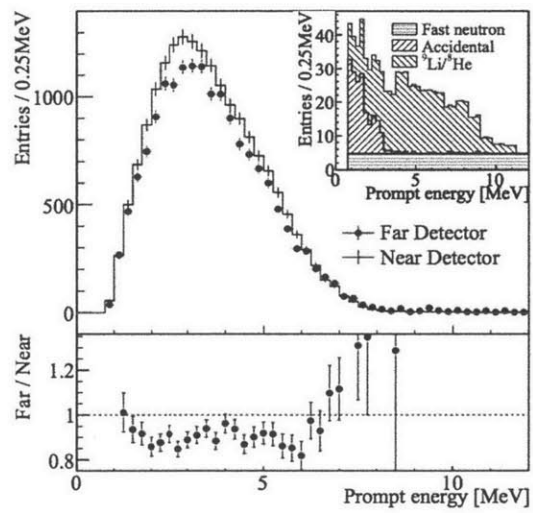


Figure 7-6: Top: distortion of the positron energy spectrum in RENO. Bottom: ratio of far detector prediction to no-oscillation scenario. Taken from [22].

Chapter 8

Conclusions

The reactor simulations performed with the DRAGON code have been instrumental in proving that our models of the Chooz reactors are well understood. These reactor models are in turn extremely important for the single-detector phase of Double Chooz as they predict the unoscillated flux. Even if the Reactor Group had direct access to fission rate measurements or predictions from EDF, it is still useful to have made our predictions, as they are instrumental for nuclear nonproliferation efforts (see Appendix B). As mentioned in Chapter 3, a DRAGON assembly simulation is usually only the first part of a full-core simulation. In order to approximate a full-core simulation with DRAGON, supplementary data such as the flux maps from Chapter 5 must be added. We have found that DRAGON lends itself very well to situations involving rapid feedback of results and to perform sensitivity studies due to its speed. However, incorporating 3D effects with it can be problematic, and using the companion code DONJON[100] can often be as time-consuming as the codes which we would like to compare it to.

Even when the Double Chooz near detector is operational in 2014, reactor simulations of the antineutrino flux will still be useful. The Near Detector flux measurement can be used to directly compare to our simulations. As we understand our simulations better with a Near Detector measurement, this will improve flux predictions in nuclear nonproliferation efforts. Work towards these efforts are given in Appendix B. In Appendix C, we perform a sensitivity study with the AFA 3G assembly simulation,

similar to our Takahama benchmark presented in Chapter 4. The speed at which the AFA 3G simulations were performed will expedite the Reactor Group's understanding of the Chooz cores.

In conclusion, we have learned that DRAGON allows us to connect the world of nuclear engineering—reactor stability and criticality, nuclear chemistry of the transuranium actinides, and neutron distributions throughout a heterogeneous core—with research in particle physics, in particular the measurement of θ_{13} . When combined with supplementary information about the reactor core as a whole, our simulations has proved useful to reactor safety studies (Takahama benchmark), neutrino physics research (the Double Chooz flux prediction), and nuclear nonproliferation (see Appendix B for the SONGS experiment). The fast, accurate, and efficient simulations performed with DRAGON have aided both nuclear nonproliferation as well as fundamental research and can continue do so long after the story of the search for θ_{13} comes to a close.

Appendix A

DRAGON Tutorial and Modifications

A.1 Code Sample and Tutorial

Here we present a sample of the DRAGON code used in the reactor simulations carried out for this thesis. The code shown below is applicable for DRAGON version 3.06H and can be obtained from the following site: <http://www.polymtl.ca/nucleaire/DRAGON/en/download/index.php>. Several of the modules listed below have been deprecated for DRAGON version 4, the experimental version of the code [101]. DRAGON is freely available and can be obtained from [102]. It can run on any platform that supports a Fortran compiler. The code below was successfully compiled with gfortran [103]. The modifications to DRAGON can be found on our DSpace archive: [104] This code is the first stage of the Takahama-3 assembly simulation. A DRAGON input file, henceforth referred to as an *input deck*, is a collection of CLE-2000 commands[105]. CLE-2000 is a system of Fortran-like procedures and commands that support the modular nature of DRAGON by providing it with a unified and uniform interface. Here, we see an example of variable declaration and assignment:

```
REAL Power := 5.00 ;
```

The := operator represents assignment, and all CLE-2000 statements must terminate with a semicolon. White space is insignificant in DRAGON; however, input in column 72 or greater will not be parsed correctly as it can represent a comment, and tab characters will always parse incorrectly and lead to an error. Variables in DRAGON can be of the typical variety found in most programming languages (integers, characters, double precision, etc.).

A.2 Linked List Directives

An input deck typically begins with a declaration of user-defined names to be introduced into the program. The LINKED_LIST directive begins a line that contains the user-defined variables. CLE-2000 can support output into a variety of formats, including ASCII and binary among others. In the following code segment, NewBurnFile, a user-defined variable, will contain plain text about the fuel evolution, and Track will be in a binary format which is more efficient for use by other DRAGON modules:

```
LINKED_LIST
  ASSMB DISCR LIBRARY CP CALC OUT BURNUP
  EDITION ;
SEQ_ASCII NewBurnFile ;
SEQ_BINARY Track ;
```

A.3 Importing Modules

The MODULE keyword informs DRAGON which elements of the code are required for the simulation. The modules here are CLE-2000 keywords; thus LIB: represents the activation of the cross section library interpolation module. The meaning of the following modules will be elaborated upon below. Failure to include the module name in this list will cause an error.

```
MODULE
```

```
LIB: GEO: EXCELT: SHI: ASM: FLU: EVO: EDI:
DELETE: END: ;
```

A.4 The LIB: module

The following segment imports the cross section libraries into the input deck.

```
LIBRARY := LIB: ::
  NMIX 6 CTRA WIMS
  DEPL LIB: WIMSD4 FIL: jendl3gx
  MIXS LIB: WIMSD4 FIL: jendl3gx
```

Now we enter the LIB: module. In the first line, we are assigning the linked list variable LIBRARY to the output of the LIB: module. The ... indicate that what follows will be a list of keyword-parameter sublists. For example, the NMIX keyword represents the number of material mixtures, such as fuel or moderator, to be treated in the simulation. In this case, there are 6 mixtures. The CTRA keyword refers to the transport correction to be applied to the cross sections, and in this case, a WIMS-style correction will be applied since the libraries are WIMS-D4 format[106]. DEPL here expects the cross section library format, which here is WIMS-D4. DRAGON can interpret several different library formats, including its own native DRAGLIB format[81]. The user is required to obtain or generate these libraries elsewhere. The name of the library is user-defined. In this simulation, the 172-group JENDL 3.2 library was used[107]. Note that none of the above code ends in a semicolon. This is because the entire LIB: module specification is a statement.

A.5 Mixtures

```
* Water / moderator
MIX 1 600.0 0.7200768
  H1H2O = '3001' 11.188
```

```
O16H2O   = '6016'   88.749
BNat      = '1011'   0.0630
```

Any line that begins with a * is a comment in CLE-2000, and thus DRAGON. The input deck will crash if the asterisk is not in the first column. The comment informs us that we are about to define the moderator for the Takahama fuel assembly. The MIX keyword labels the mixture with an arbitrary integer which must be less than 6, since NMIX was defined to be 6. The next value is the mixture temperature; thus the temperature of the water will be 600 K. The final value is the density of the mixture in g/cc. We would expect the density of water at 600 K to be less than its room temperature value, and so the value for sample SF97-4 here is about 0.72 g/cc.

The next line shows the elements and submixtures that comprise the full mixture. The mixtures contained in the LIB: module specify the initial state of the reactor. The first term in this chain of expressions (e.g., H1H2O) is a user-defined synonym for an ENDF/6-formatted[108] integer that represents the properties of the element in question. The last value represents the weight fraction in percent of the element in the mixture. Thus, we can see that oxygen-16 has a label O16H2O, is represented in ENDF/6 by the string '6016', and has a weight fraction of 11.188% in water. It is worth noting here that code '1011' represents non-soluble natural boron, which means that its value is constant throughout the course of the fuel evolution. In this case, the value is set to 630 ppm.

The user can omit the density of the material, but if this is done, instead of inputting the weight fraction of the element, the user inputs the number density of the mixture. This gives added flexibility in cases where the reactor description is incomplete and the mixture densities are unknown.

* Fuel cladding

```
MIX 2 600.0 5.821341
  CrNat   = '52' 0.0010033
  FeNat   = '2056' 0.0021067
  ZrNat   = '91' 99.689
```

In the above, we can see the mixture specification for the Zircaloy fuel cladding, and that it is almost all natural zirconium by weight.

If the sum of all of the weight percentage do not equal 100%, DRAGON will simply renormalize the inputs by the sum.

* UO2 fuel mixture

MIX 3 900.0 10.0701

O16	=	'6016'	11.852
U234	=	'234'	0.03526 1
U235	=	'2235'	3.622944 1
U238	=	'8238'	84.49 1
Pu238	=	'948'	0.0 1
Pu239	=	'6239'	0.0 1
Pu240	=	'1240'	0.0 1
Pu241	=	'1241'	0.0 1
Pu242	=	'242'	0.0 1
Pu242h	=	'1242'	0.0 1
U232	=	'232'	0.0 1
U232ps	=	'4232'	0.0 1
U233	=	'9233'	0.0 1
U236	=	'236'	0.0 1
U237	=	'927'	0.0 1
U237ps	=	'4927'	0.0 1
Np237	=	'937'	0.0 1
Np239	=	'1939'	0.0 1
Am241	=	'951'	0.0 1
Am242	=	'1952'	0.0 1
Am242m	=	'952'	0.0 1
Am243	=	'953'	0.0 1
Cm242	=	'962'	0.0 1
Cm243	=	'963'	0.0 1

Above, we see the specification for the uranium dioxide fuel mixture at 900 K and with a density of 10.07 g/cc. Of course, during the evolution of a reactor or assembly, fuel is consumed and other actinides, such as americium and curium, are produced. DRAGON will evolve these elements in time, regardless of whether they are specified as above. We explicitly list them above for 2 reasons. Firstly, notice that for all the elements save for oxygen, the last value is a "1". This is a *self-shielding index*, and it informs DRAGON that the elements sharing the same index must undergo the self-shielding process together. Since the plutonium isotopes and other higher actinides are potentially useful for important cross-checks of proper evolution, their self-shielding must be labeled in the initial state. Oxygen, not being fissile, does not undergo self-shielding and thus does not require an index (indeed, adding one will cause an error). The second reason is that it facilitates parsing of the output by the author's processing programs.

* UO₂-Gd₂O₃ fuel mixture

```
MIX 4 900.0 10.0701
U234G = '234' 0.016572 2
U235G = '2235' 2.1793 2
U238G = '8238' 80.665 2
Pu238G = '948' 0.0 2
Pu239G = '6239' 0.0 2
Pu240G = '1240' 0.0 2
Pu241G = '1241' 0.0 2
Pu242G = '242' 0.0 2
Pu242hG = '1242' 0.0 2
U232G = '232' 0.0 2
U232psG = '4232' 0.0 2
U233G = '9233' 0.0 2
U236G = '236' 0.0 2
U237G = '927' 0.0 2
U237psG = '4927' 0.0 2
```

Np237G	=	'937'	0.0	2
Np239G	=	'1939'	0.0	2
Am241G	=	'951'	0.0	2
Am242G	=	'1952'	0.0	2
Am242mG	=	'952'	0.0	2
Am243G	=	'953'	0.0	2
Cm242G	=	'962'	0.0	2
Cm243G	=	'963'	0.0	2
Gd154G	=	'2154'	0.11720	2
Gd155G	=	'2155'	0.759	2
Gd156G	=	'2156'	1.0633	2
Gd157G	=	'2157'	0.81559	2
Gd158G	=	'2158'	2.4507	2
O16G	=	'6016'	11.933	

Of the 289 ($= 17 \times 17$) fuel rods in the assembly, 25 of them contain borated water, 16 contain a $\text{UO}_2\text{-Gd}_2\text{O}_3$ mixture, and the rest are UO_2 rods. The above mixture represents the gadolinium-fuel mixture. It has a lower enrichment (2.63%), which translates to a weight percentage of about 2.18% as shown above. This illustrates that the user must compute the weight percentages of each element separately in a mixture and not merely inputting the fuel enrichment directly. The Gd rods also have a separate self-shielding index. This has been applied due to the large neutron capture cross section of Gd, and so the self-shielding procedure employed here requires its own correction which will be more detailed than that of the regular fuel rods. Again, the other element are listed despite their null values for ease in future parsing. The suffix "G" refers to "gadolinium" so that the uranium-235 in the regular fuel rods ("U235" above) can be extracted separately from that in the gadolinium-fuel mixture ("U235G").

* Guide tube material

MIX 5 COMB 2 1.0

* SF97-4

MIX 6 900.0 10.0701

O16T	=	'6016'	11.852
U234T	=	'234'	0.03526 1
U235T	=	'2235'	3.622944 1
U238T	=	'8238'	84.49 1
Pu238T	=	'948'	0.0 1
Pu239T	=	'6239'	0.0 1
Pu240T	=	'1240'	0.0 1
Pu241T	=	'1241'	0.0 1
Pu242T	=	'242'	0.0 1
Pu242hT	=	'1242'	0.0 1
U232T	=	'232'	0.0 1
U232psT	=	'4232'	0.0 1
U233T	=	'9233'	0.0 1
U236T	=	'236'	0.0 1
U237T	=	'927'	0.0 1
U237psT	=	'4927'	0.0 1
Np237T	=	'937'	0.0 1
Np239T	=	'1939'	0.0 1
Am241T	=	'951'	0.0 1
Am242T	=	'1952'	0.0 1
Am242mT	=	'952'	0.0 1
Am243T	=	'953'	0.0 1
Cm242T	=	'962'	0.0 1
Cm243T	=	'963'	0.0 1

;

Mixture 5 is, like mixture 2, composed of Zircaloy. Because it is not interesting to study the behavior of the components of this material, we can merely copy the composition from mixture 2 with the COMB (for *combine*) keyword. The value of

1.0 means that mixture 5 is made 100% of mixture 2.

Mixture 6 represents the fuel rod of interest; in this case, it is rod SF97-4. The suffix here is “T” for “target rod”. It is simple for DRAGON to simulate a fuel rod, or to simulate a full assembly. However, to extract details about a particular rod within a fuel assembly required the specification of a mixture representing the rod of interest. Then, as will be shown below, this target mixture will be assigned the required location in the reactor geometry. Since this mixture is otherwise indistinguishable from mixture 3, it is unnecessary to use a new self-shielding index. Thus to extract details for rod SF97-4, in the DRAGON output, we can search for inventory records labeled with “T”.

In a real fuel evolution/depletion calculation, it may be necessary to change the values of various mixtures as a function of time or burnup. For example, the thermal power and boron will fluctuate over the course of a fuel cycle. The LIB: module contains a special mode to enable this behavior. See the DRAGON User Manual, section 3.2.7[109].

Finally, note that the semicolon is only written at the very end of the LIB: module.

A.6 Assembly Geometry

We now illustrate the specification of the assembly geometry in DRAGON.

```
*-----  
* C1: Fuel Cell (UO2)  
* C2: Guide Tube (Zircaloy)  
* C3: Water bath (0.0538 cm thick)  
* C4: Corner water bath  
* C5: Fuel Cell (UO2-Gd2O3)  
* C6: Water bath (0.0538 cm thick)  
* CX: SF-97 (Target for benchmark)  
* CY: SF-97 (Target for benchmark)  
* CZ: SF-97 (Target for benchmark)  
*-----
```

```

ASSMB := GEO: ::
CAR2D 10 10
  X- DIAG X+ REFL Y- SYME Y+ DIAG
CELL   C2 C1 C1 C2 C1 C5 C2 C1 CX C3
        C1 C1 C1 C1 C1 C1 C1 C1 C3
          C5 C1 C1 C1 C1 C1 C1 C3
            C2 C1 C1 C2 C1 C1 C3
              C1 C1 C5 C1 C1 C3
                C2 C1 C1 C1 C3
                  C1 C1 C1 C3
                    C1 C1 C3
                      C1 C3
                        C4

```

Now that we've specified the fuel mixtures, we can set the physical location of these mixtures in our assembly. For this, we use the GEO: module, which we assign to the variable ASSMB. We begin by labeling the shape of our assembly; in this case, it is a CAR2D, for 2-dimensional Cartesian shape (i.e., rectangular grid of rods). The directive above means that we are defining a 10×10 arrangement of rods. The items labeled *CN* are the individual fuel rods, which will themselves be specified next.

The next line is the all-important declaration of boundary conditions (BCs). To understand them, first note that in fact we have only shown an *eighth* of the assembly above. We must describe to DRAGON how we would like to “unfold” this assembly until we reach its full size. It is obvious that we would like to exploit the symmetry along the diagonal. To do this, we use the expression “X- DIAG Y+ DIAG”. Here, “X-” means “incoming from the negative-X surface”, which in this case is the left side of the above arrangement. Likewise, “Y+” means “incoming from the positive-Y surface”. The combination of these two commands then instructs DRAGON to reflect the arrangement about a line passing through the upper left. It also means that DRAGON should reflect the assembly through the positive-Y and negative-X surfaces. Thus the assembly begins to unfold “upwards” and “towards the left”. A

natural question then is: do we copy the diagonal itself in this reflection, or do we merely copy around the diagonal? If we want the former, we would use the SSYM keyword, but we do not wish to duplicate the diagonal, so we use the SYME keyword. The “Y-” here means to reflect though a surface coming from the negative-Y direction (i.e., the bottom of the arrangement).

How do we get a 17×17 assembly from these BCs? To see, for a moment let us ignore the C3 and C4 cells above and pretend that we had instead specified a 9×9 Cartesian shape (CAR2D 9 9). Upon reflection through the diagonal using the SYME keyword would give us an assembly of dimensions $2 \cdot 9 - 1 \times 2 \cdot 9 - 1$ (we subtracted since the diagonal was not duplicated), or a 17×17 assembly. Finally, “X+” means “place a reflecting surface on the positive-X surface”. So the assembly begins to unfold upwards, downwards, and to the left, and on each surface, there is a reflecting BC. Cells C3 and C4 are very small cells meant to represent the very thin water bath surrounding the assembly, and so the assembly maintains its 17×17 shape even though technically it is 18×18 .

```

::: C1 := GEO: CARCEL 2
    MESHX 0.0 1.265 MESHY 0.0 1.265
    RADIUS 0.0 0.4025 0.475 MIX 3 2 1 SPLITR 2 1 ;

```

We now enumerate the properties of the individual cells making up our assembly. The “:::” operator tells DRAGON that this object is within the scope of the overall GEO: declaration. C1 is defined to be a CARCEL, meaning Cartesian cell. This is a square cell containing a series of cylindrical pins. MESHX/Y give the dimensions of the surrounding square cell in centimeters. RADIUS expects an array of numbers delineating the annular boundaries between regions in the cell. Thus we can see that this cell will be split into 3 regions, with the radius varying from [0..0.4025], [0.4025, 0.475], and [0.475, edge of cell]. Now we must assign a mixture to each region, and we do this in the same order that the regions were defined. Recall that mixture 3 was the UO₂ fuel, mixture 2 was the cladding, and mixture 1 was the moderator. We can see that the cell now consists of an inner fuel region surrounded with cladding,

which is in turn surrounded by water. Finally, SPLITR will split the cell radially in the the specified number of subregions. This is done to increase discretization which is important in mixtures that require extensive self-shielding. SPLITR 2 1 means to split the innermost (fuel) region into 2 regions, and to split the cladding into 1 region (i.e., not to split it at all). The default value for splitting is 1, which is why the outermost region did not have to be specified. We can see that C1 is our fuel cell in the configuration above.

```

::: C2 := GEO: CARCEL 2
    MESHX 0.0 1.265 MESHY 0.0 1.265
    RADIUS 0.0 0.573 0.613
    MIX 1 5 1 SPLITR 2 1 ;
::: C3 := GEO: CAR2D 1 1
    MESHX 1.265 1.3188 MESHY 0.0 1.265
    MIX 1 ;
::: C4 := GEO: CAR2D 1 1
    MESHX 1.265 1.3188 MESHY 1.265 1.3188
    MIX 1 ;

```

As mentioned previously, C3 and C4 are the “water bath” cells with a thickness of 0.0538 cm. We can see in the specification of MESHX/Y that only the δx of the mesh (size) of the cell is important to specify. Also, we can see that geometries can be defined recursively; C3 and C4 are of type CAR2D, which are both themselves embedded in a larger CAR2D structure. This allows for a variety of complicated reactor geometries.

```

::: C5 := GEO: CARCEL 2
    MESHX 0.0 1.265 MESHY 0.0 1.265
    RADIUS 0.0 0.4025 0.475 MIX 4 2 1 SPLITR 2 1 ;
::: CX := GEO: CARCEL 2
    MESHX 0.0 1.265 MESHY 0.0 1.265 SPLITR 8 1
    RADIUS 0.0 0.4025 0.475 MIX 6 2 1 ;

```

;

Cell CX is the fuel rod we wish to model, SF97-4. Recall that we have to define a unique mixture (here, 6) as well as a unique cell to extract useful data from a particular rod. We have chosen a high radial splitting to ensure that self-shielding effects are taken into account.

Notice that each cell definition as well as the overall GEO: declaration must end with a semicolon.

A.7 Tracking

We now specify the tracking parameters.

```
DISCR Track := EXCEL: ASSMB ::  
TRAK TISO 10 12.0 ;
```

The variable DISCR will contain the output of the EXCEL: module, and the file Track will contain a record of Tracking parameters for later debugging. It can be omitted if desired. The tracking module requires at the very minimum one argument, which is a GEO: object. The TRAK TISO command tells DRAGON to use isotropic reflection at any boundaries in the assembly. The first value after TISO is the angular quadrature parameter, and the final value is the integration line density. To understand these, we can imagine that the tracking module replaces our reactor geometry with sets of lines. These lines are all parallel with one another, and have a density specified in inverse centimeters. These lines represent the paths of neutrons through the assembly, and using the mixture information from the geometry definition, DRAGON can determine which materials a given neutron on a certain path will interact with. We can also take our set of lines and rotate through some fixed angle and repeat this process. In this way, we can cover the entire assembly with neutron paths which will later be used in calculating collision probabilities and neutron fluxes. The fixed angle is the angular quadrature parameter, and means that in this case, the tracking module must generate 10 sets of lines (each undergoing successive rotations

of $360 / 10 = 36^\circ$), and their density is 12 lines per cm. Increasing either of these parameters will enable a more detailed and accurate simulation, at the cost of longer running times.

We can see here an instance of DRAGON's modularity in action. Had we decided to use one of the many other tracking modules in DRAGON, only the above code would have to change.

A.8 Self-shielding, Collision Probabilities, and Flux

SHI: is the self-shielding module used in DRAGON version 3.

```
LIBRARY := SHI: LIBRARY DISCR Track :: LEVE 1 ;
```

DRAGON version 4 has a more sophisticated module for self-shielding, USS: (for universal self-shielding), however, for the Takahama-3 simulation of SF97, the SHI: module was found to be sufficient. It modifies the cross section library; this is represented in DRAGON by assigning the results of applying SHI: to LIBRARY and storing the result back into LIBRARY. The LEVE 1 option allows the different self-shielding indices from the LIB: module.

```
CP := ASM: LIBRARY DISCR Track ;
```

The ASM: module calculates collision probabilities, and takes a cross section library and tracking parameters as arguments.

```
CALC := FLU: CP LIBRARY DISCR :: TYPE K ;
```

The FLU: module takes the collision probabilities from the previous step and uses them, along with the tracking and libraries, to compute the neutron flux. The TYPE keyword here takes the value of K, implying that K_{eff} is the eigenvalue to be solved for in the multigroup neutron transport equation. The evolution of K_{eff} is a useful cross-check in cases where this information is available.

A.9 Fuel Depletion

The EVO: module evolves the fuel concentrations in time.

```
BURNUP LIBRARY := EVO: LIBRARY CALC DISCR ::  
  EDIT -2 DEPL 7.17118E-07 DAY  
  POWR <<Power>> ;
```

The last module that we will consider is the EVO: module, which evolves the fuel inventories in time. It requires the current value of the neutron flux (CALC), the tracking (DISCR) and the current values of the component inventories (LIBRARY). The LIBRARY variable, and all of the mixtures that it contains, is evolved for a certain length of time. The POWR keyword indicates that the fuel evolution will be done at a constant power. The brackets are CLE-2000 syntax for interpolating a variable's value. The value of the POWR keyword must be the *specific power*, which is given in units of power per initial mass of heavy metal. The DEPL keyword requires the length of time required for evolution, in this case specified in days. The EDIT -2 directive is unique to the author's code; it informs DRAGON that fission rate calculations are to be performed and output.

```
NewBurnFile := BURNUP ;  
END: ;  
QUIT "LIST" .
```

After the fuel evolution, the details of the evolution can be output in a file labeled NewBurnFile, a user-declared variable. This can then be passed onto subsequent calculations, and illustrates how to control output from DRAGON.

A.10 Modifications for Fission Rates

The modifications here refer to DRAGON version 3.06H and were suggested by the principal code author, Guy Marleau. The code changes involve the files EVODRV.f and EVOSIG.f. Here, we only discuss the change in EVOSIG.f since the changes in EVODRV.f only generate a new parameter in the fuel evolution module, EVO:. In

the source file EVOSIG.f, one can take the microscopic reaction rates (the rate per atom). for fissions for a particular isotope and multiply this by the number of atoms of this isotope to get the macroscopic fission rates:

$$f_i(t) = N_i(t)R_i(t) = \rho_i(t)VR_i(t) \quad (\text{A.1})$$

Here, $\rho_i(t)$ is the number density of the i th fissioning isotope, V is the volume of the reactor element, and $R_i(t)$ is the microscopic reaction rate. The corresponding lines in EVOSIG.f are:

```
*-----
*  Print microscopic and total fission rate
*-----

      IF (IMPX .LE. -2) THEN
        WRITE(IOUT,6000)
        DO ICMB=1,NCOMB
          IBM=MILVO(ICMB)
          WRITE(IOUT,6001) IBM
          DO IST=1,NVAR
            LFISS=.FALSE.
            DO IFIS=1,NFISS
              LFISS=LFISS.OR.(KFISS(IFIS).EQ.IST)
            ENDDO
            IF (LFISS) THEN
              K=JM(IBM,IST)
              IF (K.GT.0) THEN
                IS=IST
                FACT=DEN(K)*VX(IBM)
                IF (INR.NE.0) THEN
                  WRITE(HNAMIS,'(2A4)') (ISONAM(I0,K),I0=1,2)
                  WRITE(IOUT,6002) HNAMIS,SIG(IS,1,IBM)*1.E-8,
```

```
>                                     SIG ( IS , 1 , IBM ) * FACT * 1.0 E16
                                     ENDIF
                                     ENDIF
                                     ENDIF
                                     ENDDO
                                     ENDDO
                                     ENDIF
                                     RETURN
```

This snippet adds a new option to EVO: that will calculate the fission rates if the input parameter is -2. The full code changes can be found on our DSpace archive.

[104]

Appendix B

Using Antineutrinos For Nuclear Nonproliferation

Neutrinos carry no charge, have little if any mass, and have practically no observable effects. Their range in matter is so great that their energy cannot be utilized. They have no present practical importance.

–Nuclear Chemical Engineering[110], 1981 edition

As mentioned in Chapter 1, the history of the neutrino and that of the nuclear reactor are intertwined. In this appendix, we discuss performing neutrino spectroscopy on nuclear reactors, a non-invasive technique that allows us to observe changes in reactor fuel composition by detecting the antineutrinos released from the fission process. The focus here will be upon the use of reactor simulations to aid with neutrino spectroscopy. We begin with a discussion of the SONGS1 experiment[24] which provided a clear observation of changes in antineutrino emission rate due to fuel evolution. We show results of DRAGON simulations used to model the core of the SONGS Unit 2 reactor. This exercise was particularly important in establishing that the modified DRAGON code could reproduce the burnup effect.

We then move to a discussion of using the Double Chooz far detector to further the goals of the IAEA Safeguards Regime. We produce three different sets of fission rates and pass them to the Double Chooz MC. The simulated detected spectra are

then subjected to a Kolmogorov-Smirnov (K-S) test to judge to which degree the scenarios are distinguishable.

B.1 Neutrino Spectroscopy with Reactors

The goals of those who seek nuclear nonproliferation are best summarized in the IAEA Nonproliferation Treaty (NPT)[111]. The document specifies as a goal, among many others,

to prevent diversion of nuclear energy from peaceful uses to nuclear weapons or other nuclear explosive devices.

The question of how to balance a nation's peaceful use of nuclear power with the concomitant threat of nuclear proliferation is an important one, but as concerned scientists, our effort is focused not on diplomacy, but on providing tools that can prevent the dispersal of nuclear weapons as well as enable monitoring of existing nuclear material. We further confine our attention to the monitoring of fissionable material from nuclear reactors. Typical methods for monitoring the fuel in a reactor are invasive and not-real time. They involve waiting until the core shutdown to invite inspectors to examine tags and seals on fuel assemblies. They may also include video surveillance of spent fuel or even counting of fuel rods in the fuel assemblies[112]. In addition, these methods do not directly measure the fuel[24].

In light of these indirect methods of monitoring the fuel, reactor antineutrinos offer an alternative approach. In each fission, approximately 5% of the ≈ 200 MeV of energy released is carried away by electron antineutrinos[82]. These antineutrinos are emitted isotropically and pass through the reactor containment without attenuation. Although the energy taken away by antineutrinos is unrecoverable for nuclear reactors, the energy spectrum of these antineutrinos is still useful. As shown in Figure B-1, antineutrinos emitted from fission products of ^{235}U have a different energy spectrum from those from ^{239}Pu . As the reactor fuel composition changes, we would expect to see a spectral distortion due to the relative amounts of uranium and plutonium in

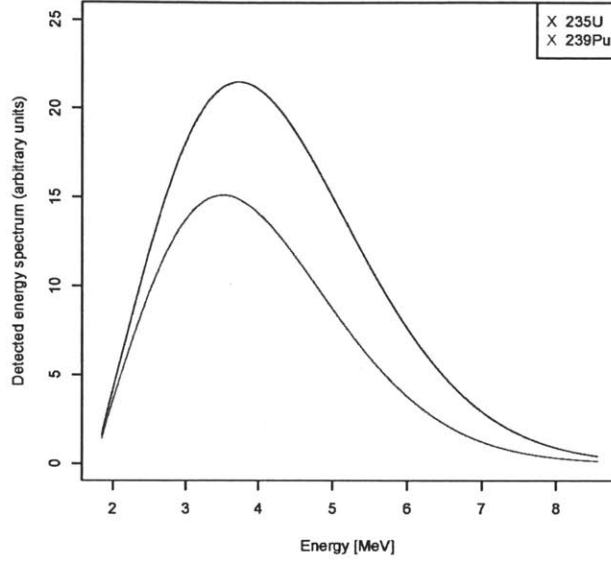


Figure B-1: Energy spectrum of detected reactor antineutrinos.

the core; this is called the burnup effect. In fact, the emitted antineutrino rate from a reactor is given by

$$\frac{dN_\nu}{dt} = \sum_k f_k(t) \int_{E_{th}}^{10} \sigma_{IBD}(E_\nu) S_k(E_\nu) dE \quad (\text{B.1})$$

Here, the threshold energy E_{th} for inverse beta decay is 1.806 MeV (the upper limit of 10 MeV is sufficient since very few reactor antineutrinos have energies above this value), the S_k are the neutrino energy spectra for the k th isotope, and the f_k are the instantaneous fission rate for the k th isotope. Thus, an accurate determination of the fission rates f_k are required to measure the antineutrino rate. However, as will be elaborated in the following section, it is possible to do a relative measurement by comparing the rates to, for example, their initial value.

The method outlined above is the essence of neutrino spectroscopy. One particular advantage of this method is that it does not require that the reactor be shut down in order to monitor the fuel evolution; in fact, since antineutrinos are being continually

emitted from the reactor core, this method allows for a non-invasive real-time monitor of the core. This method was first suggested in the 1970s by Mikaelyan[113], and much of the recent work in the field been both theoretical[114] and experimental[24, 112, 115]. We now turn to SONGS1, a recent experiment carried out by Lawrence Livermore National Laboratory (LLNL) and Sandia National Laboratory (SNL).

B.2 Close Range Core Monitoring With SONGS1

B.2.1 SONGS: Reactor and Detector

The San Onofre Nuclear Generating Station, or SONGS, is the name of both a nuclear power plant as well as an antineutrino experiment. Of the two reactors at the power plant, only one (Unit 2) was used in the experiment. Like the Takahama-3 reactor and the Chooz B1 and B2 reactors, SONGS Unit 2 is a PWR. It contains 217 fuel assemblies for a total power output of 3.4 GWth. The fuel assembly is a 16×16 design; 236 of the 256 rods are fuel rods, while the remaining space in the assembly is used for control rods. See Figures B-2 and B-3 for details of the core layout. We now move to a description of the SONGS1 detector.

The SONGS experiment[32] sought to observe changes in reactor fuel composition through examining changes in the emitted antineutrino flux. In particular, the immediate goal was to make measurement of the antineutrino rate. The ultimate goal of this type of experiment would be to observation fuel evolution from a detector far from the reactor ($O(100 \text{ km})$); however, to illustrate the proof of concept, the SONGS1 antineutrino detector was placed 24.5 m from the Unit 2 reactor core in the reactor tendon gallery (see Figure B-4), which contained steel tendons used for adjusting and inspecting steel tendons used to support the reactor containment[24]. The detector was 149 m from the Unit 3 reactor, and so it was estimated[32] that 97% of the detected antineutrinos would be from the closer Unit 2. The advantages to this location include the fact that it was outside of the containment region yet close enough to the core to see a large antineutrino flux. Also, the detector would not

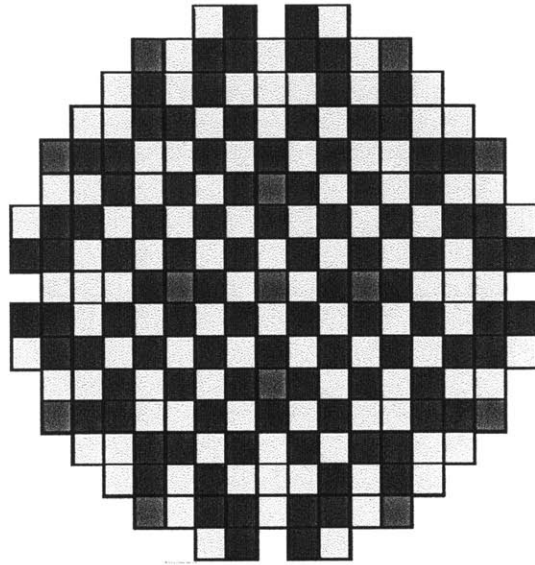


Figure B-2: SONGS Unit 2 core map. Each square is a fuel assembly. The blue fuel is fresh, the yellow fuel has passed through one fuel cycle, and the red fuel has been through two fuel cycles. Taken from [23].

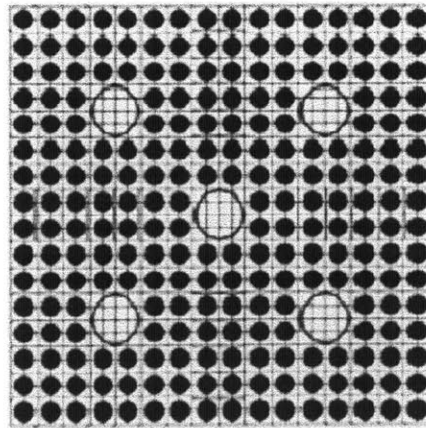


Figure B-3: SONGS Unit 2 assembly. This is a CE design. Taken from [23].

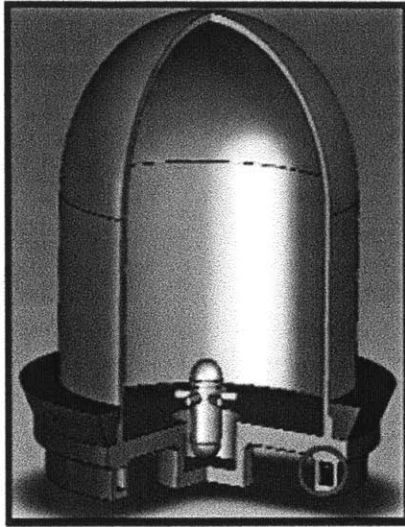


Figure B-4: The SONGS detector location in the core. The red circle locates the detector in the reactor tendon gallery. Taken from [23].

interfere with daily operations and maintenance of the reactor and would not need maintenance itself for months at a time[32].

A schematic of the detector appears in Figure B-5. Like Double Chooz and other reactor antineutrino detectors, SONGS1 used a Gd-doped liquid scintillator from the Palo Verde experiment[32, 3] to detect antineutrinos through a prompt positron annihilation event along with a delayed neutron capture event. The detector is more compact than Double Chooz, containing only 0.64 ton of scintillator. The inner target is divided into four cells, each containing the doped scintillator along with 2 PMTs. The target is surrounded by a passive polyethylene shielding to reduce neutron flux and gamma rays[32]. Surrounding the shielding is a set of plastic scintillator muon veto paddles. As the detector is 10 m below the surface, the cosmic muon flux was reduced by a factor of 7. As the goal of SONGS1 was to observe changes in the antineutrino rate due to fuel depletion and reloading, a relative measurement of the rate could be performed, given that the detector response was stable in time[32]. Indeed, due to difficulties in measuring the detector volume, the detection efficiency is only known to the 10% level, making an absolute measurement out of the question.

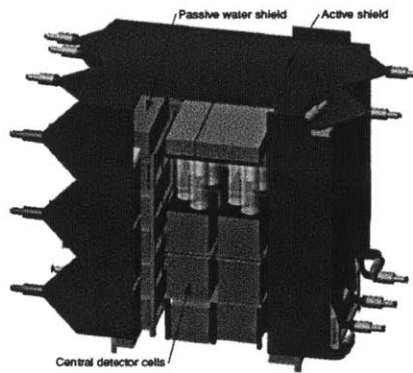


Figure B-5: The SONGS1 antineutrino detector. Taken from [23].

The total detection efficiency for antineutrinos was given as $10.7 \pm 1.5\%$ [24].

B.2.2 Data Analysis and Results

The experiment took data between June 2005 and November 2006. What follows is a description of the antineutrino event selection[24]. Each of the four cells was treated as an individual detector; each cell had to measure energies above a prompt and delayed energy threshold, and simultaneous energy depositions in neighboring cells are not taken into account[32]. Prompt events must be in the range of (2.39, 9) MeV while delayed events are in the range (3.5, 10) MeV. For each of the four cells in the detector, there was a cut placed that rejected events that had an uneven light distribution between the 2 PMTs in the cell. The experiment did not distinguish between prompt-delayed pairs that were actually antineutrino events and from correlated backgrounds that mimicked the signal; instead, an interevent time spectrum was created. In Figure B-6, we can see this spectrum plotted for all correlated events that satisfied the above criteria. The steeper exponential has a time constant of $\approx 28\mu\text{s}$, consistent with neutrons capturing on Gd [24].

In Figure B-7, we see SONGS1's evidence for a change in the antineutrino rate due to two sources: the evolution of the fuel itself causing a gradual decrease in the rate (a so-called "slope" change) and a much more dramatic change due to fuel reloading (a "step" change). The detector saw evidence for a change in antineutrino

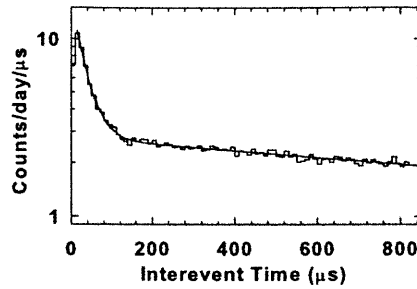


Figure B-6: A sample interevent spectrum from SONGS1. Taken from [24].

rate due to the removal of 250 kg of plutonium and the addition of 1.5 tons of uranium after the shutdown period[24]. The figure also shows a predicted rate using the ORIGEN/SCALE[116, 117] simulation package. The code was able to predict the slope but required a one-parameter fit to match the data. We show in the next section the use of the DRAGON code to do a similar fit as another way of verifying the use of the modifications made to the code to produce fission rates. SONGS1 provided us with a way to predict “slope” information while the Takahama benchmark provided us with a way to test absolute predictions (see Chapter 4).

B.2.3 Fission Rate Prediction from DRAGON

Southern California Electric (SCE), the power company that operates the SONGS reactor, provided us with the output of their reactor simulations that used the code SIMULATE-3[118]. This code is used for safety calculations as well as to provide an inventory prediction. The DRAGON code only simulates fuel assemblies, and so a full-core simulation with this code is not possible since it would treat each fuel assembly independently. However, in an approximation to a full-core calculation, we can perform a pseudo-core simulation with DRAGON if we supplement the simulation with extra information. The SIMULATE-3 calculation provides this information[71]. From SIMULATE-3, a factor was derived that weights each assembly by its power output. Thus, the outputs of the SIMULATE-3 code were used as inputs to DRAGON to predict the overall fission rates of the core, and ultimately, the antineutrino flux.

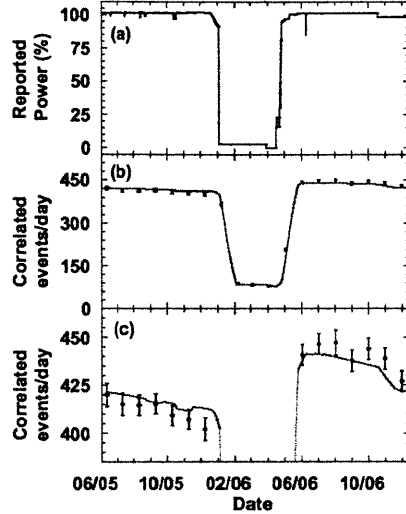


Figure B-7: Observation of antineutrino changes due to fuel evolution and reloading. The top frame shows the Unit 2 thermal power; the middle frame shows a clear tracking of the antineutrino rate; the bottom frame shows a zoom-in to the middle frame to make the change more clearly visible. Taken from [24].

A summary of the inputs used in this simulation are shown in Table B.2. The initial fuel loadings were taken from the proprietary SIMULATE-3 outputs. A 2% error on the thermal power was assumed. 650 days of reactor evolution were simulated. The total fission rate prediction is a sum of each fission rate in each fuel assembly. The fission rates obtained are shown in Figure B-9. As a cross-check, we compute the computed thermal power from DRAGON; this is shown in Figure B-8. The “reconstructed” thermal power is defined as $P_{th} = \sum_k f_k E_k$. The energies per fission E_k are shown in Table B.1, and only the isotopes ^{235}U , ^{238}U , ^{239}Pu , and ^{241}Pu . The slight decrease shown in the curve is due to production of other actinides that contribute less than 0.001% to the total power output.

To compute the detected antineutrino rate, we use equation B.1, with the additional parameters found in Table B.3. For the S_k , we use a parameterization provided by Vogel and Engel[33] whose values are shown in Table B.4, and for the inverse beta decay cross section, we use the parameterization given in [73]. The DRAGON prediction with data is shown in Figure B-10. A prediction was made for each cycle. To

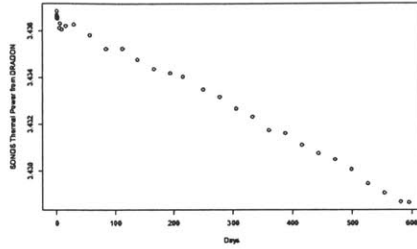


Figure B-8: DRAGON prediction of SONGS thermal power.

Isotope	Value
^{235}U	202.63 MeV
^{238}U	212.17 MeV
^{239}Pu	211.43 MeV
^{241}Pu	213.99 MeV

Table B.1: Energy released per fission used by the DRAGON code, from [31].

Input	Value	Source
Fuel density	10.412 g/cc	[119]
Cell pitch	1.285 cm	[71]
Pellet radius	0.4134 cm	[71]
Helium gap radius	0.422 cm	[71]
ZR-4 cladding	$\rho = 6.56$ g/cc	[120]
Cladding radius	0.485 cm	[71]
Average moderator temperature	578.19 K	Average of inlet and outlet temperatures
Average boron loading	600 ppm	Estimate
Fuel rod height	381 cm	[71]

Table B.2: SONGS simulations for DRAGON.

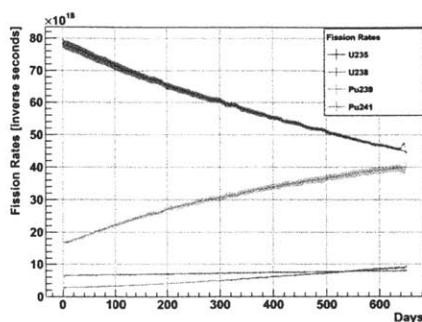


Figure B-9: DRAGON fission rate prediction for SONGS.

Input	Value
Detection efficiency	$10.7\% \pm 1\%$
Distance to reactor	24.5 ± 1.0 m
Number of target protons	4.35×10^{28}

Table B.3: Detector parameters for the SONGS antineutrino flux prediction. Taken from [32].

avoid cluttering the figure, only the Cycle 13 prediction is shown because the predictions are very similar. The data from SONGS1 was monthly-averaged and plotted. The data taking began during the second half of Cycle 12 (data on the right-side of the graph) and continued through the first half of Cycle 13 (set of data on the left side of the graph). Thus, the time axis recorded the number of days into the current fuel cycle. The good agreement between the DRAGON prediction and the data gave us confidence that the fission rate modifications were sufficient to predict the burnup effect. Together with the Takahama benchmark from Chapter 4, we can conclude that DRAGON is certainly adequate to compute fission rates at the assembly level, and given supplementary information, it can go beyond this. Now we turn to another nonproliferation exercise, one that focuses on the abilities of the Double Chooz MC.

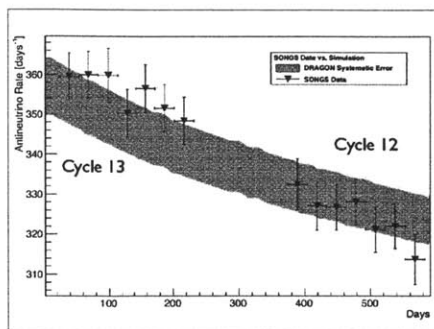


Figure B-10: DRAGON rate prediction with SONGS1 data. The time axis shows the number of days into the current fuel cycle.

Isotope	a_0	a_1	a_2
^{235}U	0.870	-0.160	-0.0910
^{238}U	0.976	-0.162	-0.0790
^{239}Pu	0.896	-0.239	-0.0981
^{241}Pu	0.793	-0.080	-0.1085

Table B.4: Fit parameters for the S_k , taken from [33].

B.3 Using the Double Chooz Far Detector for Non-proliferation

In the previous section, we detailed the use of a liquid scintillator-based antineutrino detector in performing a real-time non-invasive assay of a reactor core. We now discuss the similar use of the Double Chooz far detector (FD) for this purpose. The FD is 1.05 km from the two reactors, but we will generate a high-statistics MC sample to simulate a much closer detector on par with that of the SONGS detector. In addition, we take advantage of spectral measurements that can be performed with the FD. We outline three illicit production scenarios that can simulate increased production of plutonium while keeping the total reactor power output constant. We will demonstrate the degree to which these modified spectra can be distinguished from a baseline case.

B.3.1 Illicit Production Scenarios

For this simulation, a 2.7 GWth reactor was used, similar to the Takahama-3 reactor presented in Chapter 4. The core contained 205 fuel assemblies, each having a 17×17 design. A comparison of the SONGS detector and the Double Chooz Far Detector appears in Table B.5. We used the power evolution and inferred fuel loading of the Chooz B2 reactor during its Cycle 12, which began in November 2010 and continued through September 2011. We examined three scenarios: a baseline scenario, a “steel scenario” where the water in the water channels in each fuel assembly was replaced with SS304, and a “B4C” scenario where the water is replaced with B4C (boron carbide). Since it would be difficult to replace each fuel assembly’s water channels with SS304 or B4C, these simulations are not practical in an actual reactor since such modification would invite suspicion. However, the scenarios are included in order to study the extreme effects on the detected energy spectrum, and to perform essentially a sensitivity study around the baseline scenario. As shown in Figure B-11, these changes will tend to suppress the thermal neutron flux in the reactor while increasing the epithermal flux that causes neutron capture on ^{238}U and thus production of plutonium.

The same initial fuel loading of 116 T is used for all three simulations, and all three scenarios are evolved with the same reactor thermal power history, focusing on a month-long period from day 175 of Cycle 12 to day 205. Thus, as shown in Figure B-12, the total fission rate for each scenario is the same, removing the possibility of looking at power fluctuations to discover the illicit production. However, the fission rates of the individual fuel isotopes are shown in Figures B-13, B-14, B-15, and B-16. In these, we can see the effect of the different scenario choices on the fission rates. As expected, the ^{235}U fission rates are reduced due to the reduction of thermal flux, whereas the ^{238}U fission rates, which are caused by ~ 1 MeV neutrons, are increased. In Figures B-17, B-18, B-19, and B-20, we show the fuel inventories over this period for the three scenarios. The fuel inventories at the end of the simulation are shown in B.6. For the steel scenario, approximately 0.1 T of plutonium are produced over the

Detector	Scintillator Mass [T]	Baseline [m]	daily $\bar{\nu}_e$ Rate
SONGS	0.64	24.5	3800
Double Chooz Far Detector	8.2	1050	42

Table B.5: Comparison of SONGS and Double Chooz Far Detector.

Scenario	M_{235}	M_{238}	M_{239}	M_{241}
Base	2.361	112.2	0.601	0.095
SS304	2.417	112.1	0.695	0.109
B4C	2.615	111.5	1.076	0.130

Table B.6: Fuel inventories at end of simulation for each scenario, in metric tons.

baseline case, whereas for the B4C case, nearly 0.51 T is produced over the baseline case.

B.3.2 Double Chooz Detector Monte Carlo

The relevant features of the Double Chooz Monte Carlo (DCMC) employed in this exercise were outlined in Chapter 2. After the three sets of fission rates were generated with DRAGON, they were passed to DCRxtrTools (see Chapter 5), where the unoscillated antineutrino flux is output for each run in the interval that the fission rates were generated. The simulations were performed at 1000x statistics; since the FD is 1.05 km from the reactors, this high-statistics sample is equivalent to having the FD be a distance of approximately 33 m from the simulated reactor. This is comparable with the 24.5 m baseline for the SONGS experiment presented in the previous section. The selection criteria are the same as those used for the first publication, and have already been outlined in Chapter 6. In particular, the energy-dependent and z-axis-dependent calibration corrections have been applied.

B.3.3 Non-observation of the Burnup Effect

Even though we are studying the use of spectral measurements in this section, it is important to investigate whether or not we see a shift in the overall normalization

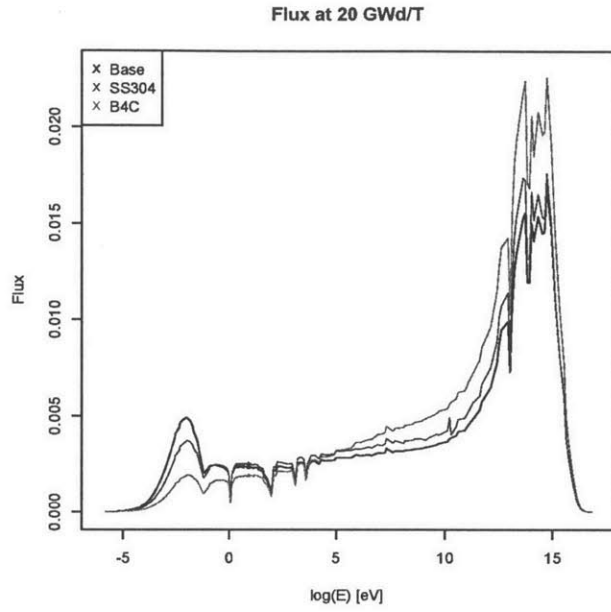


Figure B-11: Neutron flux for the three scenarios.

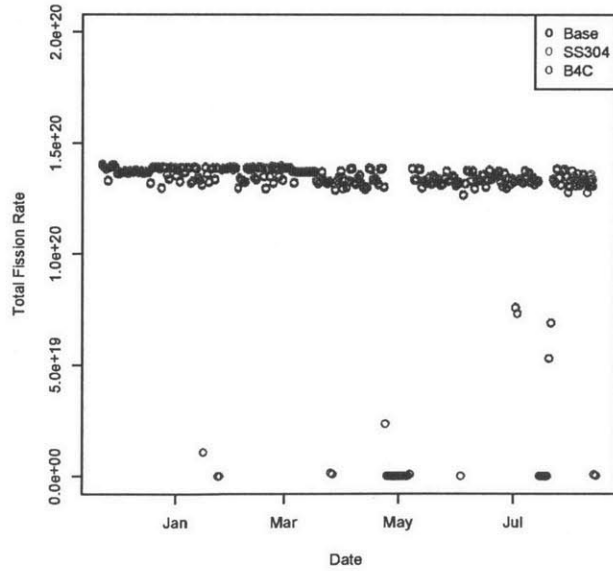


Figure B-12: Total fission rate for the three scenarios.

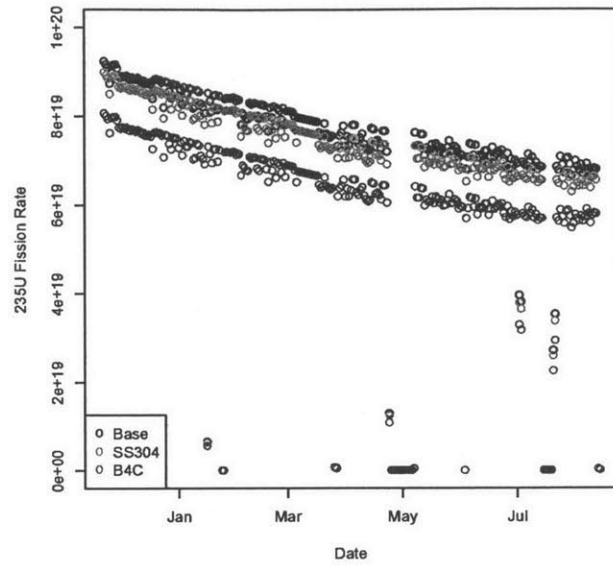


Figure B-13: ^{235}U fission rate for the three scenarios.

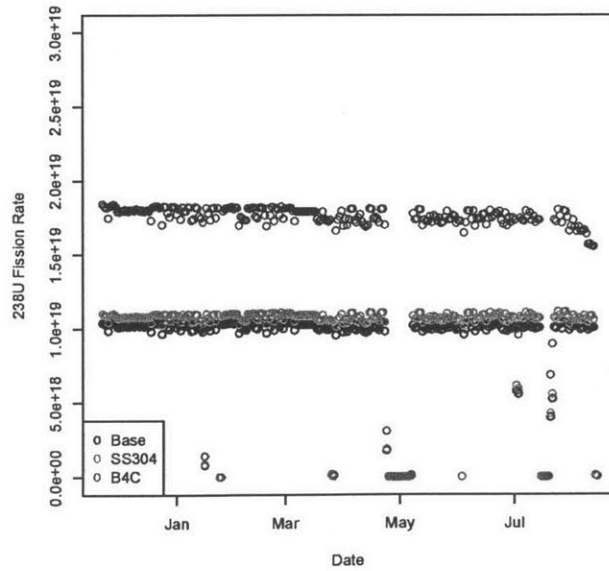


Figure B-14: ^{238}U fission rate for the three scenarios.

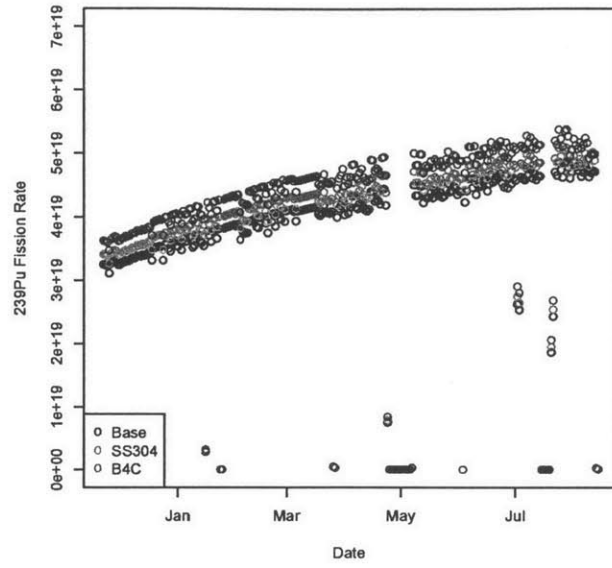


Figure B-15: ^{239}Pu fission rate for the three scenarios.

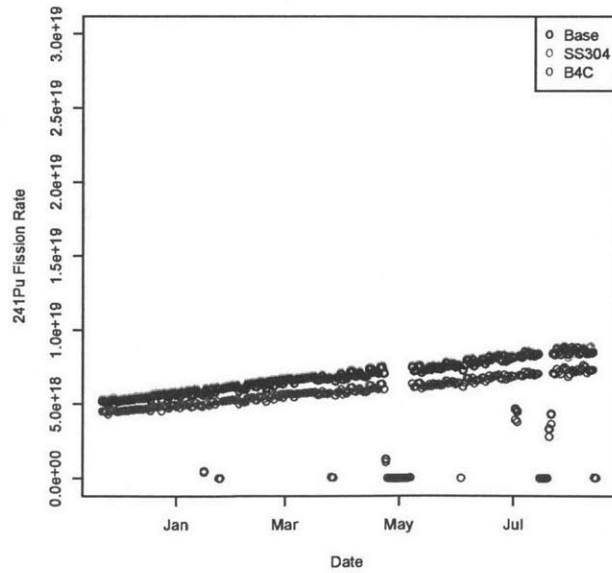


Figure B-16: ^{241}Pu fission rate for the three scenarios.

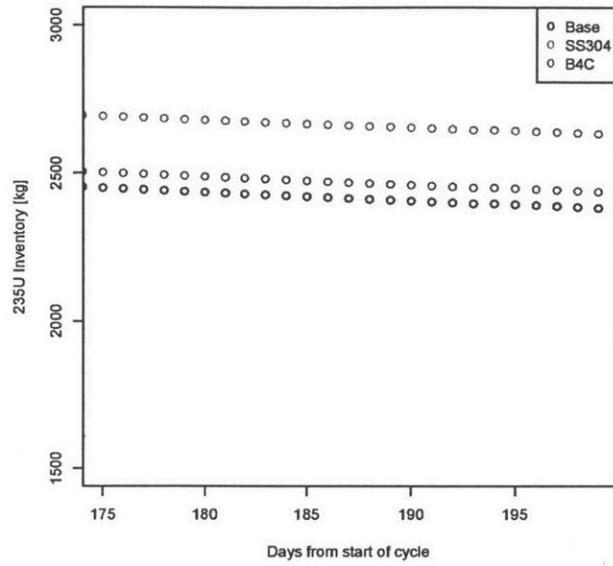


Figure B-17: ^{235}U inventory for the three scenarios.

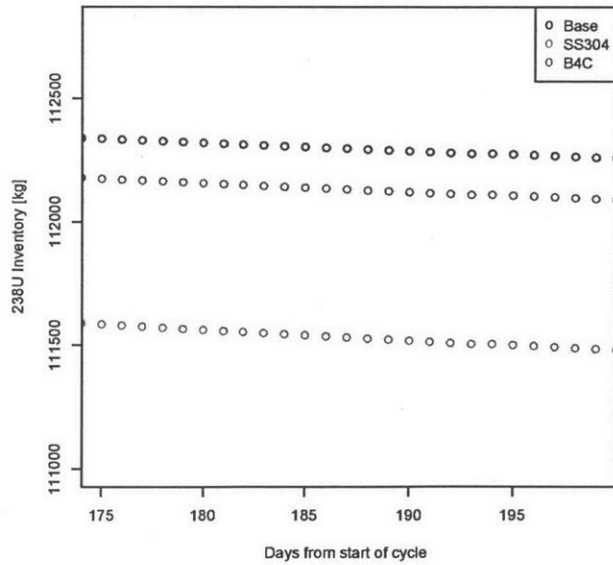


Figure B-18: ^{238}U inventory for the three scenarios.

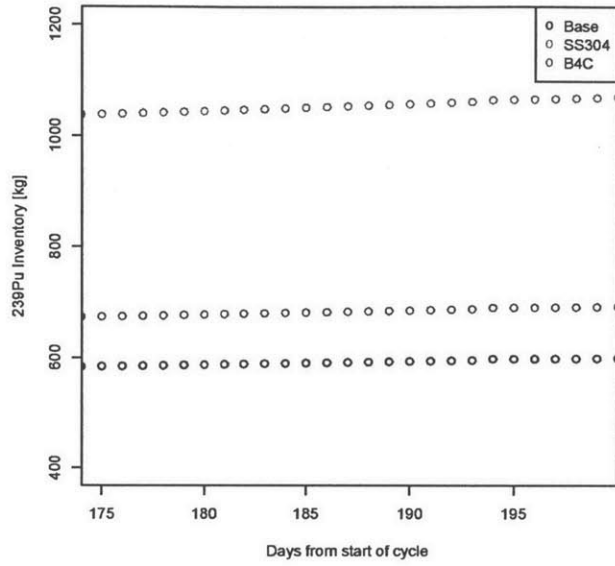


Figure B-19: ^{239}Pu inventory for the three scenarios.

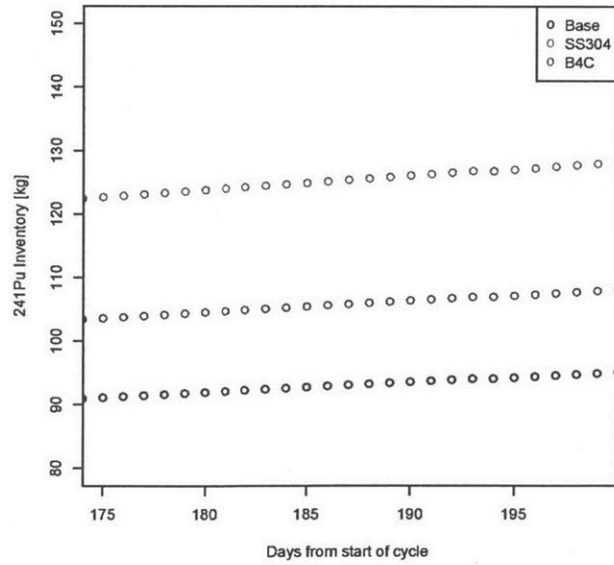


Figure B-20: ^{241}Pu inventory for the three scenarios.

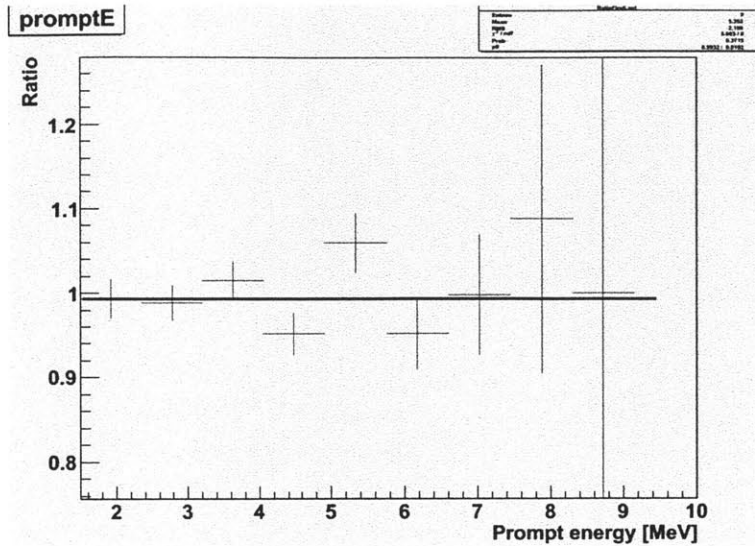


Figure B-21: Comparison of two spectra separated by 1 month.

of the spectra due to the burnup effect. Two prompt spectra were simulated for 17 hours and 20,000 events each in the base scenario separated by a month in time. In Figure B-21, we show the ratio of the first prompt spectrum to the later prompt spectra. In the figure, a best fit constant line shows that the shift is 0.993185 ± 0.01 , which is consistent with unity and thus no observation of the burnup effect.

B.3.4 Inference of Diverted Plutonium

With the fission rates from DRAGON generated, we can examine the feasibility of distinguishing diverted spectra from the different scenarios as reported above. In this section, we explore the effects of the two scenarios on the prompt energy spectra as well as the possibility of a systematic drift in the detector energy scale on the results. We also examine systematic shifts of $\pm 1\%$. For each of the three scenarios, 515 Double Chooz runs were simulated, corresponding to 29.6 days of data from day 175 to 205. Nearly 510,000 antineutrino events were produced.

In Figure B-22 we show the three spectra. The error bars are difficult to see in the figure; since the 510,000 events are placed into 9 bins, the error per bin is approximately $1/\sqrt{510,000/9} = 0.42\%$. We perform a Kolmogorov-Smirnov (K-S)

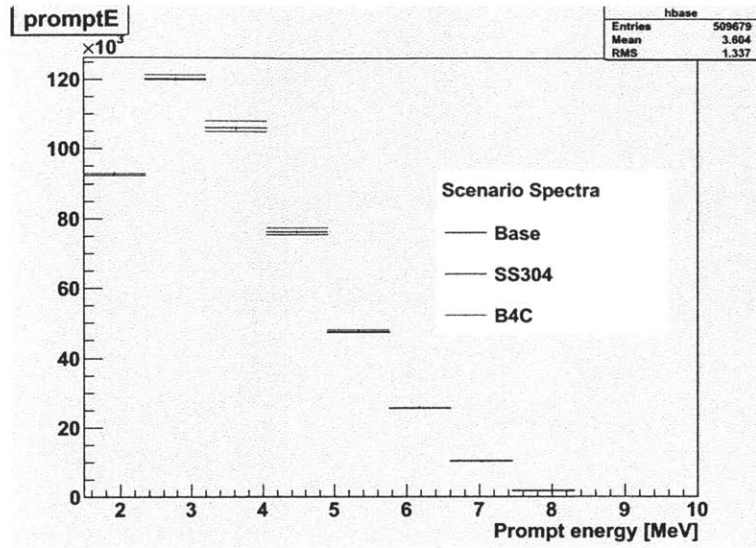


Figure B-22: Scenario spectra.

test to evaluate the distinction between the pairs of scenarios. For the baseline-to-steel distinction, the test should yield a high probability, meaning that the two spectra could in fact be drawn from the same sample. Indeed, the ROOT K-S test yields 48%. For the baseline-to-B4C case, the test yields a probability of 0.3%, meaning that the two spectra are certainly distinct.

However, with a spectral measurement, we must consider the detector energy scale. To accomplish this, for each event in the baseline scenario, we scale the prompt energy by $\pm 1\%$, creating a 1% systematic uncertainty band as shown in Figure B-23. In the figure, we see that most of the spectra are contained within the band. Thus, it is difficult to distinguish a change in spectrum due to fuel diversion from the uncertainty of the energy scale. We note here that the Double Chooz energy scale is known to 0.8%. We conclude that spectral information in this simple manner requires a detector with an energy scale uncertainty much better than 1%. However, it is possible that this simple approach could be more successful by combining this information with other sources. In addition, performing more simulations at later times in the fuel cycle, when the illicit production is maximized, may improve this test.

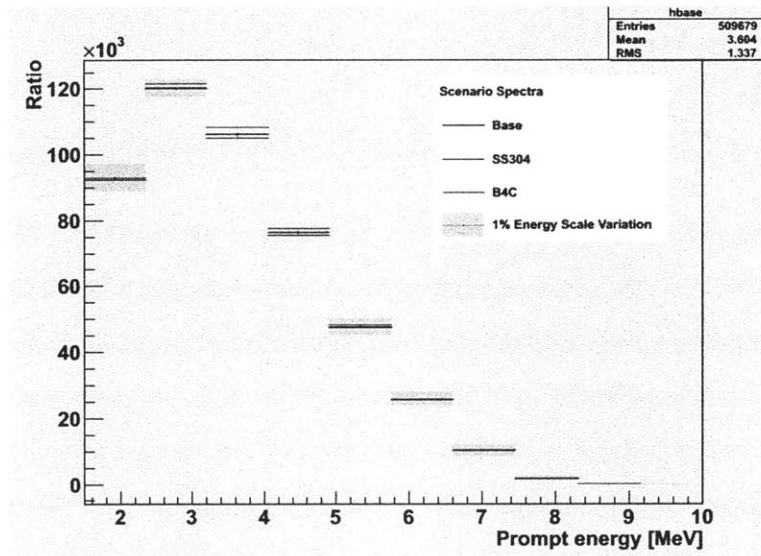


Figure B-23: Scenario spectra with 1% energy scale uncertainty band.

Appendix C

AFA3G Sensitivity Study With DRAGON

In this section, we show the results of the sensitivity study performed on the APOLLO AFA 3G comparison presented in Chapter 5. This study is similar to the one done for Takahama-3, except in the present case, it is comparing simulation to simulation (DRAGON to APOLLO). Both Chooz B1 and B2 contain 205 fuel assemblies. Of these, 204 of those in B1 and 200 of those in B2 are of the Areva-Framatone type AFA-3GL, and thus we can compute assembly-level fission rate errors based on the given parameters for this type. Analogous to the Takahama-3 simulation, we varied one parameter at a time and examine the corresponding effect on the fission rates. These parameters are shown beginning with Table C.1.

A large fraction of the assemblies contain Gd_2O_3 - UO_2 burnable absorber rods.

Parameter	Variation
Thermal Power	$\pm 0.7\%$
Fuel Temperature	± 200 K
Moderator Temperature	± 30 K
Moderator Density	$\pm 6\%$
Boron Concentration	$\pm 1.4\%$

Table C.1: Parameter variations for fission rates.

Since gadolinium has an extremely high thermal neutron capture cross section, its effect on the neutron flux in the assembly is non-negligible, and so we provide error tables for both Gd-loaded and non-Gd loaded tables.

For the AFA-3GL without Gd, the fission rate variations are shown in Figures C-1, C-2, C-3, C-4. Concrete values for a particular moment in time is listed in Table C.2. This table shows the fission rate variations taking place on day 362 of the simulation at a burnup of 14315 MWd/T.

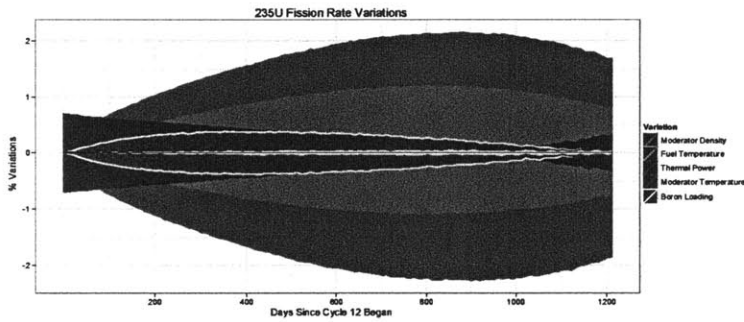


Figure C-1: Assembly-level sensitivity study of AFA 3G APOLLO simulation with DRAGON.

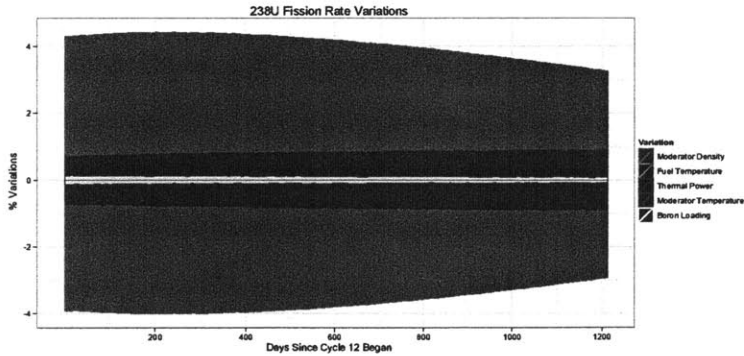


Figure C-2: Assembly-level sensitivity study of AFA 3G APOLLO simulation with DRAGON.

The first data-taking period extended from April 13, 2011 to September 18, 2011. For cores B1 and B2, Cycle 12 began on September 6, 2010 and November 22, 2010, respectively.

In the actual cores, the assemblies begin with a variety of fuel compositions based

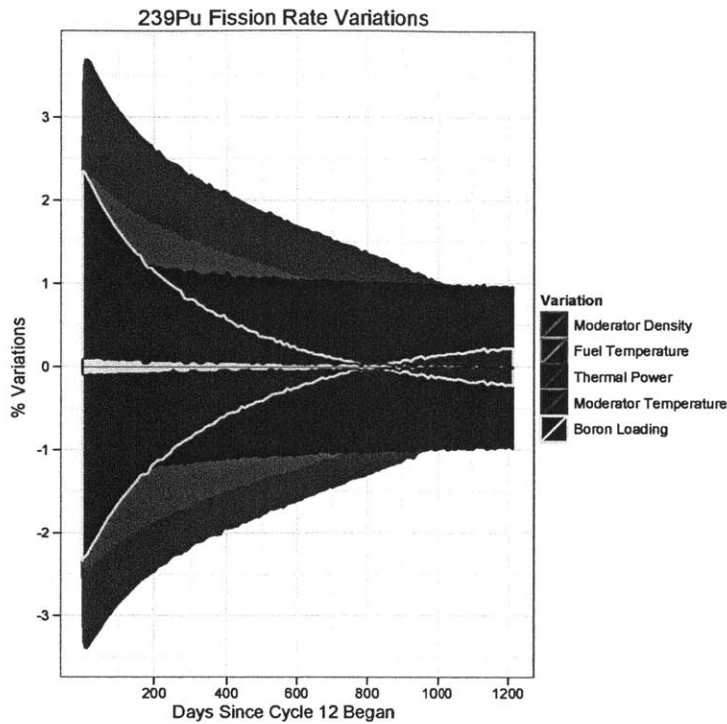


Figure C-3: Assembly-level sensitivity study of AFA 3G APOLLO simulation with DRAGON.

on the amount of irradiation they have received. The assemblies can be broadly categorized into 3 types: fresh fuel, once-burned (passed through one fuel cycle), and twice-burned (passed through the previous two cycles). For the purposes of illustration, we show the results for core B1. For B1, the total error at the beginning of the data-taking period are shown beginning with Table C.3. The contributions to the error were assumed to be independent in order to make a conservative estimate of the total error. It must be noted, however, that implicit in these calculations is the fact that DRAGON is a lattice code, and so these errors neglect the influence of neighboring fuel assemblies.

Regardless of the presence of Gd in the assembly, the moderator density provides the largest systematic uncertainty. This is not surprising given that the Chooz reactors are PWRs which require a high thermal neutron flux. A denser water moderator would thermalize neutrons more readily, increasing the fission rate for ^{235}U . Similar

Variation	²³⁵ U	²³⁸ U	²³⁹ Pu	²⁴¹ Pu
Mod.Temp +30 K	-0.375835	0.0593707	0.620594	2.0664
Mod.Temp -30 K	0.387647	-0.0499468	-0.650382	-2.10309
Fuel Temp. +200 K	-0.755965	0.495698	1.37524	1.70224
Fuel Temp. -200 K	0.823615	-0.535278	-1.52666	-1.93936
Boron +1.5%	-0.034362	0.118741	0.0347533	0.0762195
Boron -1.5%	0.0451002	-0.109317	-0.0620594	-0.0733966
Moderator Density +6%	1.4926	-3.95899	-2.03058	-2.49548
Moderator Density -6%	-1.58388	4.38401	2.1274	2.50113
Thermal Power +0.7%	0.452076	0.801975	1.10962	2.04664
Thermal Power -0.7%	-0.441338	-0.783127	-1.1121	-2.01276

Table C.2: AFA-3GL fission rate percent variations at day 362 of simulations (burnup = 14315 MWd/T)

Isotope	Uncertainty (4/13/2011)	Uncertainty (9/18/2011)
²³⁵ U	1.35%	1.77%
²³⁸ U	4.11%	4.07%
²³⁹ Pu	3.37%	2.76%
²⁴¹ Pu	5.75%	4.19%

Table C.3: Fresh fuel AFA-3GL errors: B1

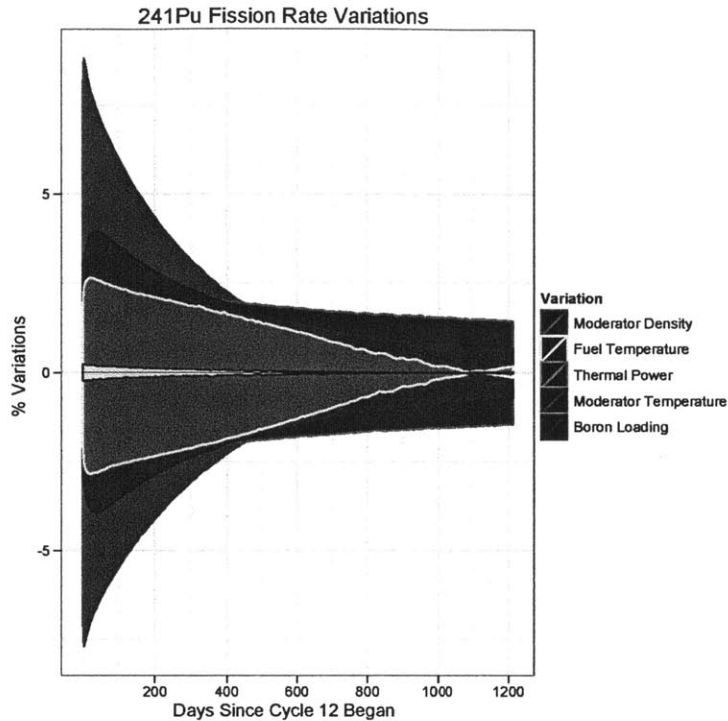


Figure C-4: Assembly-level sensitivity study of AFA 3G APOLLO simulation with DRAGON.

logic applies to the moderator temperature, which is completely correlated with its density. However, increasing the moderator temperature will decrease its density, since the water is kept at constant (15 MPa) pressure.

Since ^{238}U is only fissionable with neutrons in the MeV range, reducing the moderator density or temperature will only increase the flux of epithermal neutrons, increasing the ^{238}U fission rate. Since ^{239}Pu and ^{241}Pu are by-products of ^{238}U fissions, we can see that their deviations follow the same trend.

Increasing the fuel temperature gives more energy to neutrons in the fuel pin, which takes them from the thermal to the epithermal energy spectrum. By this argument, we can understand the decrease in ^{235}U fission rate, and consequent increase in the ^{238}U fission rate.

Since boron is a strong neutron poison in a reactor, increasing its concentration leads to a decrease in ^{235}U fission rates.

In examining the power variation, we must recall that whereas in simulation we set the thermal power, during actual reactor operation it is the lifting or lowering of control rods that results in a change in thermal power. Thus, we see that an increase in thermal power is associated with increases in all 4 types of fission rates, and vice versa.

Bibliography

- [1] K. Nakamura et al. Review of particle physics. *J. Phys.*, G37:075021, 2010.
- [2] M. Apollonio et al. Search for neutrino oscillations on a long base-line at the CHOOZ nuclear power station. *The European Physical Journal C*, 27:331 – 374, 2003.
- [3] F. Boehm et al. Final results from the palo verde neutrino oscillation experiment. *Phys. Rev. D*, 64:11, 2001.
- [4] Z. Wang. Daya bay neutrino experiment: Goal, progress and schedule. *Proceedings of the DPF 2011 Conference*, 2011.
- [5] F. Blasczyk. *T2K off-axis near detector flux measurement and absolute momentum scale calibration of the off-axis near detector tracker*. PhD dissertation, Institut de Recherche sur les lois Fondamentales de l'Univers (IRFU), 2011.
- [6] A. Sousa. Long baseline neutrino experiments. *Proceedings of the XXX. Physics in Collision*, 2011.
- [7] K. N. Abazajian et al. Light sterile neutrinos: A white paper, 2012.
- [8] B. Reinhold. *Development of a Level-1 Trigger and Timing System for the Double Chooz experiment*. PhD dissertation, RWTH Aachen, 2009.
- [9] W. Stacey. *Nuclear Reactor Physics*. Wiley-VCH, 2007.
- [10] M. Fallot, C. Jones, and A. Onillon. Reactor slides prepared for lownu 2011. Double Chooz Internal Document #3389.

- [11] United Cluster. United cluster final fit technote, 2011. Double Chooz Internal Document #3222.
- [12] F. Suekane. Standard light noise rejection. Double Chooz Internal Document #2835.
- [13] M. Toups, T. Matsubara, and P. Novella. Double chooz blessed plots, 2011. Double Chooz Internal Document #3386.
- [14] Second analysis comparison. Double Chooz Internal Document #3199.
- [15] C. Palomares, B. Reinhold, and M. Toups. Accidental background rate update. Double Chooz Internal Document #3511.
- [16] T. Mueller. Spill-in/out studies and other interesting stuff about neutron physics. Double Chooz Internal Document #3031.
- [17] P. Chang. Cf252 delayed spectra peak fitting. Double Chooz Internal Document #3209.
- [18] I. Ostrovskiy. Mc correction function: performance and error estimation. Double Chooz Internal Document #3270.
- [19] K. Abe et al. *Phys. Rev. L*, 107:041801, 2011.
- [20] P. Adamson et al. Improved search for muon-neutrino to electron-neutrino oscillations in minos. 2011.
- [21] F. P. An et al. Observation of electron-antineutrino disappearance at Daya Bay. 2012.
- [22] J. K. Ahn. Observation of reactor electron antineutrino disappearance in the reno experiment. 2012.
- [23] A. Misner. *Simulated Antineutrino Signatures of Nuclear Reactors for Nonproliferation Applications*. PhD dissertation, Oregon State University, 2008.

- [24] N. S. Bowden, A. Bernstein, S. Dazeley, R. Svoboda, A. Misner, and T. Palmer. Observation of the Isotopic Evolution of Pressurized Water Reactor Fuel Using an Antineutrino Detector. *J. Appl. Phys.*, 105:064902, 2009.
- [25] G. L. Fogli et al. Evidence of $\theta_{13} > 0$ from global neutrino data analysis. *Phys. Rev. D.*, 84:053007, 2011.
- [26] The SNO Collaboration. An independent measurement of the total active ^8b solar neutrino flux using an array of ^3he proportional counters at the sudbury neutrino observatory. *Phys. Rev. Lett.*, 92:181301, 2004.
- [27] F. Kaether. *Data Analysis of the solar neutrino experiment GALLEX*. PhD thesis, Heidelberg, 2007.
- [28] Borexino Collaboration. New results on solar neutrino fluxes from 192 days of borexino data. *Phys. Rev. Lett.*, 101:091302, 2008.
- [29] G. Mention et al. The Reactor Antineutrino Anomaly. 2011.
- [30] A. Franke, T. Lasserre, C. Mariani, G. Mention, I. Ostrovskiy, M. Shaevitz, M. Toups, and L. Winslow. Double chooz neutrino oscillation fit results. Double Chooz Internal Document #3519.
- [31] V. McLane et al. ENDF/B-VI Summary Documentation Supplement I ENDF/HE-V1 Summary Documentation, 1996.
- [32] N. S. Bowden et al. Experimental results from an antineutrino detector for cooperative monitoring of nuclear reactors. *Nucl. Instrum. Meth.*, A572:985–998, 2007.
- [33] P. Vogel and J. Engel. *Phys. Rev. D*, 39:3378, 1989.
- [34] S. Hatakeyama et al. *Phys. Rev. Lett.*, 81:2016–2019, 1998.
- [35] K. Eguchi et al. First results from kamland: Evidence for reactor antineutrino disappearance. *Phys. Rev. Lett.*, 90:021802, 2003.

- [36] The SNO Collaboration. Direct evidence for neutrino flavor transformation from neutral-current interactions in the sudbury neutrino observatory. *Phys. Rev. Lett.*, 89, 2002.
- [37] Z. Maki, M. Nakagawa, and S. Sakata. *Prog. Theor. Phys.*, 28:870, 1962.
- [38] B. Pontecorvo. *JETP*, 34:172, 1958.
- [39] B. Kayser. *Phys. Rev. D*, 24:110, 1981.
- [40] K. Zuber. *Neutrino Physics*. Taylor and Francis, 2003.
- [41] L. Wolfenstein. Neutrino oscillations in matter. *Phys. Rev. D.*, 17:2369, 1978.
- [42] B. Kayser, F. Gibrat-Debu, and F. Perrier. *Physics of Massive Neutrinos*. World Scientific Lecture Notes in Physics. World Scientific Pub Co Inc, 1989.
- [43] P. Vogel and F. Boehm. *Physics of Massive Neutrinos*. Cambridge University Press, 1992.
- [44] P. Huber, M. Lindner, M. Rolinec, T. Schwetz, and W. Winter. Prospects of accelerator and reactor neutrino oscillation experiments for the coming ten years. 2004.
- [45] J. M. Conrad. *Nucl. Phys. B Proceedings Supplement*, pages 1–6, 2010.
- [46] G. Drexlin et al. Katrin: Direct measurement of a sub-ev neutrino mass. *Nucl. Phys. B.*, 145, 2005.
- [47] F. Ardellier et al. Double Chooz: A search for the neutrino mixing angle θ_{13} . 2006.
- [48] Xinheng Guo et al. A precision measurement of the neutrino mixing angle θ_{13} using reactor antineutrinos at Daya Bay. 2007.
- [49] J. K. Ahn et al. RENO: An Experiment for Neutrino Oscillation Parameter θ_{13} Using Reactor Neutrinos at Yonggwang. 2010.

- [50] D. Ayres. Nova proposal to build a 30 kiloton off-axis detector to study neutrino oscillations in the fermilab numi beamline. 2005.
- [51] B. Ackhar et al. *Phys. Rev. B*, 243, 1996.
- [52] L. H. Miller. *The Palo Verde Neutrino Oscillation Experiment*. PhD thesis, Stanford University, 2000.
- [53] Reno: Reactor experiment for neutrino oscillation at yonggwang. *J. Phys.: Conf. Ser.*, 120:052025, 2008.
- [54] The MINOS Collaboration. *Phys. Rev. D*, 76:052003, 2007.
- [55] T. Lee. Overview of the t2k long baseline neutrino oscillation experiment. *Proceedings of the DPF 2009 Conference*.
- [56] H. Kwon et al. Search for neutrino oscillations at a fission reactor. *Phys. Rev. D.*, 24:1097–1111, 1981.
- [57] F. Von Feilitzsch, A. A. Hahn, and K. Schreckenbach. Experimental Beta Spectra from PU-239 and U-235 Thermal Neutron Fission Products and their Correlated Anti-neutrino spectra. *Phys. Lett.*, B118:162–166, 1982.
- [58] Y. Declais et al. Study of reactor antineutrino interaction with proton at bugey nuclear power plant. *Phys. Rev. B.*, 338:383–389, 1994.
- [59] G.S. Vidyakin et al. *JETP*, 93, 1987.
- [60] G.S. Vidyakin et al. *JETP Lett.*, 59, 194.
- [61] A. I. Afonin et al. A study of the reaction $\nu_e + p$ yields $e^+ + n$ in a nuclear reactor. *JETP*, 94:1–17, 1988.
- [62] G. Zacek et al. *Phys. Rev. D.*, page 2621, 1986.
- [63] Z. D. Greenwood et al. Results of a two position reactor neutrino oscillation experiment. *Phys. Rev. D.*, 53:6054–6064, 1996.

- [64] F. Reines, H. W. Sobel, and E. Pasierb. Evidence for neutrino instability. *Phys. Rev. Lett.*, 45:1307, 1980.
- [65] V. Kuvshinnikov et al. Precise measurement of the cross section for the reaction $\nu_e + p \rightarrow n + e^+$ at a reactor of the rovno nuclear power plant. *JETP*, 54, 1991.
- [66] Th. A. Mueller et al. Improved Predictions of Reactor Antineutrino Spectra. 2011.
- [67] Patrick Huber. On the determination of anti-neutrino spectra from nuclear reactors. 2012.
- [68] T. R. England, Wilson W. B., R. E. Schenter, and F. M. Mann. Summary of ENDF/B-V Data for Fission Products and Actinides. *EPRI NP-3787*, 1984.
- [69] M.A. Kellett et al. The JEFF-3.1/-3.1.1 radioactive decay data and fission yields sub-libraries, 2009.
- [70] A. Santamarina et al. The JEFF-3.1.1 Nuclear Data Library, 2009.
- [71] R. Chang. Private communication, 2010.
- [72] Z. Djurcic et al. Uncertainties in the Anti-neutrino Production at Nuclear Reactors. *J. Phys.*, G36:045002, 2009.
- [73] C. Bemporad, G. Gratta, and P. Vogel. Reactor-based Neutrino Oscillation Experiments. *Rev.Mod.Phys*, 74, 2002.
- [74] S. F. E. Tournu. Afnor xp x 07-020. 1996.
- [75] P. Vogel. Analysis of the antineutrino capture on protons. *Phys. Rev. D*, 29, 1984.
- [76] A. et al. Pichlmaier. Neutron lifetime measurement with the ucn trap-in-trap mambo-ii. *Phys. Lett. B*, 693:221 – 226, 2010.
- [77] Y. Abe et al. Indication for the disappearance of reactor $\bar{\nu}_e$ in the double chooz experiment. 2012.

- [78] G. Marleau, R. Roy, and A. Hébert. DRAGON: A Collision Probability Transport Code for Cell and Supercell Calculations. *Report IGE-157*, 1994.
- [79] O. Meplan et al. MURE: MCNP Utility for Reactor Evolution. *Proceedings of the int. conf. ENC 2005, Versailles*, 2005.
- [80] <http://neutrino.phys.ksu.edu/~GLG4sim/>, 2005.
- [81] A. Hébert. *Applied Reactor Physics*. Presses inter Polytechnique, 2009.
- [82] J. J. Duderstadt and L. J. Hamilton. *Nuclear Reactor Analysis*. Wiley Interscience, 1975.
- [83] R. Sanchez et al. Apollo ii: A user-oriented, portable, modular code for multi-group transport assembly calculations. *Nucl. Sci. Eng.*, 100:352, 1988.
- [84] J. Ragusa. Fuel assembly and 3-d core modeling and analysis. 2009.
- [85] Y. Nakahara et al. Technical Development on Burn-up Credit for Spent LWR Fuels. *ORNL/TR-2001/01*, 2001.
- [86] A. Franke. Event generation & uncertainty propagation in dcrxtrtools using the bugey4 anchor point, 2011. Double Chooz Internal Document #3221.
- [87] A. Franke. Dcrxtrtools user manual. Double Chooz Internal Document #2422.
- [88] T. Lasserre. Target h: preliminary analysis. Double Chooz Internal Document #2233.
- [89] J. Haser and C. Langbrandtner. Spill-in/out update. Double Chooz Internal Document #3445.
- [90] M. Ishitsuka, S. Lucht, J. Maeda, I. Ostrovskiy, F. Sato, and A. Stueken. Trigger efficiency task force report. Double Chooz Internal Document #3261.
- [91] P. Chang, T. Konno, I. Ostrovskiy, A. Remoto, D. Shrestha, M. Bergevin, J. Busenitz, and Z. Djurcic. Preliminary neutron efficiency note. Double Chooz Internal Document #3364.

- [92] A. Remoto. Energy containment studies. Double Chooz Internal Document #3299.
- [93] Igor Ostrovskiy. *Measuring the Neutrino Mixing Angle θ_{13} With the Double Chooz Far Detector*. PhD thesis, University of Alabama, Tuscaloosa, 2012.
- [94] M. Fallot and A. Onillon. First core fission rate error estimates. Double Chooz Internal Document #3277.
- [95] P. Novella. Expected vs. observed rate. Double Chooz Internal Document #3418, 2011.
- [96] M. Hartz. First oscillation results for the t2k experiment. 2012.
- [97] P. Adamson et al. *Phys. Rev. D.*, 82:051102, 2010.
- [98] M. Orchanian. *Proceedings of the DPF-2011 Conference*, 2011.
- [99] Anc: A westinghouse advanced nodal computing code, westinghouse report wcap-10965-p-a(p). 1986.
- [100] A. Hebert D. Sekki and R. Chambon. A user guide for donjon version4. 2011.
- [101] G. Marleau, A. Hebert, and R. Roy. A user guide for dragon version4. 2009.
- [102] <http://www.polymtl.ca/nucleaire/DRAGON/en/download/index.php>.
- [103] <http://gcc.gnu.org/fortran/>.
- [104] C. L. Jones and J. M. Conrad. Dragon 3.06h fission rate modifications with tutorial, 2012.
- [105] R. Roy. The cle-2000 tool-box. 1999.
- [106] <http://www-nds.iaea.org/wimsd/libraries.htm>.
- [107] T. Nakagawa et al. Japanese Evaluated Nuclear Data Library Version 3 Revision-2: JENDL-3.2. *Journal of Nuclear Science and Technology*, 32(12):1259–1271, 1995.

- [108] <http://t2.lanl.gov/ndf/title.html>.
- [109] G. Marleau, A. Hebert, and R. Roy. A user guide for dragon 3.06. 2007.
- [110] M. Benedict, T. H. Pigford, and H. W. Levi. *Nuclear Chemical Engineering*. McGraw-Hill Series in Nuclear Engineering. McGraw-Hill, second edition, 1981.
- [111] Treaty on the non-proliferation of nuclear weapons. <http://www.iaea.org/Publications/Documents/Infcircs/Others/infcirc140.pdf>, 1970.
- [112] A. Bernstein, Y. Wang, G. Gratta, and T. West. Nuclear reactor safeguards and monitoring with antineutrino detectors. *J. Appl. Phys.*, 91, 2002.
- [113] A. A. Borovoi and L. A. Mikaelyan. Possibilities of practical applications of neutrinos. *At. Energ.*, 44, 1978.
- [114] Patrick Huber and Thomas Schwetz. Precision spectroscopy with reactor anti-neutrinos. *Phys. Rev.*, D70:053011, 2004.
- [115] A. Bernstein, N. S. Bowden, A. Misner, and T. Palmer. Monitoring the thermal power of nuclear reactors with a prototype cubic meter antineutrino detector. *J. Appl. Phys.*, 103:074905, 2008.
- [116] S.B. Ludwig and J.P. Renier. Standard- and Extended-Burnup PWR and BWR Reactor Models for the ORIGEN2 Computer Code. *ORNL/TM-11018*, 1989.
- [117] M. D. DeHart and O. W. Hermann. An Extension of the Validation of SCALE (SAS2H) Isotopic Predictions for PWR Spent Fuel. *ORNL/TM-13317*, 1998.
- [118] <http://www.studsvikscandpower.com/nuclear-reactor-analysis-software>, 2012.
- [119] D. G. Martin. The thermal expansion of solid UO_2 and (u, pu) mixed oxides - a review and recommendations. *J. Nucl. Mater.*, 152:94 – 101, 1988.
- [120] L. M. Petrie, P. B. Fox, and K. Lucius. Standard composition library. *NUREG/CR-0200*, 1998.